Semiconductor Heterostructure Design For Non-linear Optical Processes For Quantum Information Technologies

by

Razif Bin Razali

Submitted in accordance with the requirements for the degree of Doctor of Philosophy

The University of Leeds

School of Electronic and Electrical Engineering

June 2017

The candidate confirms that the work submitted is his own, except where work which has formed part of jointly-authored publications has been included. The contribution of the candidate and the other authors to this work has been explicitly indicated below.

The candidate confirms that appropriate credit has been given within the thesis where reference has been made to the work of others.

Journal Papers

Studies of SPDC process as spectrally entangled twin photon source in Chapter 5 was based on the published papers,

Razali, R., Valavanis, A., Cooper, J. D., Ikonić, Z., Indjin, D., & Harrison, P. (2016). *Mid-infrared entangled photon generation in optimised asymmetric semiconductor quantum wells*. Superlattices and Microstructures, 90, 107-116.

Studies of SPDC process as polarization entangled twin photon source in Chapter 6 was based on the published papers,

Razali, R., Ikonić, Z., Indjin, D., & Harrison, P. (2016). *Polarization-entangledmid-infrared photon generation in p-doped semiconductor quantum wells*. Semiconductor Science and Technology, 31(11), 115011.

The candidate Razif Razali performed the simulation, analytical work and amended the qclsim and fhqw3a codes to use them with genetic optimization in finding the optimal structures. He also wrote the initial draft of the papers along with supporting material including Tables and Figures, carried out the calculation and summarisation of the results, and provided the discussion part.

The co-authors, Alex Valvanis and J. D. Cooper made the initial qclsim code ready to use and made suggestion and corrections to the draft paper. The co-authors, Zoran Ikoni{\'c}, Paul Harrison and Dragan Indjin, supervised the work and made suggestions and corrections to the draft papers.

The right of Razif Razali to be identified as Author of this work has been asserted by him in accordance with the Copyright, Designs and Patents Act 1988.

For my wife, kids, and both our parents.

Acknowledgements

I would like to express the deepest appreciation to my supervisors, Zoran Ikonić, who constantly engage with my research and kept me focus on this thesis, Paul Harrison for his enthusiasm and mentorship through this work and Dragan Indjin for helpful ideas on my work. The completion of this thesis would not have been possible without the help of all my supervisors. Their patience and encouragement help me a lot in completing this work. I would also like to thank Ministry of Higher Education Malaysia and Universiti Teknologi Malaysia for the support of my PhD studies in University of Leeds.

I am grateful to the students and staff of the quantum electronics group who I have shared an office with over the years. Special thanks to Andrew Grier and Alex Valavanis who guide me with the qclsim code.

My special thanks also goes to all my friends in Leeds who always give me their encouraging guide and give me their assistance wherever I need throughout the final stage of my thesis.

Not forgotten, to my families, especially to my both parents and my late dad in-law, who always give their blessed and moral support through my journey.

To my wife, Noor Syazuani Arazmi, thanks a lot for always be with me. Your presence in my life bring wonderful memories that we share with our kids.

Razif Bin Razali, June 2017

Abstract

Quantum information technologies require reliable sources of correlated/entangled photons. To realize and use these technologies in real life rather than just in laboratory, high efficiency and stable sources of entangled photons are needed.

This work considers the design of various semiconductor heterostructures, based on $Al_xGa_{1-x}As/GaAs$, that rely on intersubband transitions in the conduction or in the valence band, to deliver the second order nonlinear process, known as spontaneous parametric down-conversion (SPDC). The second-order SPDC can produce Bell state entangled photons. Second harmonic generation (SHG) is a well known and broadly discussed process, and using the fact that SHG is the reverse process of SPDC, initial studies of SHG are used to support the validity and accuracy of the methodology employed for nonlinear susceptibility calculations.

In designing the heterostructures, genetic optimization is used to reduce the computational cost in finding the best structure. The heterostructures designed by considering the intersubband transitions in the conduction band constitute good sources of spectrally entangled photons. The efficiency of the process is estimated and the Schmidt number calculation shows that the structure can produce twin photons with a reasonably good degree of entanglement.

Alternatively, using intersubband transitions in the valence band can deliver the polarization entangled photons, which cannot be achieved with conduction intersubband transitions. The genetic optimization is again used to design the best structures for this purpose, and the efficiency of the process is also calculated.

We then extend our work to multiparticle entangled states, also known as Greenberger-Horne-Zeilinger (GHZ) states, by considering the third order nonlinear SPDC (TOSPDC) process in designing the heterostructures for this purpose. This designed structure can be a good candidate as a direct TOSPDC source, since the second order nonlinearity is here suppressed by considering symmetric structures only. The efficiency of the process is also calculated and discussed in the thesis.

List of Publications

The following journal papers were contributed to by the author during the course of the present work.

Razali, R., Valavanis, A., Cooper, J. D., Ikonić, Z., Indjin, D., Harrison, P. (2016). *Mid-infrared entangled photon generation in optimised asymmetric semiconductor quantum wells.* Elsevier - Superlattices and Microstructures, 90, 107-116. IF : 2.117

Razali, R., Ikonić, Z., Indjin, D., Harrison, P. (2016). *Polarization-entangled mid-infrared photon generation in p-doped semiconductor quantum wells.* IOP - Semiconductor Science and Technology, 31(11), 115011. IF : 2.098

Contents

List of Figures

List of Tables

Abstract

Quantum information technologies require reliable sources of correlated/entangled photons. To realize and use these technologies in real life rather than just in laboratory, high efficiency and stable sources of entangled photons are needed.

This work considers the design of various semiconductor heterostructures, based on $Al_xGa_{1-x}As/GaAs$, that rely on intersubband transitions in the conduction or in the valence band, to deliver the second order nonlinear process, known as spontaneous parametric down-conversion (SPDC). The second-order SPDC can produce Bell's state entangled photons. Second harmonic generation (SHG) is a well known and broadly discussed process, and using the fact that SHG is a reverse process of SPDC, initial studies of SHG are used to support the validity and accuracy of the methodology employed for nonlinear susceptibility calculations.

In designing the heterostructures, genetic optimization is used to reduce the computational cost in finding the best structure. The heterostructures designed by considering the intersubband transitions in the conduction band constitute good sources of spectrally entangled photons. The efficiency of the process is estimated and the Schmidt number calculation shows that the structure can produce twin photons with a reasonably good degree of entanglement.

Alternatively, using intersubband transitions in the valence band can deliver the polarization entangled photons, which cannot be achieved with conduction intersubband transitions. The genetic optimization is again used to design the best structures for this purpose, and the efficiency of the process is also calculated.

We then extend our work to multiparticle entangled states, also known as GHZ states, by considering the third order nonlinear SPDC process in designing the heterostructures for this purpose. This designed structure can be a good candidate as a direct TOSPDC source, since the second order nonlinearity is here suppressed by considering symmetric structures only. The efficiency of the process is also calculated and discussed in the thesis.

Nomenclature

Acronyms

BZ	Brillouin zone
CB	Conduction band
DFG	Difference frequency generation
EFA	Envelope function approximation
EMA	Effective mass approximation
EPR	Einstein, Podolsky and Rosen
GHZ	Greenberger, Michael Horne and Anton Zeilinger
HH	Heavy hole
LH	Light hole
OPO	Optical parametric oscillators
OR	Optical rectification
QD	Quantum dot
QI	Quantum information
QM	Quantum mechanics
QO	Quantum optics

QW Quantum well

SFG Sum frequency generation

SFWM Spontaneous four wave mixing

SHG Second harmonic generation

SO Split-off orbital

SPDC Spontaneous parametric down conversion

TOSPDC Third order spontaneous parametric down conversion

VB Valence band

Fundamental constants

$c = 3.00 \times 10^8$m/s Speed of light in vacuum

$e = 1.60 \times 10^{-19}$ C Electron charge

$\varepsilon_0 = 8.85 \times 10^{-12}$ F/m Vacuum permittivity

$\hbar = 1.05 \times 10^{-34}$ Js Reduced Planck constant

$k_B = 1.38 \times 10^{-23}$ J/K Boltzman constant

$m_e = 9.11 \times 10^{-31}$ Kg Free electron rest mass

Chapter 1

Introduction

This chapter covers the introduction to quantum information, the reason behind this work was conducted and the structure of the thesis.

1.1 Introduction to quantum information

In quantum mechanics (QM), an object can be a particle and wave at the same time. This dual character enables a quantum-scale particle to exist simultaneously in multiple places in superposition, allowing wave-like interference. But when the particle is observed, its state will collapse to one position with some probability, meaning that any single quantum event in general cannot be predicted with certainty. Even more interesting phenomena on quantum-scale is entanglement; when two or more quantum-scale particles can be separated in space but still share connection via their combined state. In the event of measurement of the state of one separated particle, the others states will react instantaneously. This is something that Einstein, Podolsky and Rosen (EPR) could not explain and published the famous paper, known as EPR Paradox [2]. Then Bell introduced a method to check the EPR theory [3].

Quantum information (QI) was born based on the prediction of QM theory about encoding information in quantum system state. Several quantum information theory have been proposed in the past 50 years, by encoding and manipulating information using quantum superposition and entanglement. For example,

quantum cryptography [4], quantum computation [5], quantum teleportation [6], quantum metrology, quantum simulation, quantum encryption [7], quantum teleportation [8], and quantum factoring algorithms which are exponentially faster than their classical counterparts [9].

To have fully functional and practical quantum technologies, multiple challenges must be overcome, for example, in particular for computation, the technology must allow the scalable realisation, the measurement must be accurate, and able to control the QI elements, also known as qubit. Qubits or quantum bits are the quantum analogue of the classical bits of information. This qubits, can exist in superposition of the "0" and "1" levels as quantum states $|0\rangle$ and $|1\rangle$ respectively. But to have all of that, we must have reliable source of the qubits.

Different physical approaches have been developed to be a source of qubits and the most popular one is spontaneous parametric down conversion (SPDC) which is also known as parametric fluorescence in early days of this methods, based on nonlinear optics.

1.2 Background of the Problem - Reason for the research

Information processing in quantum systems can perform many tasks which are impossible in classical systems. Much progress has been made in implementing QI processing in optical systems by encoding information in polarization state of single photons. However, experimental implementation of many of the ideas for QI processing using optics requires a reliable source of correlated/entangled and single photons. To make sure that the QI processing can be implemented in real life, rather than just in laboratory, high efficiency and stable sources of entangled photons were needed. Many methods were proposed to produce suitable entangled photon pair sources and researchers who work in this area are struggling to find the reliable ones. So here, we will search for high efficiency entangled photons sources by designing suitable semiconductor heterostructure that is expected to give optimum second and third order non-linear susceptibility with acceptable level of output photon absorption.

In this project, there are three main objectives to be completed. The first one is to design and optimize semiconductor heterostructure for SPDC process by increasing the second order nonlinear susceptibility ($\chi^{(2)}$) value in conduction band. Secondly, we consider the valence band, to achieve optimum structure for polarization entanglement, and finally we consider the third order SPDC (TOSPDC), to design structures for producing multi photon entanglement, which may have wider applications compared to two photon entanglement.

By optimizing the structure of the quantum well, one can increase the $\chi^{(2)}$ or $\chi^{(3)}$ value for SDPC process to occur efficiently. By increasing the nonlinear susceptibility value, the entangled photons can be produced insufficient number to be useful in QI, especially if the phase matching is provided.

This work will give a good semiconductor heterostructure design, that can be fabricated, to produce high intensity entangled photons. Since the study focuses on semiconductor quantum well heterostructures, it is believed that the work will result in very small-sized entangled photons sources (on the micro- or nano scale).

1.3 Thesis Structure

The main purpose of this project is to produce a detailed theory on the design of semiconductor heterostructures that give high efficiency generation of entangled photons for QI technologies. The efficiency depends on the non-linear susceptibility and the absorption effect, by assuming that SPDC process is (almost) perfectly phase matched. Chapter 2 reviews previous work related to this project, starting from the birth of understanding of photon, spontaneous parametric down conversion in general and in semiconductor area specifically. Chapter 3 discusses on the main theory and methodology used in this project. Chapter 4 will be a groundwork to make sure that our calculation methods produce results comparable to previous work. Chapter 5 presents our results on SPDC based on conduction band intersubband transitions. Chapter 6 presents our results on SPDC based on valence band intersubband transitions, focusing on polarization entangled photons. Chapter 7 discusses on TOSPDC in valence band to achieve optimal structure for three photon entanglement. The results of Chapters 5 and 6 are already published, and those from Chapter 7 will be submitted soon. Chapter

8 will summarize the whole thesis, and make suggestions for improvements and further work .

1.4 Contributions of the Thesis

This work fully agrees with previous calculation of nonlinearities, as discussed in Chapter 4. Chapter 5 to 7 extend the work to the topics of present interest. We defined the correct way to calculate dipole matrix elements when nonparabolicity effects are included in Chapter 5. In this thesis we show that by using genetic optimization we can find the best structure for different types of SPDC processes. In fact, this can be used for different types of nonlinear phenomena that may be studied in the future.

This thesis is the work of designing the quantum well (QW) heterostructures to work as the entangled photon sources. The design of QWs heterostructures by finding the best one by genetic optimisation will cut the computation time and cost. The results of this thesis will also cut the cost and time for fabricating and testing the real structures in experimental work. Since the optimization is based on semiconductor QW heterostructures, the size of the entangled photon device is small compared to the current working devices.

Chapters 5 and 6 are the work that has already been published, as listed in preamble, Pages v. The work from Chapter 7 will be submitted for publication in the future.

Chapter 2

Literature Review

This chapter reviews the previous work related to SPDC, in five sections. The first section reviews the concept of semiconductor heterostructures. The second section describes empirical band-structure methods used for modelling the QWs structures. The third section describes the concept of entangled photons. The fourth section discusses general properties of SPDC, and some results of previous research in its use for entangled photon generation, while the last section reviews the third order SPDC (TOSPDC) as a direct source of entangled photon triplets.

2.1 Semiconductor Heterostructures

Heterostructures are made of two or more heterojunctions that are arranged together. Heterojunction is the interface between two different layers, denoted by the dashed line in Figure 2.1. When the narrow-bandgap material is placed between two wider-bandgap materials, this comprises two heterojunctions. This kind of alignment is known as single QW (Figure 2.2 (left)). If there are charge carriers in the system, they will tend to stay inside the QW, unless excited optically or electrically.

Complex heterostructures such as stepped (Figure 2.2 (right)), asymmetric (Figure 2.3 (left)) or symmetric (Figure 2.3 (right)) and multiple QWs (Figure 2.4) (superlattice) can be formed by adding more semiconductor layers. This will result in different electronic and optical properties of materials, that are open for

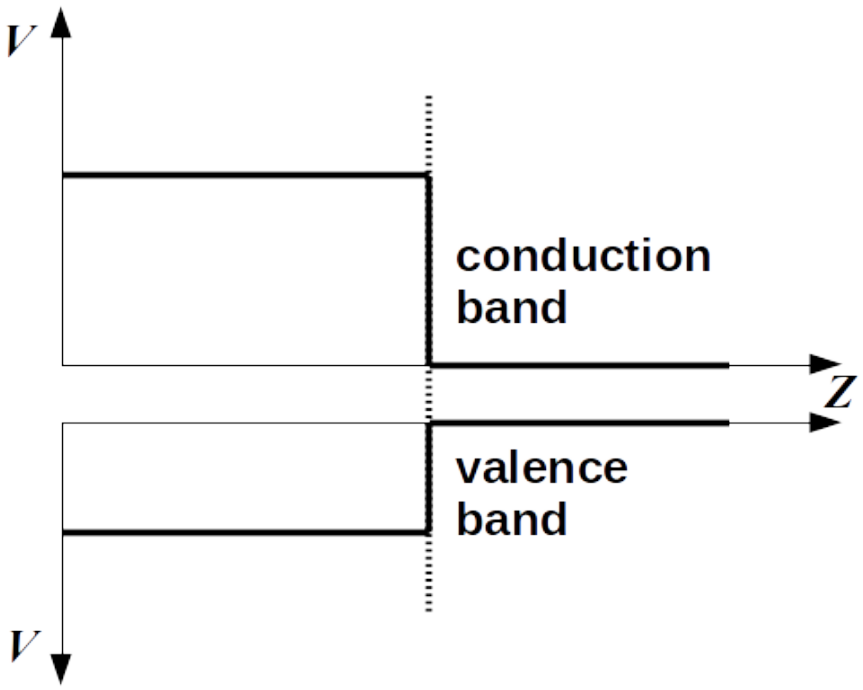

Figure 2.1: Heterojunctions (dashed line) between two different materials

exploitation. Esaki and Tsu in 1970 were the first to study one-dimensional periodic potential (superlattice) semiconductors formed by periodic variation of alloy composition [10]. In their paper, they focus on InAs-based alloy and the most studied GaAs-based alloy system. Based on Esaki and Tsu's discovery, Chang *et al.* [11] were the first to fabricate GaAs/$Al_xGa_{1-x}As$ using ultra high vacuum epitaxy system. They managed to fabricate a structure with very short period and measured its transport properties.

The discovery by Esaki and Tsu has been the starting point for studies of superlattices and observations of quantum mechanical effects in new physical scale.

2.2 Empirical Band-structures Method

Tight-binding, pseudopotential and the **k.p** method are the three most common empirical band-structures methods used for semiconductors. The choice of basis functions in Schröndinger's equation is what makes these three different (atomic-

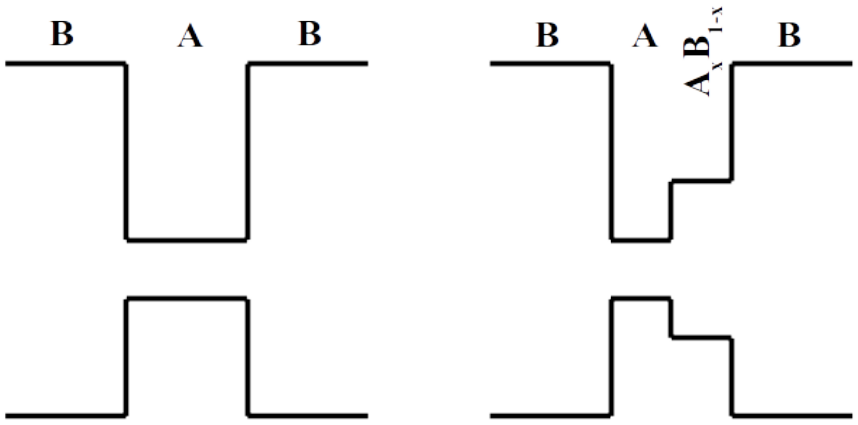

Figure 2.2: Single quantum well (left) diagram and stepped quantum well (right)

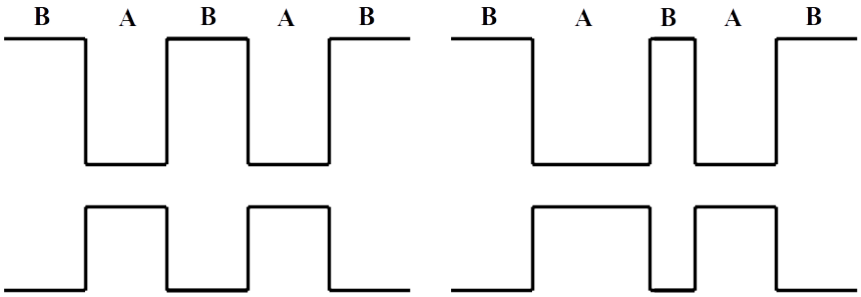

Figure 2.3: Symmetric quantum well (left) diagram and asymmetric quantum well (right)

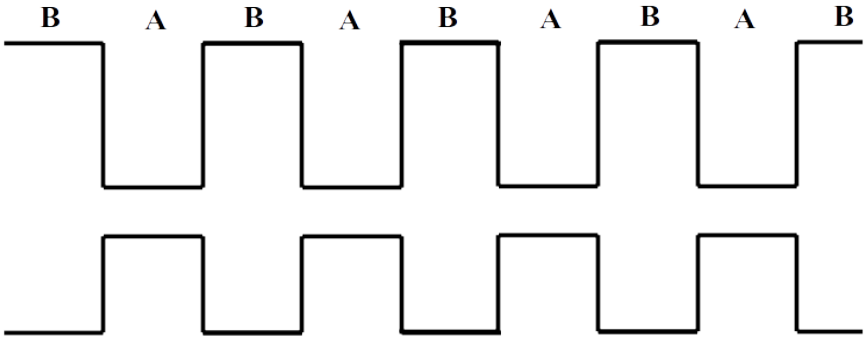

Figure 2.4: Multiple quantum well or superlattice

like, plane-wave and Bloch states respectively).

In this work, **k.p** method is chosen. This method is an efficient way to describe the conduction band (CB), valence band (VB), or both near a given point of the Brillouin zone (BZ). There are several **k.p** models, the simplest version of **k.p** method is known as effective mass method or approximation (EMA) which describes electronic properties in the CB (and as a first approximation in the VB), where the electronic states are non-degenerate and weakly interacting with each other. It is also known as 1-band model. In their paper, Bir and Pikus discuss in very detail the symmetry constraints for 1-band model.

In 2-band model, CB-VB coupling is considered, but spin is not included. The CB has one non-degenerate band $|s\rangle$ and the VB has 3 degenerate band $|p_x\rangle$, $|p_y\rangle$ and $|p_z\rangle$. This model considers coupling of CB with one VB(a particular linear combination of $|p_x\rangle$, $|p_y\rangle$ and $|p_z\rangle$).

4-band model considers one CB and three VB, and ignores more remote bands. Spin is also not included.6-band model comes from the 3 band model by introducing spin-orbit interaction. 8-band model is applied for semiconductors with direct band gap, where both CB and VB have extrema at k=0. This is an extension of the 4-band model where spin-orbit coupling is included, and also more remote bands, by Lowdin perturbation theory.

There are many others extended versions of the **k.p** method that includes CB,heavy hole (HH),light hole (LH) and split-off band (SO), and even more remote bands, but in this work, only 1-band and 6-band model is used since our calculation only focuses on intersubband transitions within CB (Chapter 4 and 5), or within VB (Chapter 6 and 7).

2.3 Entangled Photons

First nonlinear optical experiments were done by Franken *et al.* in 1961 and this is marked as the birth of nonlinear optics field [12]. They studied second harmonic generation by shooting a ruby laser beam to a quartz crystal and observed ultraviolet radiation at the output. Dingle *et al.* in 1974, using optical bandgap spectroscopy in GaAs/AlGaAs structure, have introduced the first experimental evidence for quantized states in QW [13]. The generation of squeezed states was

first demonstrated using four wave mixing method [14, p. 471].

The idea of photon was first introduced by Planck in 1901 when he worked on black-body radiation experiment and suggested that the energy in electromagnetic waves could only be released in packets [15]. In 1965, Einstein suggested that the electromagnetic waves could only exist in discrete wave-packets which he called quanta [16]. Lewis, a physical chemist, published a speculative theory that photons were uncreatable and indestructible in 1926 [17]. Although his theory was contradicted by many experiments, the name photon was adopted and used by many physicists to explain the discrete energy of light. When the first ideas of photon arose, the generation of single photons has not yet been considered.

Many experimental physicists in early stage of understanding photon used attenuated laser beam to ensure that the probability of having more than one photon became negligible. Although this method is acceptable for some experiments, it is still questionable because the attenuated laser beam is not a true single-photon source. When using attenuated laser beam, the vacuum probability is much higher than the probability to detect a photon, so the detection of no photon regime is always higher than the single photon itself. The probability to detect two photons is also generally non-zero. So the attenuated laser beam cannot be considered as a single photon source.

Nowadays, the advance in quantum information science has increased the demand for the optical sources which produce ultra bright single photons. In particular secure quantum cryptography and linear optical quantum computing depend on the availability of such single-photon sources. The combination of strict requirements for single photons plus new technologies are driving an exciting research effort into single-photon generation.

Quantum dots (QDs) in pillar micro cavities, falling neutral atoms and trapped ions in cavities, defects in diamond nanocrystals, single molecule in a solid and parametric down conversion are among the methods used to produce single photons and photon pairs [18]. The most commonly used method is called the parametric down conversion process which was first introduced by Klyshko [19]. This method was first called photon fluorescence and it produced photon pairs.

The photon-pair generation in SPDC process is a second order nonlinear process in which a pump photon disappears leading to the creation of two photons

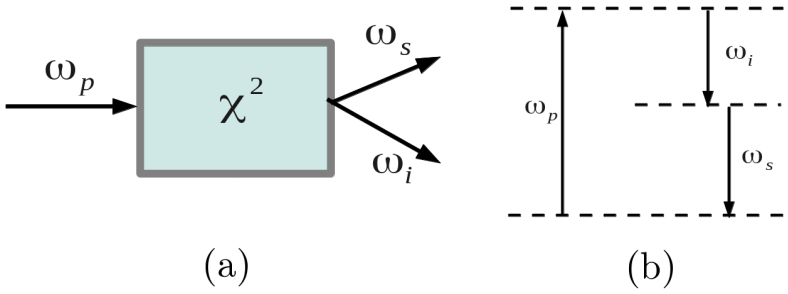

Figure 2.5: Spontaneous Parametric Down Conversion Process (SPDC). (a) Geometry of SPDC, (b) Energy-level diagram describing the SPDC process

with lower energy. This generation is driven by an optical pump field oscillating at frequency ω_p and occurs spontaneously to produce twin photons, namely the signal and idler photons with frequencies ω_s and ω_i respectively, which are lower in frequency than ω_p. This process can be conceptually illustrated by the diagram in Figure 2.5.

The signal and idler photons are said to be entangled to each other in frequency domain [20]. The non-classical correlation between the intensities of the generated two- photon states has been observed for the first time by Burnham and Weinberg in 1970 [21], and has become widely used in the experiments of quantum optics (QO). Thanks to the seminal work of Leonard Mandel and his collaborators [22, 23, 24, 25], optical parametric oscillators (OPO) based on processes of down-conversion in a cavity have proven to be efficient sources of frequency tunable light with a range of unique properties.

2.4 Spontaneous Parametric Down Conversion (SPDC)

Most popular method to generate entangled photon source is by using SPDC method. This method was first introduced by Klyshko at a seminar of the Solid State Physics Institute in Chernogolovka in 1966. His talk was about the prediction of a new non-linear optical and essentially quantum phenomenon which

he called at that time 'parametric luminescence'. Later in 1967, he developed the theory of SPDC effect and all the authors of the work; Klyshko, Fadeev, and Chunayev were awarded a discovery diploma for their theoretical prediction and experimental observation of this new kind of light scattering. Later, this effect became a basis for a new direction in laser spectroscopy, SPDC spectroscopy , and a new direction in fundamental optics, quantum photometry [26].

From 1966 until today, there was a lot of research done to produce entangled photon pairs and the applications in optical measurements. Most research based on experimental work and several approaches tries to explain the SPDC phenomenon by using numerical methods. SPDC can be of two types which are called type I and type II. Type II SPDC can be divided into two groups which are collinear and non-collinear type II SPDC, which is based on the orientation of the nonlinear medium and the output photons. In 1985 Friberg *et al*. made an experiment to measure the time delays between two photons produced in the process of SPDC type I in a potassium dihydrogen phosphate crystal. The time resolution of these measurements was of the order of 100 ps. The correlation time was found to be independent of the coherence time of the pump photons or of the propagation time through the crystal. The efficiencies of getting the signal and idler photon in this experiment were small [27], so several works were done later to produce high efficiency parametric down conversion using type I and type II SPDC [28, 29, 30].

In 2002 Di Giuseppe *et al*. proposed a new theory of SPDC by using two nonlinear crystals that were separated by a linear dispersive medium. They have shown that the state function of the down converted photon can be controlled by design of the nonlinearity profile in the crystal, as well as the spatial and spectral profile of the pump field [31]. To validate their theory, they have carried out an experiment using type II SPDC in Boston University.

There are four general methods to produce entangled photon pairs from semiconductors. One of them is from a QD [32, 33, 34, 35]. The second method is from parametric scattering in bulk semiconductor crystal [36]. The third one is from coupled QWs[37] and the last one from double/pair QDs [38].

2.5 Third Order SPDC (TOSPDC)

Entangled photon generation does not stop at photon pairs (Bell's state). Daniel Greenberger, Michael Horne and Anton Zeilinger introduced multi photon entangled state, also known as GHZ state, in 1989 [39] which is different from the Bell state.

This GHZ state has extra advantages over the Bell state, for example, it can used as quantum repeaters [40], loophole free Bell test [41] and optical quantum computing [42, 43]. This GHZ state can also be used for multipartner quantum cryptography (1998) and communication complexity task (1997,2004) that cannot be achieved by using Bell state approach.

The simplest GHZ state is by having 3 photons that are entangled to one another. The first experimental observation of GHZ state was made by group of Anton Zeilinger in 1999 [44]. Based on GHZ works, several method were proposed to produce such states, for example triexcitonic decay in QDs [45],cascaded or post selective second-order nonlinear process [46, 47, 48, 49, 50, 51, 52] and formation of approximate three photons by SPDC photon pairs with attenuated coherent state [53].

All methods above do not produce GHZ state directly from the source, they have low photon generation rate, for example, in [50], they only manage to produce up to 45 triplet photons per minute. Corona *et al.* in their paper [54] proposed a method of direct generation of entangled photon triplets using third order SPDC in optical fibers.

The process of direct TOSPDC is illustrated in Figure 2.6. The GHZ state was firstly studied by Daniel Greenberger, Michael Horne and Anton Zeilinger in 1989 [39].

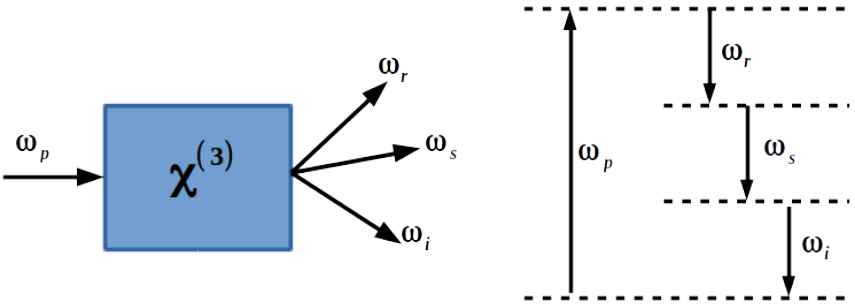

Figure 2.6: Third order Spontaneous Parametric Down Conversion Process (TOSPDC). Geometry of TOSPDC (left) and Energy-level diagram describing the TOSPDC process (right)

Chapter 3

Theory and Methodology

This chapter discusses the theory and methods used in this work.

3.1 Solving Schrödinger's Equation in Quantum Well

Effective mass approximation (EMA) is an important tool to solve the Schrödinger's Equation in semiconductor heterostructure devices. EMA assumes that charge carriers confined in semiconductor have low momentum. So only the bottom of momentum vs energy (dispersion relation) curve needs to be considered. For low momenta, the dispersion relation in most semiconductors are practically parabolic which is similar to dispersion relation for particle in free space.

Another important approximation that needs to be considered when solving Schrödinger's Equation is envelope function approximation (EFA). It is widely accepted that semiconductor heterostructure is considered as a series of one dimensional QWs which arise from the discontinuity of the band edges between different material. Solving the Schrödinger's Equation for this one dimensional QW model of heterostructure just gives the envelope function of the *real* wave function. But both approximations still produce results that represent the real systems [55].

3.1.1 Time-independent Schrödinger's Equation

The time-independent Schrödinger's Equation is usually written as:

$$\hat{H}\psi(\mathbf{R}) = E\psi(\mathbf{R}). \tag{3.1}$$

ψ is the wavefunction, $\mathbf{R}$ is the position and E is the total energy of the state. $\hat{H}$ is Hamiltonian operator, defined as:

$$\hat{H} = -\frac{\hbar^2}{2} \bigtriangledown \cdot \left(\frac{1}{m(\mathbf{R})} \bigtriangledown \right) + V(\mathbf{R}) \tag{3.2}$$

The EMA and EFA allow the Schrödinger's Equation to be solved in one dimensional QWs. So the Schrödinger's Equation can be written as:

$$-\frac{\hbar^2}{2}\frac{\partial}{\partial z}\frac{1}{m(z)}\frac{\partial}{\partial z}\psi(z) + V(z)\psi(z) = E\psi(z). \tag{3.3}$$

$m(z)$ is the effective mass and $V(z)$ is the band edge potential. The solution of this Schrödinger's Equation will give the Energy (E) and the related wave functions (ψ) for each state that may exist in potential profile given by $V(z)$.

3.1.2 Finite Difference Method

The solution of Equation (3.3) can be deduced using analytical or numerical method. Analytical solutions is 100% correct but it can only solve simple problems and are not possible for complex ones. To design complex semiconductor heterostructures with complicated Schrödinger's Equation to be solved, the numerical method is a must, but this method must be validated by the analytical solution (for simple problem) so that when it is used in complex system, the solution provided are acceptable and reliable.

In this work, finite difference method is used as numerical method to approximate the solution of differential equations in Equations (3.3) using finite difference equations to approximate the derivatives [56].

$$\frac{\mathrm{d}\psi(z)}{\mathrm{d}z} \approx \frac{\triangle\psi(z)}{\triangle z} = \frac{\psi_{i+1} - \psi_{i-1}}{2\delta z}. \tag{3.4}$$

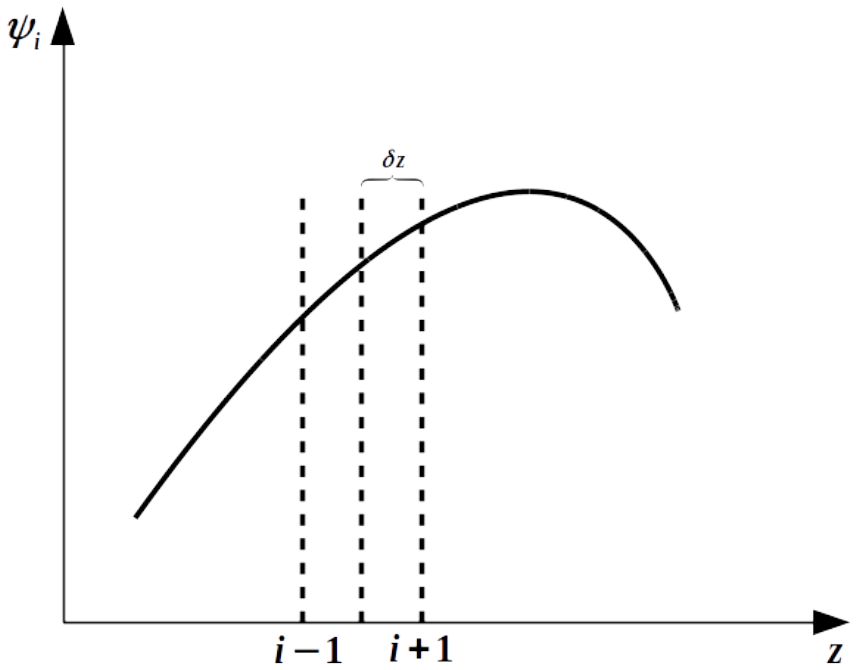

Figure 3.1: Finite difference method that split up the function of $\psi(z)$ to set of mesh point i.

The finite difference method splits up the function $\psi(z)$ into a set of discrete mesh points ($i = 0, 1, 2, ..., N$). δz is spacing between two mesh points while ψ_{i+1} and ψ_{i-1} is the value of the function at either side of ψ_i. The second derivative in Equation (3.4) can be written as:

$$\frac{\mathrm{d}^2\psi(z)}{\mathrm{d}z^2} \approx \frac{\frac{\mathrm{d}\psi(z)}{\mathrm{d}z}\Big|_{i=i+1} - \frac{\mathrm{d}\psi(z)}{\mathrm{d}z}\Big|_{i=i-1}}{2\delta z} \tag{3.5a}$$

$$\approx \frac{\psi_{i+2} - 2\psi_i + \psi_{i-2}}{(2\delta z)^2}. \tag{3.5b}$$

Since value of δz as is yet undefined small step along the z-axis, Equation (3.5) can be simplified by substitute $2\delta z$ to δz and change the mesh points shifted from 2 to 1:

$$\frac{\mathrm{d}^2\psi(z)}{\mathrm{d}z^2} \approx \frac{\psi_{i+1} - 2\psi_i + \psi_{i-1}}{(\delta z)^2}. \tag{3.6}$$

Then the Schrödinger's Equation will look like Equation (3.7),

$$-\frac{\hbar^2}{2}\left(\frac{1}{m_{i+1}}\frac{\psi_{i+1}-\psi_i}{2\delta z}-\frac{1}{m_{i-1}}\frac{\psi_{i-1}-\psi_i}{2\delta z}\right)/2\delta z+V_i\psi_i=E\psi_i, \tag{3.7}$$

with ψ, m, and V discretized which depend on subscript i that denotes a specific mesh point. Equation (3.7) can be arranged to equation below:

$$-\frac{\hbar^2}{2(\delta z)^2}\left\{\frac{\psi_{i+1}-\psi_i}{m_{i+1/2}}-\frac{\psi_i-\psi_{i-1}}{m_{i-1/2}}\right\}+V_i\psi_i=E\psi_i. \tag{3.8}$$

The $m_{i\pm1/2}$ is the effective mass value that its mesh point lie between the actual mesh points and can be treated as the mean effective mass of the two adjacent mesh points.

3.1.3 Matrix Eigenvalue Problem Representation

In this project, matrix method is used to solve the discretized Schrödinger's Equation (3.8). This method is chosen rather than others methods, like shooting method [56] or linear bi-section root finding approach [57] because when the linear matrix is created, the matrix then can easily passed to a matrix eigenvalue problem solver such as LAPACK to solve the equations numerically [58].

To do that, Equation (3.8) need to be arranged so that the coefficients of ψ can be grouped together:

$$-\frac{\hbar^2}{2(\delta z)^2}\left\{\frac{\psi_{i+1}m_{i-1/2}-\psi_i(m_{i+1/2}+m_{i-1/2})+\psi_{i-1}m_{i+1/2}}{m_{i+1/2}m_{i-1/2}}\right\}+V_i\psi_i=E\psi_i,$$

and become:

$$\frac{\hbar^2\psi_{i+1}}{2(\delta z)^2m_{i+1/2}}+\left(\frac{\hbar^2}{2(\delta z)^2}\frac{m_{i+1/2}+m_{i-1/2}}{m_{i+1/2}m_{i-1/2}}+V_i\right)\psi_i-\frac{\hbar^2\psi_{i-1}}{2(\delta z)^2m_{i-1/2}}=E\psi_i. \tag{3.9}$$

For adjacent values of i, the coefficients of ψ_{i+1} and ψ_{i-1} are identical, so the matrix constructed from Equation (3.9) will be tridiagonal symmetric as below:

$$\begin{pmatrix} b_0 & a_0 & 0 & \cdots & 0 \\ a_0 & b_1 & a_1 & \cdots & \vdots \\ 0 & \ddots & \ddots & \ddots & 0 \\ \vdots & \cdots & a_{N-2} & b_{N-1} & a_{n-1} \\ 0 & \cdots & 0 & a_{N-1} & b_N \end{pmatrix} \begin{pmatrix} \psi_0 \\ \psi_1 \\ \vdots \\ \psi_{N-1} \\ \psi_N \end{pmatrix} = E \begin{pmatrix} \psi_0 \\ \psi_1 \\ \vdots \\ \psi_{N-1} \\ \psi_N \end{pmatrix} \tag{3.10}$$

with,

$$a_i = -\frac{\hbar^2}{2(\delta z)^2 m_{i+1/2}} \tag{3.11}$$

$$b_i = \frac{\hbar^2}{2(\delta z)^2} \frac{m_{i+1/2} + m_{i-1/2}}{m_{i+1/2} m_{i-1/2}} + V_i. \tag{3.12}$$

Equation (3.10) is the time-independent Schrödinger's Equation in matrix form as below:

$$\mathbf{H}\psi = E\psi, \tag{3.13}$$

where $\mathbf{H}$ is the Hamiltonian matrix operator that will be pass to LAPACK to find the solutions.

3.1.4 Non-parabolicity

EMA for GaAs/GaAlAs is only valid for low energies case. When the carrier energy is increased to fraction of electron volt range, this approximation would fail to give accurate representation because the dispersion curve is no longer parabolic. Non-parabolicity is then introduced to consider the deviation of real and parabolic dispersion relations by including the energy dependent term.

Harrison in his book defines the EMA when band non-parabolicity is included to have an energy dependence [59];

$$m^*(E, z) = m^*(z)[1 + \alpha(z)(E - V(z))], \tag{3.14}$$

where V is the band edge potential, m^* is the electron effective mass in GaAs/GaAlAs

which is calculated as $m* = (0.067 + 0.083x)m_0$, where x is the mole fraction of Al, and the parameter α is given by;

$$\alpha = \left[1 - \frac{m^*(z)}{m_0}\right]^2 / E_g. \tag{3.15}$$

E_g is the semiconductor bandgap.

3.1.5 Eigenvalue problem linearisation

Non-parabolic Schrödinger's equation cannot be solved directly by eigenvalue solver, i.e. LAPACK as Section 3.1.3 . The reason why this happened because the energy dependence of the non-parabolic effective mass change the matrix to be cubic eigenvalue problem. Cooper *et al*. overcome this restraint by linearising the cubic eigenvalue problem. The derivation of the methods can be found in their paper [60].

Based on Cooper *et al*. works, Ma *et al*. present improved method which they claimed to be much faster to find the solutions of eigenvalue problem [61].

3.2 k·p Method

In Section 2.2, 6-band model is chosen to describe the Schrödinger equation for valence band. So the basis state used in this method can be refer to equations below[62, 63].

$$|3/2, 3/2\rangle = (1/\sqrt{2})\,|(X{+}iY)\uparrow\rangle \tag{3.16a}$$
$$|3/2, -3/2\rangle = (1/\sqrt{2})\,|(X{-}iY)\downarrow\rangle \tag{3.16b}$$
$$|3/2, 1/2\rangle = (1/\sqrt{6})\,|(X{+}iY)\downarrow\rangle - \sqrt{2/3}\,|Z\uparrow\rangle \tag{3.16c}$$
$$|3/2, -/2\rangle = -(1/\sqrt{6})\,|(X{-}iY)\uparrow\rangle - \sqrt{2/3}\,|Z\downarrow\rangle \tag{3.16d}$$
$$|1/2, 1/2\rangle = (1/\sqrt{3})\,|(X{+}iY)\downarrow\rangle + (1/\sqrt{3})\,|Z\uparrow\rangle \tag{3.16e}$$
$$|1/2, -1/2\rangle = -(1/\sqrt{3})\,|(X{-}iY)\uparrow\rangle + (1/\sqrt{3})\,|Z\downarrow\rangle \ . \tag{3.16f}$$

The Hamiltonian that describes the HH, LH and SO bands for $|J,m_J\rangle$,

$$H = \begin{pmatrix} P+Q & 0 & -S_- & R & (1/\sqrt{2})S_- & \sqrt{2}R \\ 0 & P+Q & -R^\dagger & -S_+ & -\sqrt{2}\text{-}R^\dagger & (1/\sqrt{2})\text{-}S_+ \\ -\text{-}S_-^\dagger & -R & P\text{-}Q & C & \sqrt{2}Q & \sqrt{3/2}\Sigma_- \\ R^\dagger & -S_+^\dagger & C^\dagger & P\text{-}Q & -\sqrt{3/2}\Sigma_+ & 2Q \\ (1/\sqrt{2})S_-^\dagger & -\sqrt{2}R & \sqrt{2}Q & -\sqrt{3/2}\Sigma_+^\dagger & P+\Delta & -C \\ \sqrt{2}R^\dagger & (1/\sqrt{2})S_+^\dagger & \sqrt{3/2}\text{-}\Sigma_-^\dagger & \sqrt{2}Q & -C^\dagger & P+\Delta \end{pmatrix} \tag{3.17}$$

with

$$P = \frac{\hbar^2}{2m_0}\gamma_1(k_x^2 + k_y^2 + k_z^2) \tag{3.18a}$$

$$Q = \frac{\hbar^2}{2m_0}\gamma_2(k_x^2 + k_y^2 - 2k_z^2) \tag{3.18b}$$

$$R = \sqrt{3}\frac{\hbar^2}{2m_0}(-\overline{\gamma}k_-^2 + \mu k_+^2 \tag{3.18c}$$

$$S_\pm = 2\sqrt{3}\frac{\hbar^2}{2m_0}k_\pm[(\sigma-\delta)k_z + k_z\pi] \tag{3.18d}$$

$$\Sigma_\pm = 2\sqrt{3}\frac{\hbar^2}{2m_0}k_\pm\left\{\left[\frac{1}{3}(\sigma-\delta)+\frac{2}{3}\pi\right]k_z + k_z\left[\frac{2}{3}(\sigma-\delta)+\frac{1}{3}\pi\right]\right\} \tag{3.18e}$$

$$C = 2\left(\frac{\hbar^2}{2m_0}\right)k_-[k_z(\sigma-\delta-\pi) - (\sigma-\delta-\pi)k_z] \tag{3.18f}$$

$$k_\pm = k_x \pm ik_y, \overline{\gamma} = \frac{1}{2}(\gamma_2+\gamma_3), \mu = \frac{1}{2}(\gamma_3-\gamma_2) \tag{3.18g}$$

$$\sigma = \overline{\gamma} - \frac{1}{2}\delta, \pi = \mu + \frac{3}{2}\delta = \frac{1}{9}(1+\gamma_1+\gamma_2-3\gamma_3) \tag{3.18h}$$

and Δ is the spin-orbit splitting.

Introducing new basis,

$$|F_1\rangle = \alpha\,|3/2,-3/2\rangle - \alpha * |3/2,3/2\rangle \tag{3.19a}$$

$$|F_2\rangle = \beta\,|3/2,1/2\rangle + \beta * |3/2,-1/2\rangle \tag{3.19b}$$

$$|F_3\rangle = \beta\,|1/2,1/2\rangle + \beta * |1/2,-1/2\rangle \tag{3.19c}$$

$$|F_4\rangle = \alpha\,|3/2,-3/2\rangle + \alpha * |3/2,3/2\rangle \tag{3.19d}$$

$$|F_5\rangle = \beta\,|3/2, 1/2\rangle - \beta * |3/2, -1/2\rangle \tag{3.19e}$$

$$|F_6\rangle = \beta\,|1/2, 1/2\rangle - \beta * |1/2, -1/2\rangle \tag{3.19f}$$

where

$$\alpha = \frac{1}{\sqrt{2}} exp\left[i(\phi/2 + \eta + \pi/4)\right] \tag{3.20a}$$

$$\beta = \frac{1}{\sqrt{2}} exp\left[i(\phi/2 - \eta - 3\pi/4)\right] \tag{3.20b}$$

$$\phi = \arctan(k_x/k_y) \tag{3.20c}$$

$$\eta = \frac{1}{2}\arctan\left[(\omega_3/\omega_2)\tan(2\phi)\right] \tag{3.20d}$$

the Hamiltonian takes a block-diagonal form

$$H = \begin{pmatrix} H_+ & 0 \\ 0 & H_- \end{pmatrix} \tag{3.21}$$

where

$$H_\pm = \begin{pmatrix} P{+}Q & R{\pm}iS & \sqrt{2}R{\pm}i/\sqrt{2}S \\ R{\pm}iS^\dagger & P{\text{-}}Q\ {\mp}iC & \sqrt{2}Q \mp i\sqrt{3/2}\Sigma \\ \sqrt{2}R \mp i/\sqrt{2}S^\dagger & \sqrt{2}Q \pm i\sqrt{3/2}\Sigma^\dagger & P\ {+}\Delta \pm i\ C \end{pmatrix} \tag{3.22}$$

where P and Q are same as above and R, S, Σ and C now,

$$R = -\sqrt{3}\left(\frac{\hbar^2}{2m_0}\right)\gamma_\phi k_\parallel^2 \tag{3.23a}$$

$$S = 2\sqrt{3}\left(\frac{\hbar^2}{2m_0}\right)k_\parallel\left[(\sigma-\delta)k_z + k_z\pi\right] \tag{3.23b}$$

$$\Sigma = 2\sqrt{3}\left(\frac{\hbar^2}{2m_0}\right)k_\parallel\left\{\left[\frac{1}{3}(\sigma-\delta) + \frac{2}{3}\pi\right]k_z + k_z\left[\frac{2}{3}(\sigma-\delta) + \frac{1}{3}\pi\right]\right\} \tag{3.23c}$$

$$C = 2\left(\frac{\hbar^2}{2m_0}\right)k_\parallel\left[k_z(\sigma-\delta-\pi) - (\sigma-\delta-pi)k_z\right] \tag{3.23d}$$

$$\gamma_\phi = \sqrt{\overline{\gamma^2} + \mu^2 - 2\overline{\gamma}\mu cos\phi} \tag{3.23e}$$

$$k_{\parallel}^2 = k_x^2 + k_y^2 \ . \qquad (3.23f)$$

In the presence of biaxial strain,

$$\varepsilon_{xx} = \varepsilon_{yy} \neq \varepsilon_{zz} \qquad (3.24a)$$

$$\varepsilon_{xy} = \varepsilon_{yz} = \varepsilon_{zx} = 0 \ . \qquad (3.24b)$$

The P and Q terms in the Hamiltonian are amended with the strain terms

$$P \rightarrow P + P_{\varepsilon}, \quad P_{\varepsilon} = -a_v(\varepsilon_{xx} + \varepsilon_{yy} + \varepsilon_{zz}) \qquad (3.25a)$$

$$Q \rightarrow Q + Q_{\varepsilon}, \quad Q_{\varepsilon} = -\frac{b}{2}(\varepsilon_{xx} + \varepsilon_{yy} - 2\varepsilon_{zz}) \qquad (3.25b)$$

where a_v and b are the Pikus-Bir deformation potentials, the other strain terms being zero. The strain components are evaluated from

$$\varepsilon_{xx} = \varepsilon_{yy} = \frac{a_0 - a_{lat}}{a_{lat}}, \qquad (3.26a)$$

$$\varepsilon_{zz} = -\frac{2C_{12}}{C_{11}}\varepsilon_{xx} \qquad (3.26b)$$

where C_{11} and C_{12} are the stiffness constants, a_0 is the lattice constant of substrate and a_{lat} is the lattice constant for the layer.

To find the quantized states energies and wave functions, the block-diagonal form of Hamiltonian is used by solving one 3×3 block at a time. The wave function, being a vector of length 3,

$$H_{\pm}\Psi_{\pm} = E\Psi_{\pm}, \qquad \Psi_{\pm}(\overrightarrow{r}) = \psi_{\pm}(z) \cdot exp[i(k_x x + k_y y)], \qquad (3.27a)$$

$$\psi_{+}(z) = \begin{pmatrix} F_1(z) \\ F_2(z) \\ F_3(z) \end{pmatrix}, \qquad \psi_{-}(z) = \begin{pmatrix} F_4(z) \\ F_5(z) \\ F_6(z) \end{pmatrix} \qquad (3.27b)$$

is expanded in Fourier series

$$F^{(\ell)}(z) = \sum_{\ell} F_j^{(\ell)} exp(ig_\ell z), \quad g_\ell = \ell \cdot \frac{2\pi}{L} \tag{3.28}$$

with L is the length of the periodicity of the structure. A finite number of g_ℓ vectors is taken, say N_z. For convenience and to facilitate using FFT in the calculation, g_ℓ's are taken in standard FFT order, i.e with $\ell = 0, 1, 2, ..., \pm N_z/2, -N_z/2+1, ..., -2, -1$. For each wave function component there is a vector of Fourier components, and stacked on top of each other these make the Fourier representation of the total wave function.

With the Luttinger γ parameters varying along the structure, the individual elements of the Hamiltonian block, when acting upon the wave function components, read (the factor $\hbar^2/2m_0$ is taken to be absorbed in the γ parameters, and use is made of the fact that ie. $S = (\sigma - \delta)k_z + k_z\pi$ and $S^\dagger = k_z(\sigma - \delta) + \pi k_z$),

$$(P + Q + V)F_1 = -\frac{d}{dz}(\gamma_1 - 2\gamma_2)\frac{dF_1}{dz} + (\gamma_1 + \gamma_2)k_{||}^2 F_1 + (V + P_\varepsilon + Q_\varepsilon)F_1 \tag{3.29a}$$

$$= -\frac{d(\gamma_1 - 2\gamma_2)}{dz}\frac{dF_1}{dz} - (\gamma_1 - 2\gamma_2)\frac{d^2F_1}{dz^2} + (\gamma_1 + \gamma_2)k_{||}^2 F_1 + (V + P_\varepsilon + Q_\varepsilon)F_1 \tag{3.29b}$$

$$(R \mp iS)F_2 = -\sqrt{3}\gamma_\phi k_{||}^2 F_2 \mp 2\sqrt{3}k_{||} \cdot \left[(\sigma - \delta)\frac{dF_2}{dz} + \frac{d}{dz}(\pi F_2)\right] \tag{3.30a}$$

$$\sqrt{3}\gamma_\phi k_{||}^2 F_2 \mp 2\sqrt{3}k_{||} \cdot \left[(\sigma - \delta + \pi)\frac{dF_2}{dz} + \frac{d\pi}{dz} \cdot (\pi F_2)\right] \tag{3.30b}$$

$$(\sqrt{2}R \pm \frac{i}{\sqrt{2}}S)F_3 = -\sqrt{2}\sqrt{3}\gamma_\phi k_{||}^2 F_3 \pm \sqrt{2}\sqrt{3}k_{||} \cdot \left[(\sigma - \delta + \pi)\frac{dF_2}{dz} + \frac{d\pi}{dz} \cdot F_2\right] \tag{3.31a}$$

$$(R \pm iS^{\dagger})F_2 = -\sqrt{3}\gamma_{\phi}k_{||}^2 F_1 \pm 2\sqrt{3}k_{||} \cdot \left[(\sigma - \delta + \pi)\frac{dF_1}{dz} + \frac{d(\sigma - \delta)}{dz} \cdot F_1\right] \tag{3.31b}$$

$$(P - Q \mp iC + V)F_2 = -\frac{d(\gamma + 2\gamma_2)}{dz}\frac{dF_2}{dz} - (\gamma_1 + 2\gamma_2)\frac{d^2F_2}{dz^2} + (\gamma_1 - \gamma_2))k_{||}^2 F_2 - \tag{3.32a}$$

$$\mp 2k_{||}\frac{d(\sigma - \delta - \pi)}{dz}F_2 + (V + P_{\varepsilon} - Q_{\varepsilon})F_2 \tag{3.32b}$$

$$(\sqrt{2}Q \mp i\sqrt{3/2}\Sigma)F_3 = 2\sqrt{2}\frac{d\gamma_2}{z}\frac{dF_3}{dz} + 2\sqrt{2}\frac{d^2F_3}{dz^2} + \sqrt{2}\gamma_2 k^2 + ||F_3 - \tag{3.33a}$$

$$\mp 3\sqrt{2}k_{||} \cdot \left[(\sigma - \delta + \pi)\frac{dF_3}{dz} + \frac{d(2\sigma - 2\delta + \pi)/3}{dz}F_3\right] + \sqrt{2}Q_{\varepsilon}F_3 \tag{3.33b}$$

$$(\sqrt{2}R \mp \frac{i}{\sqrt{2}}S^{\dagger})F_1 = -\sqrt{2}\sqrt{3}\gamma_{\phi}k_{||}^2 F_1 \mp \sqrt{2}\sqrt{3}k_{||} \cdot \left[(\sigma - \delta + \pi)\frac{dF_1}{dz} + \frac{d(\sigma - \delta)}{dz} \cdot F_1\right] \tag{3.34}$$

$$(\sqrt{2}Q \pm i\sqrt{3/2}\Sigma^{\dagger})F_2 = 2\sqrt{2}\frac{d\gamma_2}{z}\frac{dF_2}{dz} + 2\sqrt{2}\frac{d^2F_2}{dz^2} + \sqrt{2}\gamma_2 k_{||}^2 F_2 + \tag{3.35a}$$

$$\pm 3\sqrt{2}k_{||} \cdot \left[(\sigma - \delta + \pi)\frac{dF_2}{dz} + \frac{d(\sigma - \delta + 2\pi)/3}{dz}F_2\right] + \sqrt{2}Q_{\varepsilon}F_2 \tag{3.35b}$$

$$(P \pm iC + \Delta + V)F_3 = \tag{3.36a}$$

$$-\frac{d\gamma_1}{dz}\frac{dF_3}{dz} - \gamma_1\frac{d^2F_3}{dz^2} + \gamma_1 k_{||}^2 F_3 \pm \frac{d(\sigma - \Delta - \pi)}{dz}F_3 + (V + \delta + P_{\varepsilon})F_3 \tag{3.36b}$$

where + and − corresponds to the upper and lower block respectively. To set up the Hamiltonian matrix, then we can use the Fourier transforms of the Luttinger parameters and potentials (bias field, built-in and strain), and use

the fact that if ℓ-th Fourier component of $y(z)$ is y^ℓ, then the ℓ-th component of $dy(z)/dz$ is $ig_\ell y^{(\ell)}$. With the way of ordering of the wave functions' Fourier components as described above (the set of F_1^ℓ's first, then F_2^ℓ's and then F_3^ℓ's, with N_z components in each stack), we give a few examples of how the matrix elements are set up.

The (ℓ, j) element of the matrix, relating the ℓ-th and j-th components of F_1, according to the first relation. is given by

$$-(\gamma_1-2\gamma_2)^{(k)}\cdot ig_k\cdot ig_j-(\gamma_1-2\gamma_2)^{(k)}\cdot(ig_j)^2+(\gamma_1+\gamma_2)^{(k)}k_{||}^2+(V+P_\varepsilon+Q_\varepsilon^{(k)}, \quad (3.37)$$

the $(\ell, j+N_z)$ element, relating the ℓ-th component of F_1 and the j-th component of F_2, by

$$-\sqrt{3}\gamma_\phi^{(k)}k_{||}^2\cdot\left[(\sigma-\delta+\pi)^{(k)}\cdot ig_j+\pi^{(k)}\cdot ig_k\right] \quad (3.38)$$

the $(\ell, j+2N_z)$ element, relating the ℓ-th component of F_1 and the j-th component of F_3, by

$$-\sqrt{2}\sqrt{3}\gamma_\phi^{(k)}k_{||}^2\cdot\left[(\sigma-\delta+\pi)^{(k)}\cdot ig_j+\pi^{(k)}\cdot ig_k\right] \quad (3.39)$$

the $(\ell+N_z, j+N_z)$ element, relating the ℓ-th and the j-th component of F_2, by

$$-(\gamma_1+2\gamma_2)^{(k)}\cdot ig_k\cdot ig_j-(\gamma_1+2\gamma_2)^{(k)}\cdot(ig_j)^2+(\gamma_1-\gamma_2)^{(k)}k_{||}^2\mp 2k^{||}(\sigma-\delta-\pi)^{(k)}\cdot ig_k+(V+P_\varepsilon+Q_\varepsilon^{(k)}), \quad (3.40)$$

etc., where k is the subscript of the plane wave $g_k = g_\ell - g_j$ (if such g_k is out of the range included, the matrix elements equals zero). In the above expressions the superscript (k) denotes the k-th Fourier component of the corresponding z-dependent variable.

The Hamiltonian matrix is then diagonalized, i.e. eigenenergies and (optionally) eigenfunctions found, using the diagonalization subroutine for Hermitian matrices. Having found the wave functions for one or both blocks, these maybe easily expanded into the $|j, m_j\rangle$ representation if necessary.

3.2.1 Self-consistent calculation

If the calculation is to be self-consistent, the total potential must include the space-charge potential, along with that of the bias field and the coordinate-dependent valence band edge. The charge in the structure includes the -ve charge of ionized acceptors $N_A(z)$ and the +ve charge of holes $p(z)$. The former is stated in the data file and

$$p(z) = \sum_n \int \frac{dk_x dk_y}{4\pi^2} \cdot f_{FD}\left[E_n(k_x.k_y), E_F\right] \cdot \sum_{j=1}^{6} |F_{j,n,k_x,k_y}(z)|^2 \tag{3.41}$$

where the summation goes over all n states that are significantly populated, f_{FD} is the Fermi-Dirac function and E_F the Fermi level for holes (we choose the energy level to be measured downwards), and $F(z)$ the wave function components for states included.

The Fermi level is determined from the global neutrality condition, i.e. by numerically solving the equation

$$\int p(z)dz = \sum_n \int \frac{dk_x dk_y}{4\pi^2} \cdot f_{FD}\left[E_n(k_x.k_y), E_F\right] = \int N_A(z)dz = N_A^S \tag{3.42}$$

where N_A^S is the total acceptor doping per unit surface of the structure. This done by bisection, i.e the Fermi level is varied until the holes space charge, which depends on E_F, balances the acceptors space charge, which is constant, with satisfactory accuracy.

The potential $V_{sc}(z)$ is then found by solving the Poisson equation

$$\Delta[\varepsilon(z)\Delta V_{sc}(z)] = -\frac{e[p(z) - N_A(z)]}{\varepsilon_0} \tag{3.43}$$

where $\varepsilon(z)$ is the relative dielectric permittivity, varying along the structure because it is material dependent. This equation is solved by making the finite-difference approximation, which results in a tridiagonal system of linear equations, which may then be solved very fast.

The self-consistent solution is obtained iteratively. Once the quantized states of the structure have been found in a particular iteration (that is, with previously

calculated potential, starting with $V_{sc}(z) = 0$ in the first iteration), the new values of the Fermi level, and then the potential $V_{sc}(z)$ are calculated. A weighted average of the potential from the previous and current iterations is then taken,

$$(1-\alpha)V_{sc}^{old}(z) + \alpha V_{sc}^{new}(z) \rightarrow V_{sc}^{new}(z) \tag{3.44}$$

and used in the next iteration. Typically, the relaxation parameter $\alpha \sim (0.25 - 0.3)$ gives stable calculation and reasonably good convergence. The iterations are terminated when the energies of all states calculated in two subsequent iterations differ by less than the prescribed amount.

Since the self-consistent procedure requires a large amount of calculations, i.e. finding the states at a number of (k_x, k_y) points, computation would be very slow if Equation (3.41) was used, even though the sampling may be restricted only to the irreducible wedge ($k_x > 0, k_y > 0$, and $k_x > k_y$). The procedure is accelerated by sampling (k_x, k_y) only along a single line (denoted as $k_{||}$) and using the axial approximation (in this step only). Instead of Equation (3.41) one then uses

$$p(z) = \sum_z \int \frac{2\pi k_{||} dk_{||}}{4\pi^2} \cdot f_{FD}\left[E_n(k_{||}), E_F\right] \cdot \sum_{j=1}^{6} |F_{j,n,k_{||}}(z)|^2 \tag{3.45}$$

3.2.2 Optical transition matrix elements

In electromagnetic field described by magnetic vector-potential $\overrightarrow{A}$, the interaction operator reads,

$$H_{int} = e\overrightarrow{v} \cdot \overrightarrow{A} = \frac{ie}{\hbar}\left[H, \overrightarrow{r}\right] \cdot \overrightarrow{A} \tag{3.46}$$

where $\overrightarrow{v}$ is the velocity operator, the commutator of the coordinate and the Hamiltonian operators,i.e.

$$\overrightarrow{v} = \frac{1}{i\hbar}[\overrightarrow{r}, H] \tag{3.47}$$

This is a matrix operator which acts upon the initial state wave function vector, and the resulting vector is dot-multiplied with the final wave state wave function vector and integrated over z to give the transition matrix element. The (equivalent) dipole matrix element may then be calculated by dividing this by the transition energy, i.e. $\overrightarrow{d}_{if} = \langle i|\left[\overrightarrow{r}, H\right]|f\rangle / (E_i - E_f)$.

The full derivation for this section, which uses 6×6 Hamiltonian can be found in Appendix D.

3.3 Non-linear Susceptibilities

The linear relationship between the electric polarization of a dielectric medium and the electric field of a light wave implied by Equation (3.48) below is an approximation that is only valid when the electric field amplitude is small.

$$\mathbf{P} = \varepsilon_0 \chi \mathbf{E}, \tag{3.48}$$

with

$$\mathbf{E}(t) = E_0 e^{-i\omega_0 t} + E_1 e^{-i\omega_1 t}. \tag{3.49}$$

With the widespread use of large-amplitude beams from powerful lasers, it is necessary to consider a more general form of Equation (3.48) in which the relationship between the polarization and electric field is nonlinear,

$$\mathbf{P} = \varepsilon_0(\chi^{(1)}\mathbf{E} + \chi^{(2)}\mathbf{E}^2 + \chi^{(3)}\mathbf{E}^3 + ...) \tag{3.50}$$

The first term in Equation (3.50) is the same as in Equation (3.48) and describes the linear response of the medium. $\chi^{(1)}$ can thus be identified with the linear electric susceptibility χ in Equation (3.48). The other terms describe the nonlinear response of the medium. The term in $\mathbf{E}^2$ is called the second-order nonlinear response and $\chi^{(2)}$ is called the second-order nonlinear susceptibility. Similarly, the term in $\mathbf{E}^3$ is called the third-order nonlinear response and $\chi^{(3)}$ is called the third-order nonlinear susceptibility. In general, one can write,

$$\mathbf{P}^1 = \varepsilon_0 \chi^{(1)} \mathbf{E}^1 \tag{3.51a}$$

$$\mathbf{P}^2 = \varepsilon_0 \chi^{(2)} \mathbf{E}^2 \tag{3.51b}$$

$$\mathbf{P}^3 = \varepsilon_0 \chi^{(3)} \mathbf{E}^3 \tag{3.51c}$$

$$\vdots$$

$$\mathbf{P}^n = \varepsilon_0 \chi^{(n)} \mathbf{E}^n \tag{3.51d}$$

where, for $n \geqslant 2$, $\mathbf{P}^n$ is the nth-order nonlinear polarization and χ^n is the nth-order nonlinear susceptibility. It is usually the case that the nonlinear susceptibilities have rather small magnitude. This means, when the electric field amplitude is small, the nonlinear terms are negligible and can be reverted to the linear relationship between $\mathbf{P}$ and $\mathbf{E}$ that is assumed in linear optics. On the other hand, when the electric field is large, the nonlinear terms in Equation (3.50) cannot be ignored and we enter the realm of non-linear optics which we are interested in.

3.3.1 Density Matrix Formalism

To calculate the nonlinear absorption in a medium, the perturbative solution of the density matrix is necessary [64]. The Hamiltonian $\widehat{H}$ is decomposed in two parts, the unperturbed term $\widehat{H}_0$ and the time dependent interaction potential $\widehat{V}(t)$ representing the perturbation

$$\widehat{H} = \widehat{H}_0 + \widehat{V}(t) \ , \tag{3.52}$$

and the density matrix is defined by,

$$\rho = |\psi\rangle\langle\psi| \tag{3.53}$$

By including the phenomenological damping terms, the time evolution equation for the density matrix is:

$$\dot{\rho}_{nm} = \frac{-i}{\hbar}\left[\widehat{H}, \widehat{\rho}\right]_{nm} - \Gamma_{nm}\left(\rho_{nm} - \rho_{nm}^{eq}\right) \tag{3.54}$$

$\dot{\rho}_{nm}$ is the nm element of $\dot{\rho}$, ρ_{nm}^{eq} is the equilibrium value of ρ_{nm}. For the nm element of order q of the density matrix, the following equation is obtained [65]:

$$\rho_{nm}^{(q)}(t) = \int_{-\infty}^{t} \frac{-i}{\hbar}\left[\widehat{V}(t'), \widehat{\rho}^{(q-1)}\right]_{nm} \times e^{(i\omega_{nm} - \Gamma_{nm})(t'-t)} \mathrm{d}t'. \tag{3.55}$$

3.3.2 Second Order Susceptibilities

For SPDC in coupled QW structures, only the second order nonlinearity effects are taken into account. The second-order contribution to the non-linear polar-

Table 3.1: Second-order nonlinear phenomena based on input and output of the system [1]

Effect	Input frequency	Output frequency
Frequency doubling	ω	2ω
Sum frequency mixing	ω_1, ω_2	$(\omega_1+\omega_2)$
Difference frequency mixing	ω_1, ω_2	$\lvert\omega_1-\omega_2\rvert$
Down conversion	ω_p	ω_s, ω_i
Degenerate parametric amplification	$2\omega, \omega$	ω

ization in Equation (3.51b) is given by:

$$\begin{aligned}\mathbf{P}^{(2)}(t) =&\chi^2\varepsilon_0\left[E_0^2e^{-2i\omega_0 t}+E_1^2e^{-2i\omega_1 t}+2E_0E_1e^{-i(\omega_0+\omega_1)t}\right.\\&\left.2E_0E_1^*e^{-i(\omega_0-\omega_1)t}\right]+2\chi^2\varepsilon_0\left[E_0E_0^*+E_1E_1^*\right]\end{aligned} \tag{3.56}$$

The complex amplitudes of Equation (3.56) are given by:

$$P(2\omega_0) = \chi^{(2)}E_0^2 \tag{3.57a}$$
$$P(2\omega_1) = \chi^{(2)}E_1^2 \tag{3.57b}$$
$$P(\omega_0+\omega_1) = 2\chi^{(2)}E_0E_1 \tag{3.57c}$$
$$P(\omega_0-\omega_1) = 2\chi^{(2)}E_0E_1^* \tag{3.57d}$$
$$P(0) = 2\chi^{(2)}(E_0E_0^*+E_1E_1^*). \tag{3.57e}$$

$P(2\omega_0)$ and $P(2\omega_1)$ can be referred to frequency doubling or second harmonic generation (SHG). $P(\omega_0+\omega_1)$ as sum frequency generation (SFG) and $P(\omega_0-\omega_1)$ as difference frequency generation (DFG). The last equation which is Equation (3.57e) is the optical rectification (OR). SPDC belongs to DFG category. Table 3.1 lists some of the important second-order nonlinear phenomena.

For this specific case (second order nonlinear process), Equation (3.55) turned to Equation (3.58) below

$$\rho_{nm}^{(2)} = e^{-(i\omega_{nm}-\Gamma_{nm})t}\int_{-\infty}^{t}dt'\frac{-i}{\hbar}\left[\widehat{V}(t'),\widehat{\rho}^{(1)}\right]_{nm}\times e^{(i\omega_{nm}-\Gamma_{nm})t'}, \tag{3.58}$$

while Equation (3.59) relates the second order polarization to the second order nonlinear susceptibility tensor

$$\mathbf{P}^{(2)}\left(\omega_p+\omega_q\right)=\sum_{jk}\sum_{(pq)}\chi^{(2)}_{ijk}\left(\omega_p+\omega_q,\omega_p,\omega_q\right)\times E_j(\omega_q)E_k(\omega_p). \tag{3.59}$$

General case of $(\chi^{(2)}_{ijk})$ in Equation (3.59) can be defined as.

$$\begin{aligned}\chi^{(2)}\left(\omega_p+\omega_q;\omega_p,\omega_q\right)=&\frac{e^3N}{2\varepsilon_0\hbar^2}\sum_{lmn}\left(\rho^{(0)}_{ll}-\rho^{(0)}_{mm}\right)\\&\left\{\frac{d^x_{ln}d^y_{nm}d^z_{ml}}{\left[\left(\omega_{nl}-\omega_p-\omega_q\right)-i\Gamma_{nl}\right]\left[\left(\omega_{ml}-\omega_p\right)-i\Gamma_{ml}\right]}\right.\\&+\frac{d^x_{ln}d^z_{nm}d^y_{ml}}{\left[\left(\omega_{nl}-\omega_p-\omega_q\right)-i\Gamma_{nl}\right]\left[\left(\omega_{ml}-\omega_q\right)-i\Gamma_{ml}\right]}\\&+\frac{d^y_{ln}d^x_{nm}d^z_{ml}}{\left[\left(\omega_{nm}+\omega_p+\omega_q\right)+i\Gamma_{nm}\right]\left[\left(\omega_{ml}-\omega_p\right)-i\Gamma_{ml}\right]}\\&\left.+\frac{d^z_{ln}d^x_{nm}d^y_{ml}}{\left[\left(\omega_{nm}+\omega_p+\omega_q\right)+i\Gamma_{nm}\right]\left[\left(\omega_{ml}-\omega_q\right)-i\Gamma_{ml}\right]}\right\},\end{aligned} \tag{3.60}$$

with e is the electron charge, ε_0 is the free space permittivity, ω_p, ω_q and $\omega_p+\omega_q$ are the frequencies of three photons interacting in the nonlinear system,

For one-dimensional case $\left(\chi^{(2)}_{zzz}\right)$, Equation (3.60) can be written as,

$$\begin{aligned}\chi^{(2)}\left(\omega_p+\omega_q;\omega_p,\omega_q\right)=&\frac{e^3N}{2\varepsilon_0\hbar^2}\sum_{lmn}\left(\rho^{(0)}_{ll}-\rho^{(0)}_{mm}\right)d_{ln}d_{nm}d_{ml}\\&\left\{\frac{1}{\left[\left(\omega_{nl}-\omega_p-\omega_q\right)-i\Gamma_{nl}\right]\left[\left(\omega_{ml}-\omega_p\right)-i\Gamma_{ml}\right]}\right.\\&+\frac{1}{\left[\left(\omega_{nl}-\omega_p-\omega_q\right)-i\Gamma_{nl}\right]\left[\left(\omega_{ml}-\omega_q\right)-i\Gamma_{ml}\right]}\\&+\frac{1}{\left[\left(\omega_{nm}+\omega_p+\omega_q\right)+i\Gamma_{nm}\right]\left[\left(\omega_{ml}-\omega_p\right)-i\Gamma_{ml}\right]}\\&\left.+\frac{1}{\left[\left(\omega_{nm}+\omega_p+\omega_q\right)+i\Gamma_{nm}\right]\left[\left(\omega_{ml}-\omega_q\right)-i\Gamma_{ml}\right]}\right\}\end{aligned} \tag{3.61}$$

3.3.3 Second Harmonic Generation (SHG)

Equation (3.61) is general equation for one dimensional second order nonlinear intersubband absorption process in three level system. For example, for SHG, $\chi^{(2)}$, when only one incident photon frequency ω exist (monochromatic pump laser) $\omega_p = \omega_q = \omega$, Equation (3.61) can be simplified to Equation (3.62) below:

$$\begin{aligned}\chi^{(2)}(2\omega,\omega,\omega) =& \frac{e^3}{L_z\varepsilon_0\hbar^2}\left(\frac{d_{13}d_{32}d_{21}}{\omega_{31}-2\omega-i\Gamma_{31}}\right) \\ &\times\left[\frac{n_1-n_2}{\omega_{21}-\omega-i\Gamma_{21}}+\frac{n_3-n_2}{\omega_{32}-\omega-i\Gamma_{32}}\right],\end{aligned} \tag{3.62}$$

where d_{ij} are the transition dipole matrix elements, L_z is the length of the structure, n_i is the electron sheet densities in the ground state ($i = 1$), first excited state ($i = 2$) and second excited state ($i = 3$), ω_{ij} the transition frequency ($\omega_{ij} < 0$ for $i < j$) and Γ_{ij} are the off-diagonal relaxation rates ($i \to j$ transition line widths). Derivation to simplified Equation (3.61) to (3.62) can be referred in Appendix A.

Electrons normally only populate the lowest energy level (ground state) and the off-diagonal relaxation rates are taken to be equal, $\Gamma_{12} = \Gamma_{23} = \Gamma_{31} \equiv \Gamma$. So $n_3 = n_2 = 0$ and $n_1 = N$, Equation (3.62) then reduces to

$$\chi^{(2)} = \frac{Ne^3}{\hbar^2 L_z\varepsilon_0}\Pi^{(2)}, \tag{3.63}$$

with,

$$\Pi^{(2)} = \left\| \frac{d_{12}d_{23}d_{31}}{(\omega_{31}-2\omega-i\Gamma)(\omega_{21}-\omega-i\Gamma)} \right\|. \tag{3.64}$$

The SHG process with monochromatic pump is illustrated in Figure 3.2.

3.3.4 Theory of SPDC

The geometry and energy level diagram describing the SPDC process are given in Figure 2.5. Using similar methods in Appendix A and referring to Figure 2.5 (b), only Equation (1f) give high value for $\chi^{(2)}$ SPDC. Then for this case, Equation (3.61) can be reduced to:

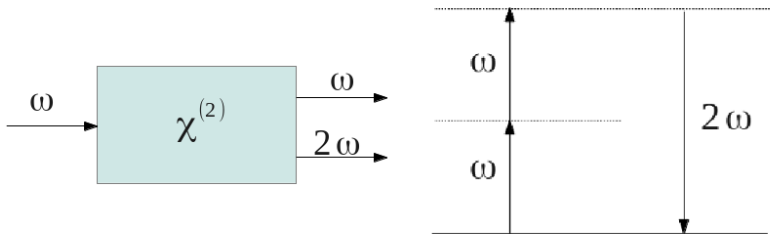

Figure 3.2: (a) Geometry of SHG. (b) Energy-level diagram describing SHG

$$\begin{aligned}\chi^{(2)}\left(\omega_s,\omega_p,-\omega_i\right) =& \frac{e^3 N}{2\varepsilon_0\hbar^2}\frac{(\rho_{11}^{(0)}-\rho_{33}^{(0)})d_{12}d_{23}d_{31}}{\left[(\omega_{21}+\omega_i-\omega_p)-i\Gamma_{21}\right]\left[(\omega_{31}-\omega_p)-i\Gamma_{31}\right]} \\ =& \frac{e^3 d_{12}d_{23}d_{31}}{2\varepsilon_0 L_z\hbar^2}\frac{(n_1-n_3)}{\left[(\omega_{21}-\omega_s)-i\Gamma_{21}\right]\left[(\omega_{31}-\omega_p)-i\Gamma_{31}\right]}\end{aligned} \tag{3.65}$$

For exact resonance case, $\omega_{21}=\omega_s, \omega_{32}=\omega_i, \omega_{31}=\omega_p$ and considering realistic n-doped QWs in thermal equilibrium which only the ground level well is populated ($n_3 \ll n_1$), Equation (3.65) reduces to:

$$\chi^{(2)}_{\text{resonant}}\left(\omega_s,\omega_p,-\omega_i\right) = \frac{e^3 n_1}{2\varepsilon_0 L_z}\frac{d_{12}d_{23}d_{31}}{(\hbar\Gamma)^2} \tag{3.66}$$

In the preliminary work (Ground work in Chapter 4), the discussion and results were focused on SHG since most of previous work was done in this area. Studies on SPDC can be seen as extended version of work on SHG since both of them are second order non-linear problems. Comparing our preliminary results with previous work in SHG should show that the procedure is correct, and can be extended to SPDC, towards designing a highly efficient entangled photon source based on coupled QW.

3.4 Third Order Nonlinear Interaction

Two schemes of third order nonlinear interaction that are discussed are defined in Figure 3.3, with conservation of energy for Figure 3.3(a) and Figure 3.3(b) as

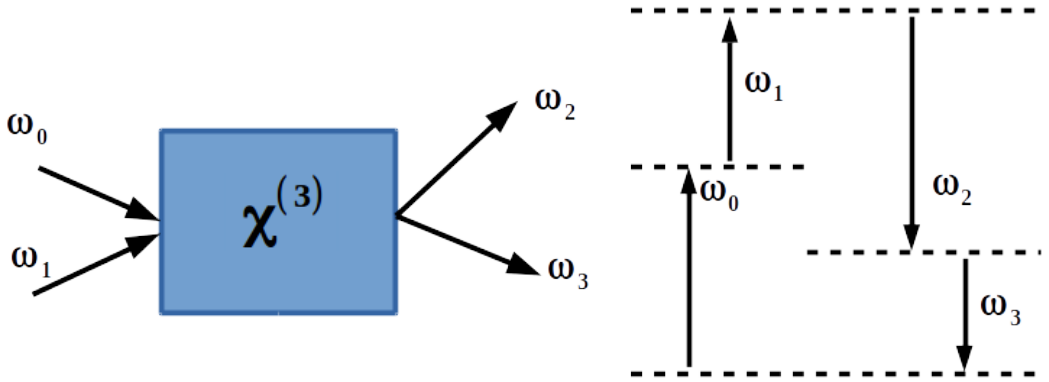

(a)

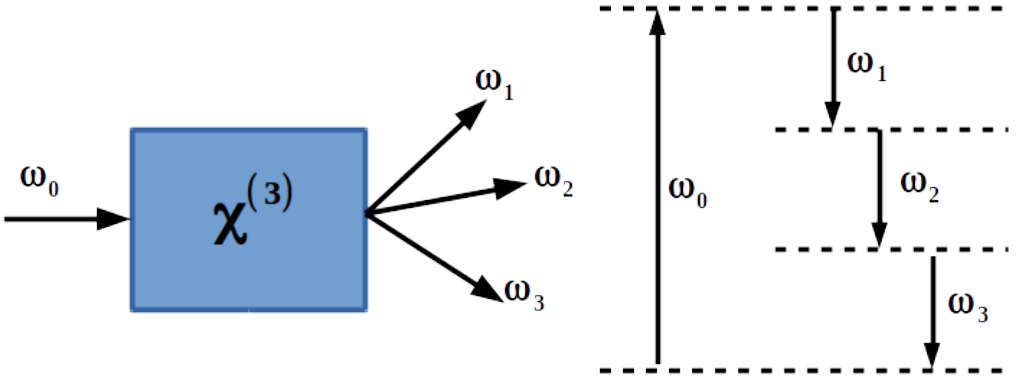

(b)

Figure 3.3: Two schemes of third order nonlinear process (a) Spontaneous four wave mixing (SFWM) and (b) Third order spontaneous parametric down conversion (TOSPDC)

below

$$\hbar\omega_0 + \hbar\omega_1 = \hbar\omega_2 + \hbar\omega_3 \tag{3.67a}$$

$$\hbar\omega_0 = \hbar\omega_1 + \hbar\omega_2 + \hbar\omega_3 \tag{3.67b}$$

respectively.

Two-photon absorption, nonlinear refractive index, solitons, four wave mixing,Raman scattering and phase conjugation are (various) third order nonlinear processes that are bound to Equation (3.67a). While Equation (3.67b) is the conservation of energy for third order spontaneous parametric down conversion (TOSPDC) process that we are interested in (Chapter 7). This process involved one pump photon ($\hbar\omega_0$) that is down converted to three entangled photon ($\hbar\omega_1, \hbar\omega_2, \hbar\omega_3$) at the output of the nonlinear medium which in our case is a QW structure.

The reverse process of TOSPDC is called third order harmonic generation (THG) that involved summation of three pump photons ($\hbar\omega_1 = \hbar\omega_2 = \hbar\omega_3$) at the input and produced 1 pump photon with the energy of $3\hbar\omega_1$.

3.4.1 Theory of TOSPDC

TOSPDC is suggested to be the direct source of GHZ state and this process can be refer to the Figure 3.3(b). TOSPDC could produce three photon entanglement in continuous degrees of freedom such as energy and momentum. Boyd in his book [p182] derived general third order susceptibility $\chi^{(3)}$ as equation below,

$$\chi^{(3)}_{kijh}(\omega_p+\omega_q+\omega_r;\omega_p,\omega_q,\omega_r) = \frac{N}{\varepsilon_0\hbar^3}\mathcal{P}_I \sum_{nvml}$$
$$\left\{ \frac{(\rho^{(0)}_{mm}-\rho^{(0)}_{ll})\mu^k_{mn}\mu^j_{nv}\mu^i_{vl}\mu^h_{lm}}{[\omega_{nm}-\omega_p-\omega_q-\omega_r-i\Gamma_{nm}]\,[\omega_{vm}-\omega_p-\omega_q-i\Gamma_{vm}]\,[\omega_{lm}-\omega_p-i\Gamma_{lm}]} \right.$$
$$- \frac{(\rho^{(0)}_{ll}-\rho^{(0)}_{vv})\mu^k_{mn}\mu^j_{nv}\mu^i_{lm}\mu^h_{vl}}{[\omega_{nm}-\omega_p-\omega_q-\omega_r-i\Gamma_{nm}]\,[\omega_{vm}-\omega_p-\omega_q-i\Gamma_{vm}]\,[\omega_{vl}-\omega_p-i\Gamma_{vl}]}$$
$$- \frac{(\rho^{(0)}_{vv}-\rho^{(0)}_{ll})\mu^k_{mn}\mu^j_{vm}\mu^i_{nl}\mu^h_{lv}}{[\omega_{nm}-\omega_p-\omega_q-\omega_r-i\Gamma_{nm}]\,[\omega_{nv}-\omega_p-\omega_q-i\Gamma_{nv}]\,[\omega_{lv}-\omega_p-i\Gamma_{lv}]}$$
$$\left. + \frac{(\rho^{(0)}_{ll}-\rho^{(0)}_{nn})\mu^k_{mn}\mu^j_{vm}\mu^i_{lv}\mu^h_{nl}}{[\omega_{nm}-\omega_p-\omega_q-\omega_r-i\Gamma_{nm}]\,[\omega_{nv}-\omega_p-\omega_q-i\Gamma_{nv}]\,[\omega_{nl}-\omega_p-i\Gamma_{nl}]} \right\} \tag{3.68}$$

$\mathcal{P}_I$ in Equation (3.68) is the intrinsic permutation operator which means that in the summation one takes all possible permutations of the input frequencies ω_p, ω_q and ω_r with the cartesian indices h, i, j permuted simultaneously.

Chapter 4

Groundwork

This chapter shows the groundwork for the whole thesis. It is done during the first year of the research. This work focuses on SHG rather than SPDC since SHG work is well known and easy to understand and replicate. And the fact that, SPDC is just a reverse process of SHG, studies of SHG process can be the starting point to all our work. For the record, in this chapter, no genetic optimization is done, and the calculation is purely based on resonant process.

4.1 Second Harmonic Generation

4.1.1 Resonant Input

By using Equation (3.63) we tried to find what input frequency gives the maximum nonlinear susceptibility for SHG. In this section, we used double QW structures that have $\omega_{12} \simeq \omega_{23} = 99\text{meV}/\hbar$. In Figure 4.1. ω_{12} is the energy difference between green and red line while ω_{23} is the energy difference between blue and green line.

The well width of the first well is taken to be $cw_1 = 20.0$ Å, the barrier potential is kept constant at $V_0 = 400\text{meV}$ (aluminium mole fraction in barrier $x = 0.48$) with barrier width of $w_b = 6.0$ Å and the second well width is $cw_2 = 83.0$ Å. The ω in Equation (3.63) was varied from $-300\text{meV}/\hbar$ to $300\text{meV}/\hbar$ and the result are plotted in Figure 4.2.

Figure 4.2 shows that the maximum nonlinear susceptibility for SHG case

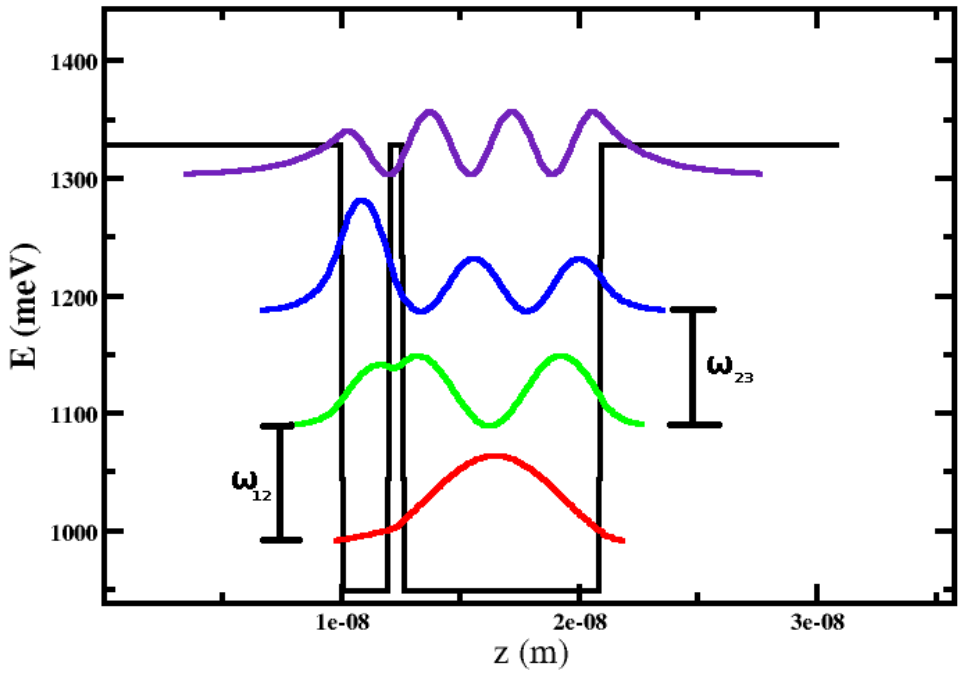

Figure 4.1: The potential (conduction band edge) in asymmetric coupled QW structure

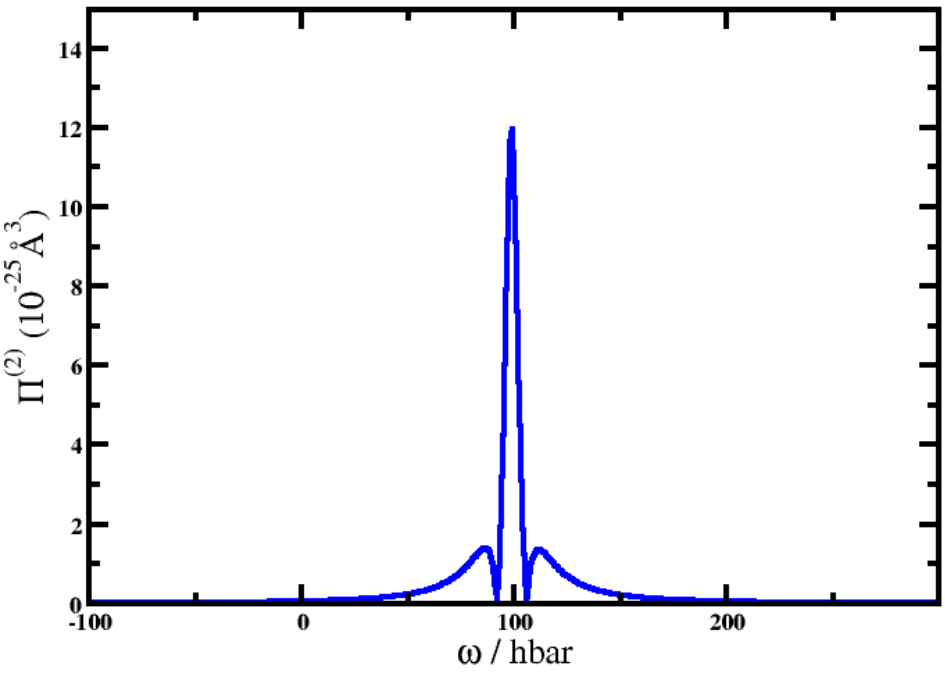

Figure 4.2: Plot of $\Pi^{(2)}$

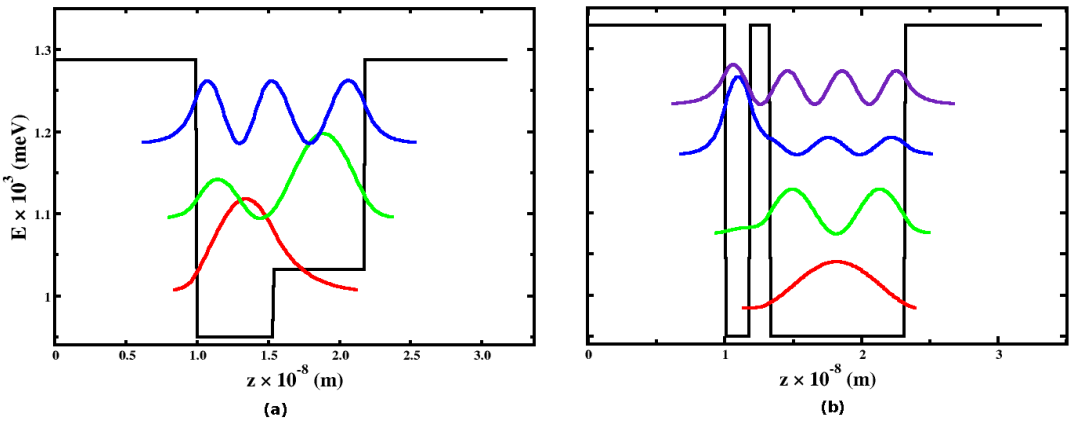

Figure 4.3: (a) Single step structure. (b) Asymmetric coupled QW structure

occurred when the input pump frequency is equal to 99meV/$\hbar$. This pump frequency is resonant with the energy difference for three lowest levels in Figure 4.1. From this result, we can simplify Equation (3.63) to Equation (4.1) by using resonant conditions $\omega_{12} = \omega_{23} = \omega$ which maximizes the nonlinear susceptibility and making efficient SHG in QWs possible.

$$\chi^{(2)}_{\text{resonant}} = \frac{e^3}{L_z \varepsilon_0 (\hbar\Gamma)^2} \Pi^{(2)}_{\text{resonant}} \tag{4.1}$$

$$\Pi^{(2)}_{\text{resonant}} = \|d_{12} d_{23} d_{31}\|$$

4.2 Maximization of Resonant $\chi^{(2)}$ Using Brute Force Method

In this section, the main goal is to find the best potential QW heterostructure that gives highest $\chi^{(2)}_{\text{resonant}}$, i.e. the product of matrix element $\Pi^{(2)}_{\text{resonant}}$ in Equation (4.1). This method computes $\Pi^{(2)}_{\text{resonant}}$ for all possible structures by fixing barrier potential but varying the well width, step width and step potential height in Section 4.2.1 (Single Step Quantum Well), while in Section 4.2.2 (Coupled Quantum Well), the barrier potential is fixed. The first well, barrier and second well widths are varied until the resonant condition is found and then $\Pi^{(2)}_{\text{resonant}}$ computed.

4.2.1 SHG in Step Quantum Well

Figure 4.3(a) shows the single step QW used in this section. The barrier potential was kept at $V_0 = 340$meV which corresponds to aluminium mole fraction $x = 0.41$ in the barrier material. The pump photon radiation was chosen to be $\hbar\omega = 100$meV ($\lambda \simeq 12.4\mu$m GaAs-based quantum cascade laser operating at room temperature [66]).

Figure 4.4(a) shows the largest value of the dipole matrix element product around 4000 Å^3 was obtained for a well width of $c_w = 40$Å. The corresponding values of the step width $c_s = 63$ Å and the step potential $V_s = 123$meV which can be refer to Figure 4.4(b). This result is close to that obtained by semi-analytical method in [59] Page 378.

4.2.2 SHG in Double Quantum Well

Figure 4.3(b) shows asymmetric coupled QW structure used in this section. The barrier potential was kept at $V_0 = 400$meV which corresponds to aluminium mole fraction $x = 0.48$ in the barrier material. The pump photon radiation is chosen to be $\hbar\omega = 100$meV ($\lambda \simeq 12.4\mu$m GaAs-based quantum cascade laser operating at room temperature [66]).

Figure 4.5(a) shows that the largest value of the dipole matrix element product is 4042 Å^3, which was obtained for a well width of $c_{w1} = 26$ Å. The corresponding values of the second well width $c_{w2} = 67$ Å and the barrier width of $c_b = 7$Å, as shown to Figure 4.5(b). This result is also close to the result of semi-analytical method in [59] Page 380.

All constants in Section 4.2.1 and 4.2.2 are taken the same as in previous work [59], so that results in this chapter are comparable and easily validated. Brown line in Figures 4.4 and 4.5 are the data extracted from [59] and it can be seen that the well and barrier width in both Figures are similar to our results, but not the $\Pi^{(2)}$ values. The reason behind this is that our methods include the nonparabolicity in $\Pi^{(2)}$ calculations in contrast to those in [59]. The fact that the patterns are very similar for the $\Pi^{(2)}$ values, and exactly the same for barrier and well width, confirms that our calculations are correct and can be used in further investigations.

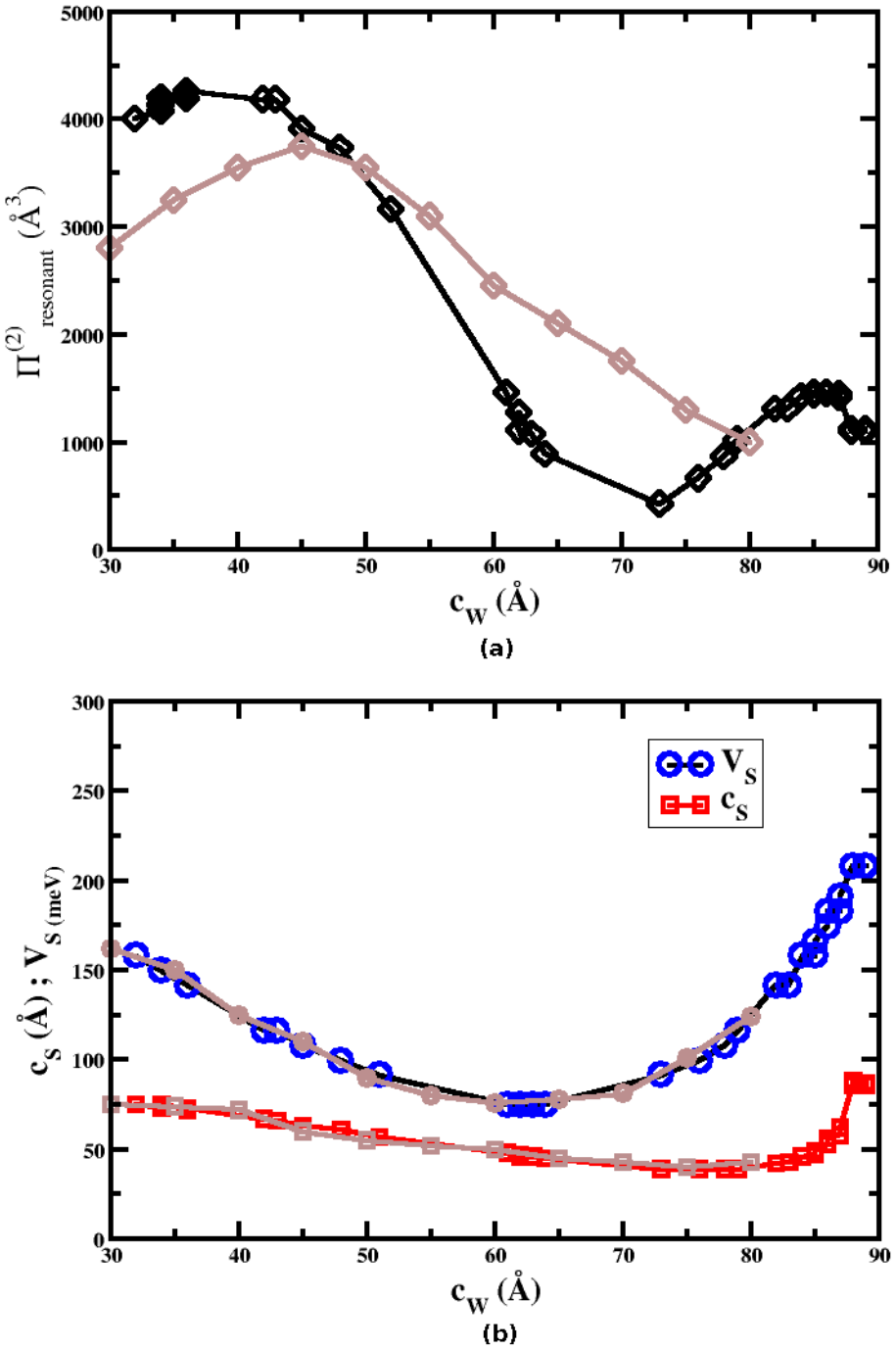

Figure 4.4: Optimization of an $Al_xGa_{1-x}As$ single step QW under double resonance condition, $\hbar\omega = 100$meV. (a) The product of matrix elements $\Pi^{(2)}_{\text{resonant}}$ as it depends on the choice of well width, (b) Step witdh and step potential as a function of well width.

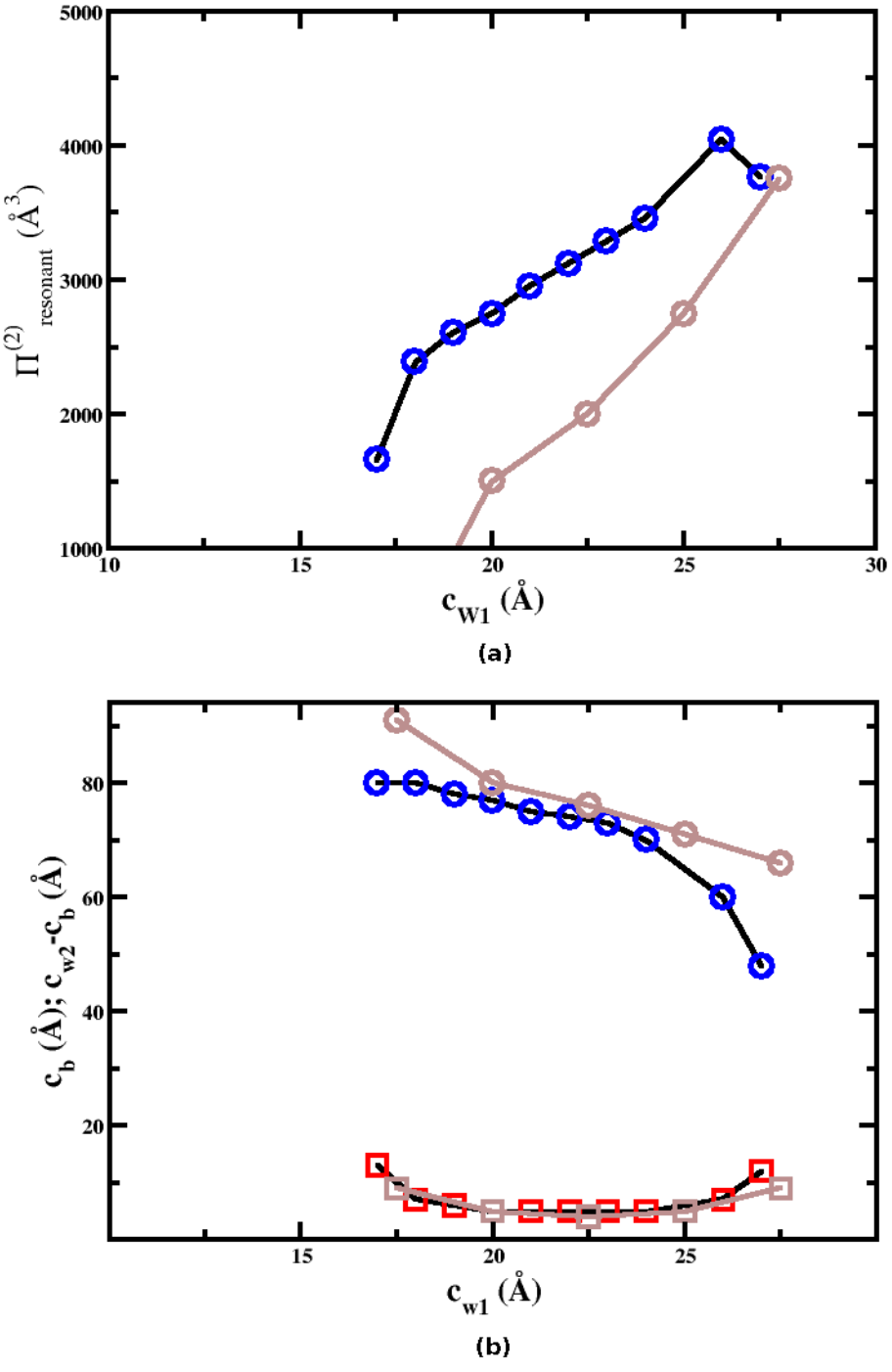

Figure 4.5: Optimization of an $Al_xGa_{1-x}As/GaAs$ asymmetric coupled QWs under double resonance condition, $\hbar\omega = 100$meV. The barrier height was kept constant at $V_0 = 400$meV. (a) The product of matrix elements $\Pi^{(2)}$ as a function of the first well width (c_{w1}), (b) The barrier thickness and the second well width as a function of the first well width (c_{w1}).

4.3 Conclusion

In this Chapter, we successfully replicated the optimization process for SHG in double and step QW. The results in Section 4.2 are close to those obtained by semi-analytical method in [59] Page 378. With this finding, we confirmed that our method and calculation of $\chi^{(2)}$ is correct and can be applied to SPDC and TOSPDC problems using general equation for nonlinear susceptibility as discussed in Chapter 3.

Chapter 5

SPDC in Intersubband transition at Conduction Band

This chapter is based on the published reference [67]: "Mid-infrared entangled photon generation in optimised asymmetric semiconductor quantum wells" [R. Razali, A. Valavanis, J. D. Cooper, Z. Ikonić, D. Indjin, and P. Harrison *Superlattices and Microstructures*, **90**, 107-116 (2016)].

5.1 Introduction

Generation of entangled photons, and of heralded single photons, is a very important ingredient in a variety of quantum information technologies. Experimental implementation of these techniques, using optics, requires a reliable source of correlated/entangled and single photons. This is usually implemented by SPDC process in a nonlinear optical medium with non-zero second order susceptibility, where the pump photon gets split into a 'signal' and 'idler' photon. The twin photons are usually polarisation-entangled. However, one can also use the spectral (frequency) entanglement of the photon pair.

In the visible or near-infrared wavelength range, the commonly used materials for this purpose are nonlinear optical crystals like lithium niobate, which have relatively large nonresonant nonlinear susceptibility. There are bulk materials which are good in the mid-infrared range, however at these longer wavelengths

one can also take advantage of much larger resonant nonlinearities achievable in semiconductor heterostructures, based on intersubband transitions between size-quantized states therein. Second-order nonlinearity is available in asymmetric semiconductor QW structures. High nonlinearity appears in relatively narrow ranges of photon energies, near the transition resonances, which are typically in the mid-infrared range. In contrast to SPDC based on conventional nonlinear crystals, which enable different polarizations of signal and idler photons, and hence the polarization entanglement, a specific feature of Γ-valley intersubband transitions is that their nonlinearity exists only for light polarization perpendicular to the QWs, hence disabling polarization entanglement. This type of SPDC is also known as type-0 parametric process. Here we consider the design of high efficiency frequency-entangled photon sources by optimizing the profile of semiconductor QWs so to obtain maximal second order nonlinear susceptibility, and consider the efficiency of spectrally entangled twin photon generation.

5.2 SPDC generation of twin photons in quantum wells

The SPDC process is illustrated in Figure 2.5. The photon-pair generation is a second order nonlinear process in which a pump photon with frequency ω_p is spontaneously converted into two photons with lower energy, called signal and idler photons, with frequencies ω_s and ω_i respectively. The process is allowed in materials with non-zero second order susceptibility.

For SPDC process, the maximally entangled Bell-states will take form as,

$$|\psi^{\pm}\rangle = \frac{1}{\sqrt{2}}(|01\rangle \pm |10\rangle), \tag{5.1}$$

with

$$\begin{aligned} |01\rangle &= |0\rangle \otimes |1\rangle \\ |10\rangle &= |1\rangle \otimes |0\rangle \end{aligned} \tag{5.2}$$

and for this case, $|0\rangle = |\omega_1, Z\rangle$, $|0\rangle = |\omega_2, Z\rangle$ with $\omega_1 + \omega_2 = \omega_3$

Generally, resonantly enhanced susceptibility in QWs is accompanied by a large absorption, which in its own right, unrelated to phase-matching issues, leads to a limited useful interaction length in such structures.

Since SPDC is a second order nonlinear process, the polarization of SPDC is defined by Equation (3.51b) which rewrite in Equation (**??**).

$$\mathbf{P} = \varepsilon_0 \chi^{(2)} \mathbf{E}^2 \ . \tag{5.3}$$

The second-order nonlinear susceptibility ($\chi^{(2)}$) is calculated using Equation 3.61 which rewrite in Equation (5.4:

$$\begin{aligned}
\chi^{(2)}\left(\omega_p+\omega_q,\omega_p,\omega_q\right) = \frac{e^3 N}{2\varepsilon_0\hbar^2}\sum_{lmn}\left(\rho_{ll}^{(0)}-\rho_{mm}^{(0)}\right) d_{ln}d_{nm}d_{ml} \\
\left\{\frac{1}{\left[\left(\omega_{nl}-\omega_p-\omega_q\right)-i\Gamma_{nl}\right]\left[\left(\omega_{ml}-\omega_p\right)-i\Gamma_{ml}\right]}\right. \\
+\frac{1}{\left[\left(\omega_{nl}-\omega_p-\omega_q\right)-i\Gamma_{nl}\right]\left[\left(\omega_{ml}-\omega_q\right)-i\Gamma_{ml}\right]} \\
+\frac{1}{\left[\left(\omega_{nm}+\omega_p+\omega_q\right)+i\Gamma_{nm}\right]\left[\left(\omega_{ml}-\omega_p\right)-i\Gamma_{ml}\right]} \\
\left.+\frac{1}{\left[\left(\omega_{nm}+\omega_p+\omega_q\right)+i\Gamma_{nm}\right]\left[\left(\omega_{ml}-\omega_q\right)-i\Gamma_{ml}\right]}\right\}
\end{aligned} \tag{5.4}$$

where ω_p and ω_q are the input, and $\omega_p+\omega_q$ the output photon frequencies, and Γ_{ij} are the linewidths. The total electron density is N, and $N\rho_{ii}^{(0)}$ is the electron density in quantised state i. The summation over lmn in Equation (5.4) goes over all states in the system. The d_{ij} in Equation (5.4) is the dipole transition matrix element, and for Γ-valley intersubband transitions it has only the z-component (perpendicular to the QW layer plane), so $\chi^{(2)}$ denotes the $\chi_{zzz}^{(2)}$ component of the susceptibility tensor.

Dipole matrix elements are calculated from the wave functions of states in the QW structure, obtained by solving the effective-mass Schrödinger equation. We have here used the effective-mass model with nonparabolicity, and the Schrödinger equation was solved by linearisation of the nonlinear matrix eigenvalue problem, as described in detail in Chapter 3. In this case the d_{ij} cannot be calculated from the conventional expression $\langle\psi_i|\,\hat{z}\,|\psi_j\rangle$, as can be easily checked by varying

the origin of the coordinate z (this changes the calculated values of d_{ij}, because of wavefunctions' non-orthogonality if the nonparabolicity is accounted for). Instead, the matrix elements of the momentum operator ($P_z = i\hbar\dfrac{d}{dz}$) are first calculated from [68]:

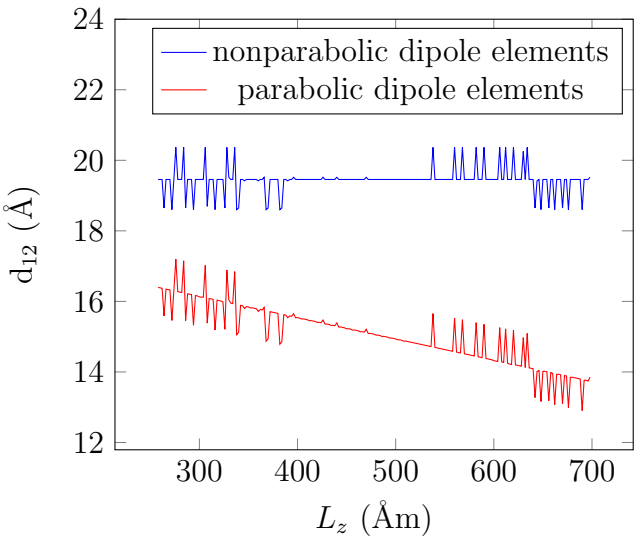

Figure 5.1: Effect of the well width on nonparabolic dipole matrix elements (blue line) and parabolic dipole matrix elements (red line).

$$\langle\psi_i|\,\widehat{P}\,|\psi_j\rangle = \frac{1}{2}\langle\psi_i|\,P_z\frac{m_0}{m(E_i,z)} + \frac{m_0}{m(E_j,z)}P_z\,|\psi_j\rangle \quad , \tag{5.5}$$

with $P_z = i\hbar\dfrac{d}{dz}$. Equation (5.5) then can be expanded as,

$$\langle\psi_i|\,\widehat{P}\,|\psi_j\rangle = \frac{m_0}{2}\langle\psi_i|\,P_z\frac{m_0}{m(E_i,z)} + \frac{m_0}{m(E_j,z)}P_z\,|\psi_j\rangle \tag{5.6a}$$

$$= \frac{m_0}{2}\langle\psi_i|\,i\hbar\frac{d}{dz}\frac{1}{m(E_i,z)} + \frac{1}{m(E_j,z)}i\hbar\frac{d}{dz}\,|\psi_j\rangle \tag{5.6b}$$

$$= \frac{i\hbar m_0}{2}\left[\int_0^z \psi_i\frac{d}{dz}\left(\frac{\psi_j}{m(E_i,z)}\right)dz + \int_0^z \psi_i\frac{1}{m(E_j,z)}\frac{d\psi_j}{dz}dz\right]. \tag{5.6c}$$

This equation depends on the nonparabolic effective mass. As we know, there is commutation relation between momentum operator and position Equation

(5.7).

$$\widehat{P} = \frac{im_0}{\hbar}\left[\widehat{H}, \widehat{z}\right]. \tag{5.7}$$

By making use of Equation(5.7), $\langle\psi_i|\,\widehat{P}\,|\psi_j\rangle$ in Equation (5.5) can be defined as,

$$\langle\psi_i|\,\widehat{P}\,|\psi_j\rangle = \frac{im_0}{\hbar}\left[\langle\psi_i|\,\widehat{H}\widehat{z}\,|\psi - j\rangle - \langle\psi_i|\,\widehat{z}\widehat{H}\,|\psi - j\rangle\right] \tag{5.8a}$$

$$= \frac{im_0}{\hbar}\left[\langle\widehat{H}\psi_i|\,\widehat{z}\,|\psi - j\rangle - \langle\psi_i|\,\widehat{z}\,|\widehat{H}\psi - j\rangle\right] \tag{5.8b}$$

$$= \frac{im_0}{\hbar}\left[E_i\,\langle\psi_i|\,\widehat{z}\,|\psi - j\rangle - E_i\,\langle\psi_i|\,\widehat{z}\,|\psi - j\rangle\right] \tag{5.8c}$$

$$= \frac{im_0}{\hbar}(E_i - E_j)\,\langle\psi_i|\,\widehat{z}\,|\psi_j\rangle \tag{5.8d}$$

By rearranging Equation (5.8d), the dipole matrix can be written as,

$$\langle\psi_i|\,\widehat{z}\,|\psi_j\rangle = \frac{\hbar}{im_0}\frac{\langle\psi_i|\,\widehat{P}\,|\psi_j\rangle}{E_i - E_j}. \tag{5.9}$$

Inserting Equation (5.6c) to Equation (5.9), the dipole matrix element now can be written as,

$$\langle\psi_i|\,\widehat{z}\,|\psi_j\rangle = -\frac{\hbar^2/2}{E_i - E_j}\left[\int_0^z \psi_i \frac{d}{dz}\left(\frac{\psi_j}{m(E_0, z)}\right)dz + \int_0^z \psi_i \frac{1}{m(E_j, z)}\frac{d\psi_j}{dz}dz\right] \tag{5.10a}$$

Using Equation (5.10), the dipole matrix elements are now independent on the choice of the coordinate origin as can be referred to Figure 5.1 (blue line).

So here we successfully derived a non-parabolic dipole matrix element that can be used to calculate the transition dipole moment of electron from $|\psi_i\rangle$ to $|\psi_j\rangle$ in non-parabolic system.

5.3 Optimization of Heterostructure for SPDC

Structural optimization for SPDC aims to find the global maximum of $\chi^{(2)}$ value, among all possible QW designs. These may generally include arbitrary smooth or abrupt potentials, coming from appropriate variation of the AlGaAs alloy composition, and in cases of susceptibilities relevant for the second harmonic generation, third harmonic generation, or optical rectification, has been the subject of numerous studies, based on a variety of methods. Here we restrict considerations to the (practically most interesting) case of multiple rectangular QWs made of the same material (GaAs) and barriers made from another single material composition (AlGaAs). A single rectangular (hence symmetric) QW gives $\chi^{(2)} = 0$, as do all the symmetric multi QWs (MQWs), because the cyclic product of matrix elements in Equation (5.2) is zero therein, but unequal-width double QWs (DQW), or MQWs are acceptable candidates.

Figure 5.2 shows the plot of $\chi^{(2)}$ value based on a combination of two different well's width with fixed barrier. The step length is $1\mathring{A}$. To generate this kind of data it takes more than a day to finish. So if we have varied the barrier width as well, the computation time will increase exponentially. In fact, if we focus on different number of QWs, the computation time is not acceptable. So it is not wise to use this method to find the best QW structure that can provide high value of $\chi^{(2)}$.

Since an extensive search over the parameter space is too demanding even for the simplest, double QW structure which has the two well widths and the barrier width describing its shape, we have used a genetic algorithm to find the global maximum of $\chi^{(2)}$. This starts with an arbitrary DQW (or MQW) structure, and varies the layer widths, one at a time, initially with a large step length (50Å), in order to perform the initial 'scan' of the parameter space, and keeps twenty best structures as 'parents'. The initial width for each well and barrier is set to 2Å and the maximum width allowed is 100Å. The step length is then halved and the best structure between all daughter structures, coming from each parent, is kept. In this calculation the daughter structures were obtained by directly mutating the parents individually, without cross-fertilization between different parents. The search for the maximum is repeated until the step length is 1Å,

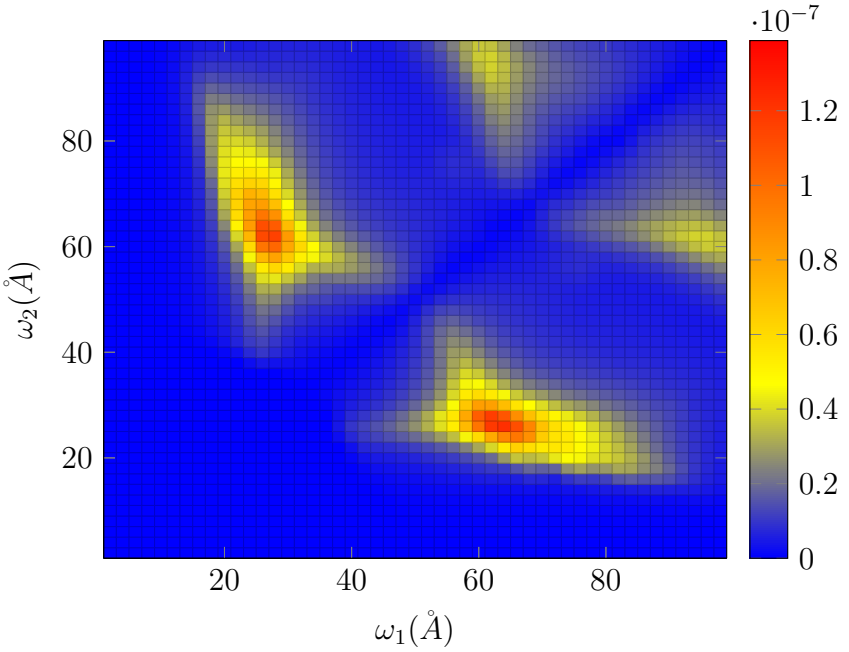

Figure 5.2: $\chi^{(2)}$ value with two varied QW width

which is the smallest step that can be realistically guaranteed experimentally. The method is computationally reasonably fast in finding the global maximum of $\chi^{(2)}$. Certainly, in exceptional cases it may happen that the method finds only a local, rather than global maximum, but even then the result is practically useful.

Table 5.1 shows different QW structures, optimised for $\chi^{(2)}$, found by this method, for different nonlinear interactions: SPDC denotes the spontaneous parametric downconversion, followed by a number which denotes the idler photon energy in meV that was used in the design. Since the meaning of signal and idler in the SPDC case is interchangeable, a structure name is chosen to be consistent with Figure 2.5. E.g., the SPDC50 structure produces 50 meV and 150 meV photons, just as SPDC150 does, but the former has the property that the intermediate state in it is $\hbar\omega_s \approx 150$ meV from the ground state. It is interesting to note that the optimisation procedure delivers the SPDC50 energy configuration as globally optimal, i.e. having a larger $\chi^{(2)}$ than that achievable in the best – but in fact only locally optimal – SPDC150 structure (the latter could be found by putting additional constraints in the optimisation procedure). So, each entry in Table 5.1 corresponds to a particular nonlinear process in a particular optimised

Table 5.1: The optimized structures with different number of QWs, for various SPDC cases - either nearly degenerate or very non-degenerate. The layer widths are given in Å, with the outermost layers being the barriers.

	Double-QW	**Triple-QW**	**Quad-QW**
SPDC99	100/27/10/61/100 $\chi^{(2)}$ =1.2879e-7	100/22/6/10/6/57/100 $\chi^{(2)}$ =1.3079e-7	100/12/5/19/10/50/2/9/100 $\chi^{(2)}$ =1.2687e-7
SPDC98	100/27/10/61/100 $\chi^{(2)}$ =1.2758e-7	100/22/6/10/6/57/100 $\chi^{(2)}$ =1.2709e-7	100/12/5/19/10/50/2/9/100 $\chi^{(2)}$ =1.2332e-7
SPDC97	100/26/10/62/100 $\chi^{(2)}$ =1.1890e-7	100/21/5/10/7/58/100 $\chi^{(2)}$ =1.2137e-7	100/12/5/19/10/50/2/9/100 $\chi^{(2)}$ =1.1784e-7
SPDC96	100/26/10/62/100 $\chi^{(2)}$ =1.1279e-7	100/58/5/11/7/20/100 $\chi^{(2)}$ =1.1438e-7	100/21/4/9/7/55/5/4/100 $\chi^{(2)}$ =1.1251e-7
SPDC67	100/20/17/60/100 $\chi^{(2)}$ =7.4714e-8	100/59/8/5/9/18/100 $\chi^{(2)}$ =7.6715e-8	100/7/2/11/9/8/9/58/100 $\chi^{(2)}$ =7.6799e-8
SPDC50	100/17/21/60/100 $\chi^{(2)}$ =7.5064e-8	100/14/11/9/15/58/100 $\chi^{(2)}$ =7.9230e-8	100/23/13/17/12/14/15/58/100 $\chi^{(2)}$ =7.6047e-8

structure. All structures in Table 5.1 are GaAs QWs embedded in AlGaAs barriers with the Al concentration fixed to 48.1%. The highest $\chi^{(2)}$ value in most cases is obtained for triple QW structures, so only these are used in further discussion of SPDC entangled photon generation.

Resonantly enhanced nonlinearities are always accompanied with increased absorption, which has to be taken into account when considering the efficiency of optical processes. The absorption coefficient α, is found from the imaginary part of the linear susceptibility ($\chi^{(1)"}$) [64, p. 167], and is calculated from:

$$\alpha = \chi^{(1)"}\omega/c \ , \tag{5.11}$$

with ω is the photon angular frequency, c is the speed of light and $\chi^{(1)"}$ is,

$$\chi^{(1)"} = \sum_n \frac{N f_{ij} e^2}{2\varepsilon_0 m \omega_{ij}} \left[\frac{\Gamma_{ij}}{\Gamma_{ij}^2 + (\omega_{ij} - \omega)^2} - \frac{\Gamma_{ij}}{\Gamma_{ij}^2 + (\omega + \omega_{ij})^2} \right] \ . \tag{5.12}$$

Equation (5.12) depends on the number of electrons (N),relaxation rates(Γ_{ij}) and the oscillator strength of i to j transitions withf_{ij} defined as

$$f_{ij} = \frac{2m\omega_{ij}|d_{ij}|^2}{3\hbar e^2} \ . \tag{5.13}$$

Inserting Equation (5.13) into Equation (5.12), the imaginary part of linear susceptibility ($\chi^{(1)"}$) can be written as

$$\chi^{(1)"} = \sum_n \frac{e^2 N d_{ij}^2}{3\hbar\varepsilon_0} \left[\frac{\Gamma_{ij}}{\Gamma_{ij}^2 + (\omega_{ij} - \omega)^2} - \frac{\Gamma_{ij}}{\Gamma_{ij}^2 + (\omega + \omega_{ij})^2} \right] \ . \tag{5.14}$$

Using Equation (5.11) and (5.14) and by making use of the best structure that we get for SPDC process in Table 5.1, we plot the absorption coefficient in the Figure 5.3.

From Figure 5.3, there are two peaks that mean most absorption occurred at these two photon energies. The maximum absorption occurred at photon energy which is almost equal to signal or idler photon and the second largest absorption occurred at energy equal to that of the pump photon.

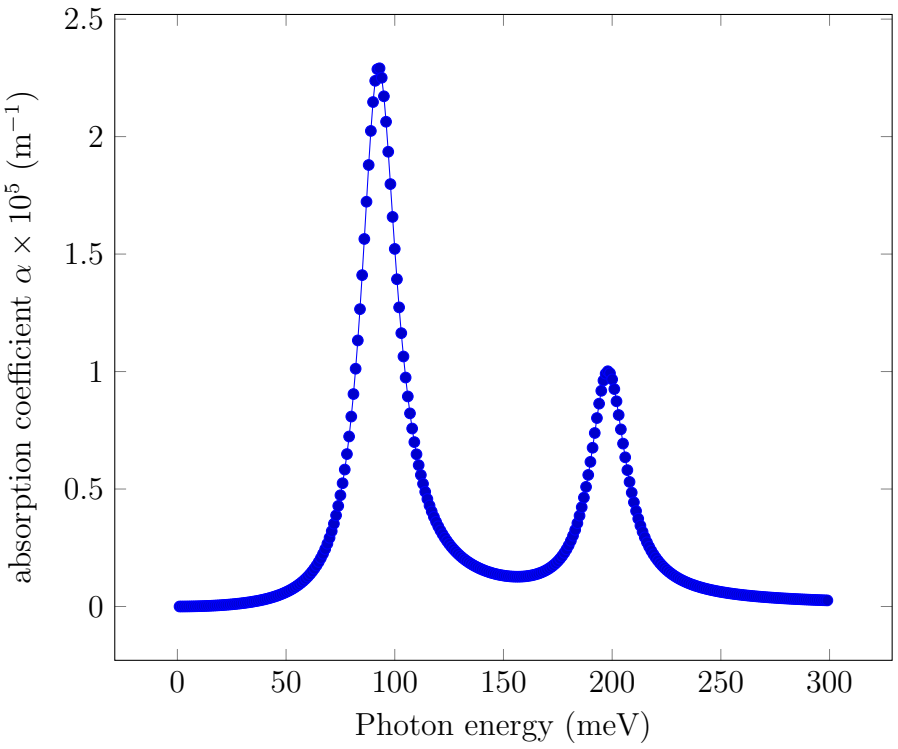

Figure 5.3: Absorption coefficient

5.4 Twin Photon Generation

The quantitative analysis of twin-photon generation in media which have optical losses have been presented in [69]. For non-degenerate twin-photon generation, the expression for the correlated twin (ω_1, ω_2) photon flow, P_{Twin} is [69]:

$$P_{\text{Twin}} = \frac{c|\kappa|^2 P_3 L}{|n_1 - n_2|} \frac{e^{-2\alpha_3 L} - e^{-2(\alpha_1+\alpha_2)L}}{2(\alpha_1 + \alpha_2 - \alpha_3)L} \ . \tag{5.15}$$

and in the degenerate case, where the signal and idler frequencies are (almost) the same, the corresponding expression is [69]:

$$\begin{aligned} P_{\text{Twin}} =& \frac{4|\kappa|^2 P_3 L^{3/2}}{3\sqrt{2\pi|g|}} \frac{3e^{-|\alpha_{11-3}|L}}{2|\alpha_{11-3}L|^{3/2}} \\ & \times \int_0^{\sqrt{|\alpha_{11-3}L|}} \sinh(|\alpha_{11-3}L| - x^2)\ dx \ . \end{aligned} \tag{5.16}$$

where $\alpha_{11-3} = \alpha_1 + \alpha_2 - \alpha_3$ (the absorption difference) and $g = [\partial^2\beta/\partial\omega^2]$, with $\beta = 2\pi n_{p/2}/\lambda_{p/2}$.

The n_i and α_i in Equation (5.15) and (5.16) are the refractive index and absorption coefficient at photon frequency ω_i, L is the length of the device, P_3 is the pump power, and κ is related to $\chi^{(2)}$ via

$$|\kappa|^2 P_3 = \sqrt{\frac{4\omega_1^2\omega_2^2 d_{\text{eff}}^2 |A_3|^2}{k_1 k_2 c^4}} \ . \tag{5.17}$$

where $d_{\text{eff}} = 0.5\chi^{(2)}$, and k_i is the wavenumber for photon i. A_3 is related to the intensity of the pump (a value of I_3=1 kW/cm^2 was used in calculations), with $A_3 = \sqrt{2I_3/(\varepsilon_0 c n_3)}$. The refractive indices n_i in Equation (5.15) depend on the photon wavelengths. These are calculated using Sellmeyer's equation for GaAs and AlGaAs [70], using the weighted average of the refractive indices for the constituent binary compounds in the structure (this is justified because the wavelengths involved are far larger than any layer thickness in the structure). The refractive index also depends on the temperature of the heterostructure [71], and in these calculations room temperature was assumed.

The structures were designed / optimised for the largest $\chi^{(2)}$ at the specified values of ω_s and ω_i, but from (5.15) or (5.16) it is clear that the actual twin photon generation rate also depends on the structure length, and on the absorption at all the involved frequencies, and the transition linewidth will thus also indirectly influence the conversion efficiency. All this implies that the best performance may not even be necessarily obtained "at resonance". The optimal (in $\chi^{(2)}$ alone) structure profile itself is not affected by the choice of linewidth (we have checked that, and only the actual value of $\chi^{(2)}$ at resonance is affected). An alternative approach to the structure design would be to optimise for efficiency, considering the linewidth, interaction length and signal / idler frequencies as additional optimisation parameters. However, to reduce the number of parameters, in this work we have used the optimisation of $\chi^{(2)}$, and have subsequently varied the signal / idler frequencies, linewidth, and the interaction length in order to find the best performance achievable under realistic conditions.

5.4.1 Non-degenerate case

Fig. 5.4 and 5.5 show the pump to twin-photon conversion efficiency for non-degenerate cases, using two different optimized structures (designed to split pump photons into two photons with the ratio of their frequencies either 2:1 or 3:1). The actual values of pump or signal photon energies were then varied around the design values, and the transition linewidth was also varied, and in each case the length which produces the largest conversion rate is found and recorded. This (optimal) conversion length should be well below the coherence length of the nonlinear process, otherwise a serious reduction of "effective" $\chi^{(2)}$ would take place (or some reduction if quasi-phase-matching is employed). For the pump frequency and splitting ratios considered here, using the Sellmeyer's equation again gives the coherence lengths of ∼1000–1500 μm, and the conversion length was required to be below 100 μm, but the actual values found in non-degenerate cases were much smaller than that. The results in Fig. 5.4 show that a larger linewidth requires a larger interaction length for the maximum efficiency, and even then this efficiency is smaller than for narrow linewidths. Furthermore, as shown in Fig. 5.5, for realistic values of the linewidth (mid-range in Fig. 5.4) a structure may not perform best under the exact resonance conditions for which it is designed, i.e. some detuning from it may actually improve the conversion, on account of the reduced absorption, despite the simultaneous decrease of the $\chi^{(2)}$ value.

5.4.2 Degenerate Case

Fig. 5.6 shows the nearly-degenerate twin-photon conversion efficiency, Equation (5.16), as it depends on the signal/idler frequency in the SPDC99 structure, calculated for a couple of different linewidths. The optimal interaction length, required for this conversion, is shown in Fig. 5.6(b), but is limited to 100μm, both in order to keep phase-mismatching negligible and to have a very short SPDC converter. Fig. 5.6(c) shows the frequency dependence of $\chi^{(2)}$ of this structure for different linewidths, this is clearly very different from the conversion efficiency, due to the influence of absorption.

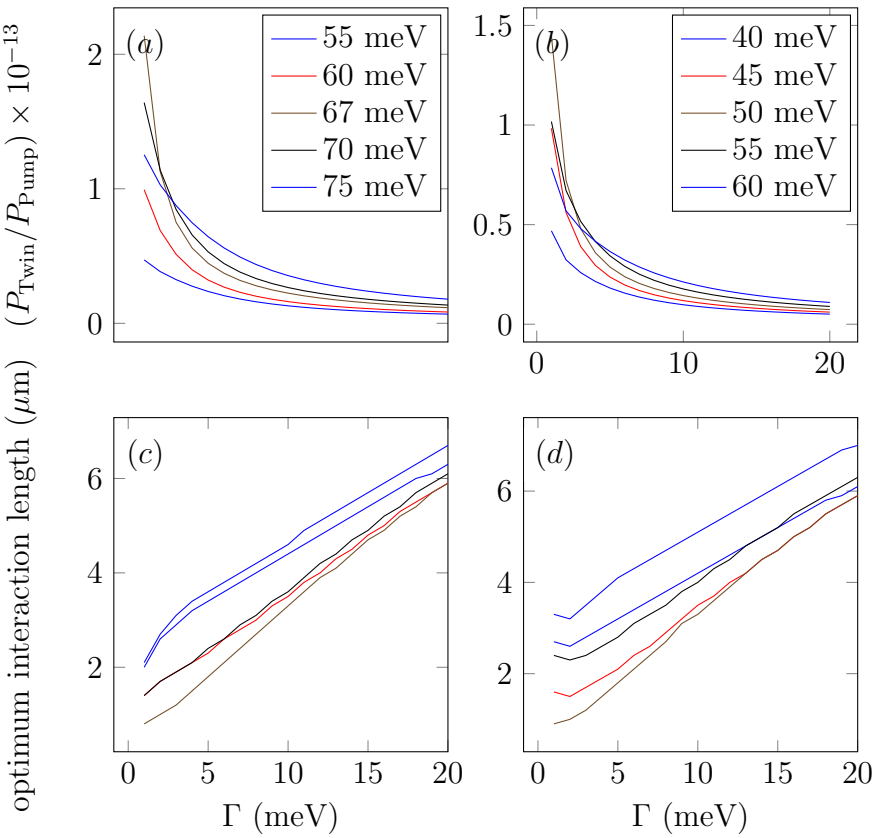

Figure 5.4: The pump to twin-photon conversion efficiency calculated for the optimised non-degenerate case structures for different idler's energy (coloured lines). The left plots (a,c) is for the case where the structure is optimised for idler = 1/3 × pump (67 meV), and the right plot (b,d) for the structure optimised for idler = 1/4 × pump (50 meV).

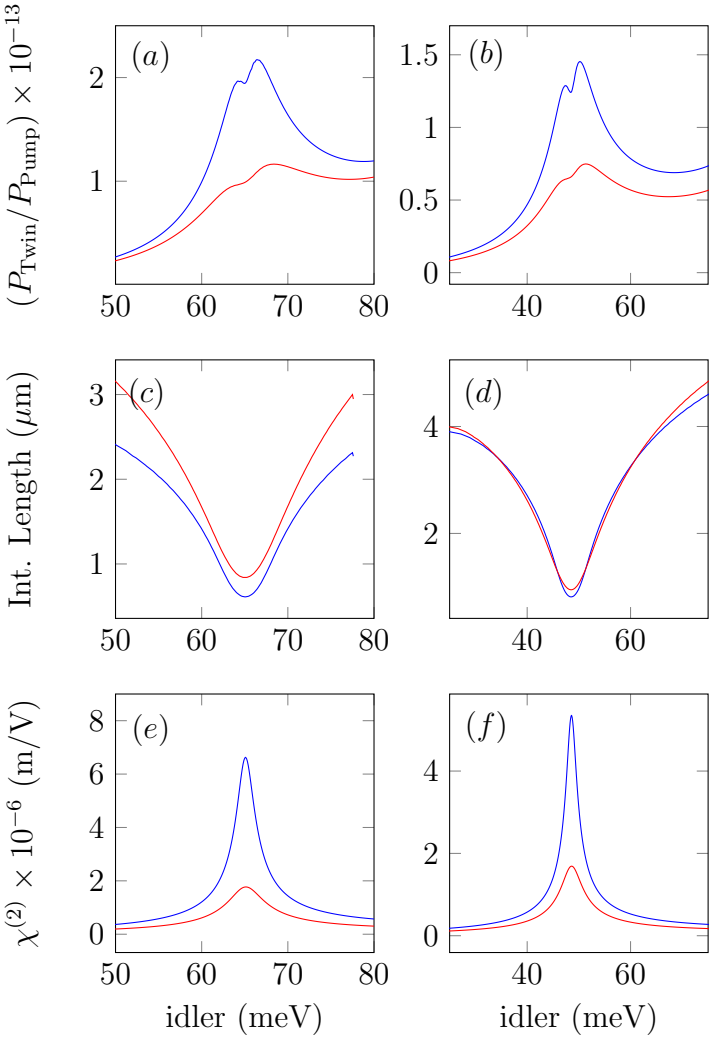

Figure 5.5: The pump to twin-photon conversion efficiency calculated for the optimised non-degenerate case structures, with the linewidth of 1 meV (blue line) and 2 meV (red line). The left plots (a,c,e) use the best structure for case of the idler being 1/3 of the pump energy (67 meV) and the right plots (b,d,f) are for the case of the idler being 1/4 of the pump energy (50 meV).

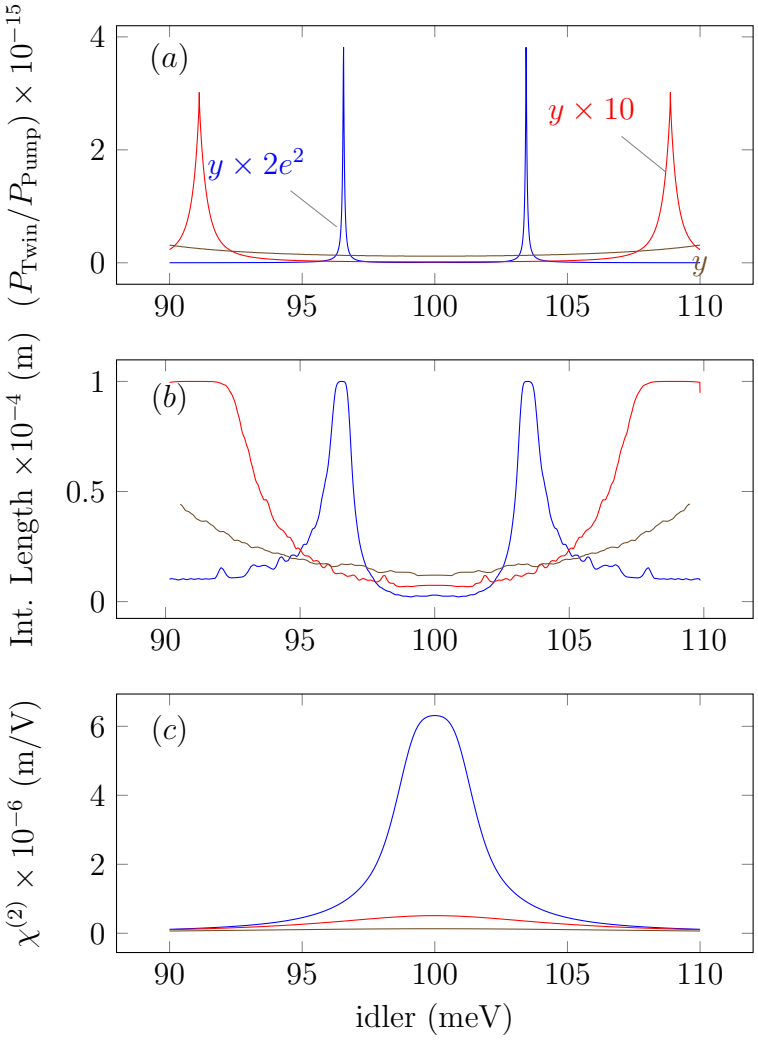

Figure 5.6: (a) The pump to almost-degenerate twin-photon generation efficiency of the SPDC99 structure, calculated for different linewidths, 1 meV (blue), 5 meV (red), and 10 meV (brown line); (b) the optimal interaction length, necessary for the efficiency shown in (a), and (c) $\chi^{(2)}$ in the optimised structure, for different linewidths.

5.5 Schmidt Number

The SPDC-generated twin-photon state can be written as [72],

$$|\Psi\rangle = A \iint dv_+ dv_- \alpha(v_+)\phi(v_-)\, |2^{-1/2}(v_+ + v_-)\rangle_s\, |2^{-1/2}(v_+ - v_-)\rangle_i \ , \quad (5.18)$$

where A is the normalization constant, and $|...\rangle_\mu$ (with $\mu = s, i$) represent the single photon Fock states in signal and idler modes. $\alpha(v_+)\phi(v_-)$ in Equation (5.18) is the joint amplitude of pump envelope function (PEF) $\alpha(v_+)$ and 'phase-matching function' (PMF) $\phi(v_-)$, where in SPDC processes in bulk nonlinear materials the latter comes from the phase mismatch of the three waves and the presence of any quasi-phase-matching (QPM) scheme applied. In the QW structures considered here the conversion lengths are very short for any significant phase mismatch to appear, but the nonlinearity is strongly resonant, i.e. dispersive.

The amount of quantum entanglement (including polarization, spatial and spectral degree of freedom) between two-photon states generated in SPDC process can be quantified by the cooperativity parameter known as Schmidt Number K. The minimum allowed value of K is 1, which corresponds to no entanglement. Based on Equation (5.18), if $\alpha(v_+)$ and $\phi(v_-)$ can be approximated as Gaussian functions, with the full width at half maximum (FWHM) of σ_+ (for the pump power) and σ_- (for the twin-photon power) respectively, and if $\sigma_+ \ll \sigma_-$, the K value can be obtained from a simple analytical expression in Equation (5.19) [72]:

$$K = \frac{1}{2^{1/2}} \frac{\sigma_-}{\sigma_+} \ . \quad (5.19)$$

The pump at these, mid-IR wavelengths is likely to be a quantum cascade laser, and typical bandwidths then are in the 550 kHz to 1.5 MHz range, e.g. [73]. By varying the signal and idler frequencies we find that $\phi(v_-)$ indeed has an approximately Gaussian shape, and its K value is given Table 5.2 (using a PEF bandwith of 1 MHz, i.e. $\sigma_+ = 4.239 \times 10^{-6}$ meV), which would imply a good degree of twin-photon entanglement, although not as high as predicted for SPDC process in transparent nonlinear bulk materials [72].

Table 5.2: Schmidt number for different structures and different linewidths (Γ). Empty fields correspond to cases where the simple expression in Equation (5.19) could not be used.

Γ (meV)	OPT67	OPT50	OPT99
1	7411	5901	8248
2	7716	5962	
5			12317
10			

5.6 Conclusion

Optimization of QW structures to deliver large second-order nonlinear susceptibility $\chi^{(2)}$, useful for the frequency-entangled twin-photon generation by SPDC,was performed using a genetic algorithm. Calculations show that, for structures operating in the mid-infrared range, a reasonably good degree of entanglement can be obtained, and the required optimal conversion length is very short. Furthermore, the structures which have a large spacing between the lower two subbands are advantageous over structures where this spacing is small.

Chapter 6

SPDC by Intersubband transitions in the Valence Band

This chapter is based on the published reference [74] : "Polarization-entangled mid-infrared photon generation in p-doped semiconductor quantum wells" [R. Razali, Z. Ikonić, D. Indjin and P. Harrison *Semicond. Sci. Technol.* **31** (2016) 115011]

6.1 Introduction

Quantum correlated photon pairs, also known as entangled photon pairs, are the main ingredient in quantum communications [75], quantum computing [75, 76, 77], quantum key distribution (QKD) [78], quantum teleportation [79], super-dense coding [80] and many other applications of quantum information theory. These photon pairs can be generated in SPDC, or in SFWM [81]. SPDC, which is also known as parametric fluorescence [19], is based on second order nonlinearity ($\chi^{(2)}$), while SFWM is based on third order nonlinearity ($\chi^{(3)}$). Raman scattering noise, which is hard to suppress in SFWM [82], has made the SPDC scheme more attractive. The SPDC and SWFM processes, producing entangled photon pairs, can be induced in different media, like bulk crystals (possibly with tailored inhomogeneous nonlinearity [31]), QW heterostructures, in quantum dots [35, 83], or NV centres in diamond [84].

This work focuses on SPDC process based on intersubband transitions in the VB of QW heterostructures. The incentive to consider this case comes from the fact that SPDC based on intersubband transitions within the CB Γ-valley (the most frequent case) does not provide polarization entanglement, since these transitions are active only for Z-polarization of light (perpendicular to the well layer)[67]. In contrast, VB intersubband transitions are active for various polarizations, which comes from their p-like, rather than s-like character, enabling polarization entanglement in the SPDC process (in particular, the type II SPDC). Unlike the case of CB intersubband transitions, the optical parameters of VB intersubband transitions cannot be calculated by the EMA, but rather by $\mathbf{k}\cdot\mathbf{p}$ method (in particular, for structures based on wider band gap materials, assumed in this work, the 6-band $\mathbf{k}\cdot\mathbf{p}$ method is sufficiently accurate). As for the structure design and optimisation, the methodology employed here is similar to what we have used previously [67]

As pointed in [85], which considered the optimization of the second harmonic generation (SHG) in p-type GaAs-AlAs step QW structures, the symmetry of hole state wave functions enables only 5 non-zero components of the second-order polarizability: ZXY, ZXX, XYZ, XXZ and ZZZ, where the first component denotes the generated SHG photon polarization, the other two being the pump photons. SPDC is similar to SHG, but reversed in time, so these selection rules apply to SPDC as well. Therefore, generation of polarization-entangled twin photons can rely on ZXY, XYZ or XXZ configuration. Practical considerations, suggesting that SPDC will be used in waveguide layout (co-propagating waves), imply that polarizations of the three waves cannot be all different, hence only the XXZ polarization will be considered here.

As mentioned in Chapter 5, the maximally entangled Bell-states take form as Equation 5.1 and 5.2. For this Chapter $|0\rangle = |\omega, Z\rangle$, $|1\rangle = |\omega, X\rangle$ with $\omega = \frac{1}{2}\omega_{pump}$

6.2 SPDC based on valence intersubband transitions

SPDC is a second order optical process, with the nonlinear polarization

$$\mathbf{P} = \varepsilon_0 \chi^{(2)} \mathbf{E}^2 \tag{6.1}$$

determined by the second-order nonlinear susceptibility $\chi^{(2)}$ as given e.g. in [64, p. 174]. For intersubband transitions involving hole states in QWs the state energies $E_l(k_x, k_y)$ depend on their quantum index l and the in-plane wave vector (k_x, k_y), and the transition matrix elements also depend on (k_x, k_y), so the summation over all states, discretized in the (k_x, k_y) plane, is written as

$$\begin{aligned}
\chi^{(2)}\left(\omega_p + \omega_q, \omega_p, \omega_q\right) = \frac{e^3 \Delta k_x \Delta k_y}{8\pi^2 L_z \varepsilon_0 \hbar^2} \times \\
\sum_{k_x,k_y} \sum_{lmn} \left[f_{\mathrm{FD}}(E_l(k_x,k_y), E_F) - f_{\mathrm{FD}}(E_m(k_x,k_y), E_F)\right] \\
\left\{ \frac{d^x_{ln} d^x_{nm} d^z_{ml}}{\left[(\omega_{nl} - \omega_p - \omega_q) - i\Gamma_{nl}\right]\left[(\omega_{ml} - \omega_p) - i\Gamma_{ml}\right]} \right. \\
+ \frac{d^x_{ln} d^z_{nm} d^x_{ml}}{\left[(\omega_{nl} - \omega_p - \omega_q) - i\Gamma_{nl}\right]\left[(\omega_{ml} - \omega_q) - i\Gamma_{ml}\right]} \\
+ \frac{d^x_{ln} d^x_{nm} d^z_{ml}}{\left[(\omega_{nm} + \omega_p + \omega_q) + i\Gamma_{nm}\right]\left[(\omega_{ml} - \omega_p) - i\Gamma_{ml}\right]} \\
\left. + \frac{d^z_{ln} d^x_{nm} d^x_{ml}}{\left[(\omega_{nm} + \omega_p + \omega_q) + i\Gamma_{nm}\right]\left[(\omega_{ml} - \omega_q) - i\Gamma_{ml}\right]} \right\},
\end{aligned} \tag{6.2}$$

where e is the electron charge, Δk_x and Δk_y are the mesh steps in x- and y-directions, L_z is the total length of the structure in z-direction, ε_0 is the free space permittivity, ω_p, ω_q and $\omega_p + \omega_q$ are the frequencies of three photons interacting in the nonlinear system, and $\hbar\omega_{nm} = E_n(k_x, k_y) - E_m(k_x, k_y)$ is the subband spacing at a particular (k_x, k_y). In the SPDC case, ω_p and ω_q may denote the signal and idler photons, while $\omega_p + \omega_q$ is the pump photon that will be down-converted in the SPDC process. Γ_{ij} is the linewidth of $i \to j$ transition, and d^x_{ij} is the x-component of dipole matrix element for this transition. The state energies $E_m(k_x, k_y)$ and the matrix elements d^x_{ij} were calculated using 6×6 k.p method

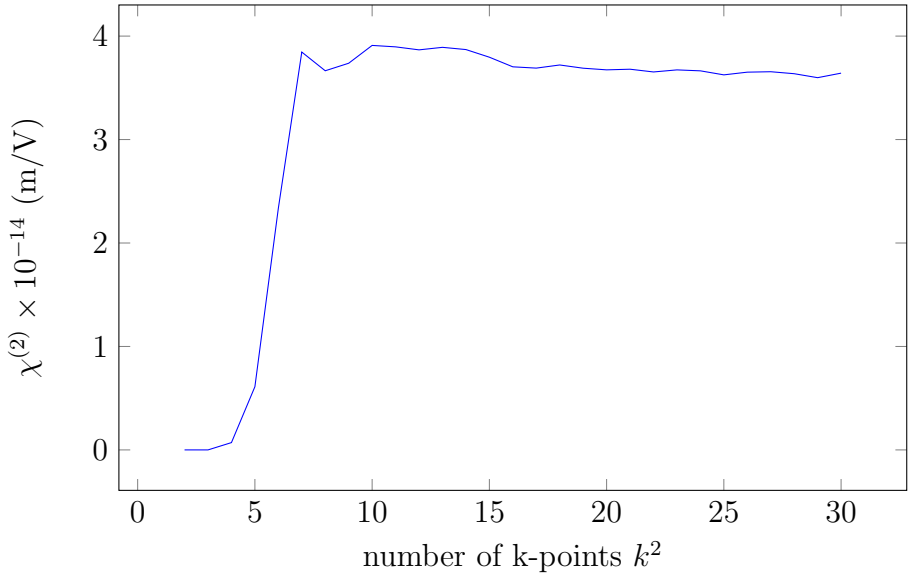

Figure 6.1: Convergence of $\chi^{(2)}$ with variable total number of k-points

[59, p. 407].

The state populations in (6.2) are given by the Fermi-Dirac function f_{FD}:

$$f_{\text{FD}}(E_a(k_x, k_y), E_F) = \left[1 + e^{\left(\frac{E_a(kx,ky) - E_F}{k_B T}\right)}\right]^{-1} . \tag{6.3}$$

where E_F is the Fermi energy in the structure, k_B is the Boltzmann's constant and T is the temperature.

6.3 Convergence of Results

In calculating the $\chi^{(2)}$ value for each structure, the number of k-points that was considered in each calculation will affects the precision of $\chi^{(2)}$ value that we can get. Of course by increasing the number of k-points, we can get really precise value but it will increase the computational time to get the results. So here we plot the number of k-points taken in a calculation for one structure against the $\chi^{(2)}$ value to look at how many points of k is good enough to be used for further optimization, so that we won't overuse the computational time to get acceptable value.

From Figure 6.1, we can see that the convergence of $\chi^{(2)}$ starts when number of k-points is square of 15. So we can stop at 225 k-points at quarter plane area to get acceptable value of $\chi^{(2)}$. Since using quarter plane is good enough to represent the whole plane, if we consider full plane we would effectively use 900 k-points to get these results. So, by using 225 points in quarter plane saves three quarters of computational time for the same accuracy of $\chi^{(2)}$.

6.4 Degenerate Twin Photon Generation

Quantitative analysis of twin-photon generation in the presence of optical losses [69] shows that the degenerate twin photon generation is given by

$$P_{\text{Twin}} = \frac{4|\kappa|^2 P_3 L^{3/2}}{3\sqrt{2\pi|g|}} \frac{3e^{-|\alpha_{123}|L}}{2|\alpha_{12-3}L|^{3/2}} \times \int_0^{\sqrt{|\alpha_{12-3}L|}} \sinh(|\alpha_{12-3}L| - x^2)\, dx \ . \tag{6.4}$$

where $\alpha_{123} = \alpha_1+\alpha_2+\alpha_3$, $\alpha_{12-3} = \alpha_1+\alpha_2-\alpha_3$, $g = [\partial^2\beta/\partial\omega^2]$, and $\beta = 2\pi n_1/\lambda_1$. The α_i in (6.4) is the absorption coefficient at photon frequency ω_i for $i = 1, 2, 3$, L is the length of the device, P_3 is the pump power, and κ is related to $\chi^{(2)}$ via

$$\kappa = \varepsilon_0 d_{\text{eff}} \sqrt{\frac{2\omega_1\omega_2}{n_1 n_2 n_3 S_{\text{eff}}} \left(\frac{\mu_0}{\varepsilon_0}\right)^{\frac{3}{2}}} \tag{6.5}$$

where $d_{\text{eff}} = 0.5\chi^{(2)}$, S_{eff} is the pump beam cross section. It should be noted that the three waves (1,2,3) each have generally different absorption coefficients α_i, either because of their frequency (pump vs. signal/idler) or because of their polarization (signal vs. idler, which are degenerate in frequency, but not in polarization). The n_i in Eqs.(6.4) and (6.5) is the refractive index at frequency ω_i, calculated from Sellmeyer's equation for GaAs and AlGaAs [70], including the temperature dependence [71], and then using the weighted average of the refractive indices for the constituent binaries in the structure (this is justified because the wavelengths involved are far larger than any layer thickness in the structure).

The absorption coefficient α in (6.4) is calculated from the imaginary part of

linear susceptibility ($\chi^{(1)}$), as [64, p. 167]

$$\alpha = \chi^{(1)\prime\prime}\omega/c \ , \tag{6.6}$$

where $\chi^{(1)\prime\prime}$ is calculated as

$$\begin{aligned}\chi^{(1)\prime\prime} = \ & \frac{\Delta k_x \Delta k_y}{(2\pi)^2 L_z} \frac{e^2}{3\hbar\varepsilon_0} \sum_{k_x,k_y} \sum_n \{f_{\mathrm{FD}}(E_l(k_x,k_y),E_F) - \\ & f_{\mathrm{FD}}(E_m(k_x,k_y),E_F)\} \, |d^i_{lm}|^2 \times \\ & \left[\frac{\Gamma_{lm}}{\Gamma^2_{lm}+(\omega_{lm}-\omega)^2} - \frac{\Gamma_{lm}}{\Gamma^2_{lm}+(\omega+\omega_{lm})^2}\right] .\end{aligned} \tag{6.7}$$

For resonant structures the absorption peaks at pump and signal / idler photon energies, just as the nonlinear susceptibility does, and must be accounted for.

As illustrated in Figs. 6.2(a) and 6.2(b), the product of dipole matrix elements depends on (k_x, k_y), but the pattern is replicated in each quarter of the k_x–k_y plane, which is used in summation over k_x, k_y points in Eq.(6.2) to speed up the calculations by a factor of 4, which is important for the optimisation process.

In calculating $\chi^{(2)}$ the summation should include all k-points which may have any significant population of holes, and with the in-plane dispersion of hole state varying from one structure to another: 10% of the Brillouin zone was taken as a safe limit. The number of k-points within this range is taken as 15 in each direction, which gives a reasonable convergence of the calculated value of $\chi^{(2)}$. In numerical calculations the pump power $P_3 = 1$ kW, and cross section $S_{\mathrm{eff}} = 100 \times 100 \ \mu m^2$ were used for reference.

Fig. 6.2 shows an example of the variation of the $\{\ldots\}$ term in (6.2) (product of matrix elements and resonance terms in denominators, but without the hole density-dependent Fermi-Dirac terms), as it varies across the (k_x, k_y) plane.

6.5 Optimization of SPDC efficiency

QW structures suitable for SPDC were designed by performing a genetic optimization, with SPDC efficiency as the target. We consider the degenerate SPDC, with signal and idler photon energies fixed to 100 meV and the pump to 200 meV, while the linewidth Γ was assumed to have the 'typical' value of 10 meV for

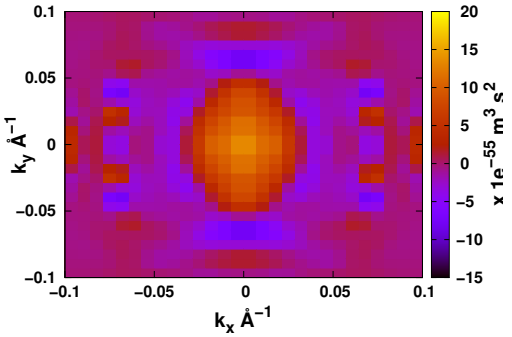

(a) Real part

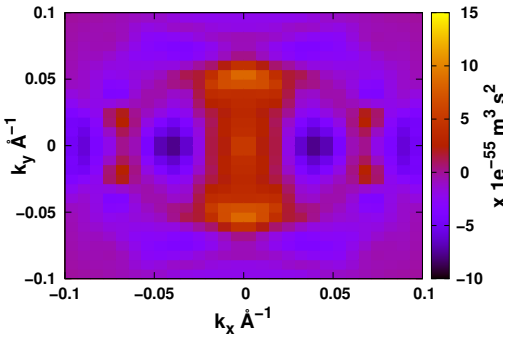

(b) Imaginary part

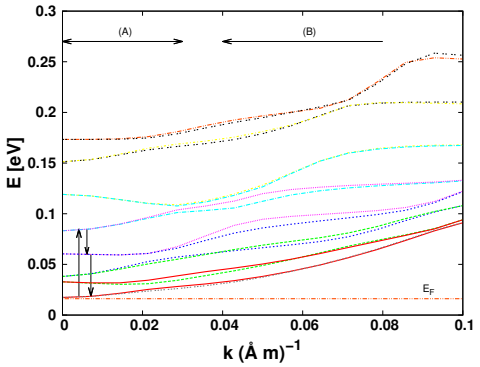

(c) The dispersion of quantised states

Figure 6.2: (a,b) The value of the $\{\ldots\}$ term in Eq.(6.2), calculated for the first structure from Table 6.1, as it depends on (k_x, k_y) and (c) The dispersion of quantised states in this structure, with the transition which, although off-resonant, gives the largest contribution to $\chi^{(2)}$ denoted (however, various other transitions also contribute significantly). The small (A) and large (B) wave vector ranges give opposite-in-sign contributions to $\chi^{(2)}$).

all transitions. Non-zero $\chi^{(2)}$ requires asymmetric QWs, and the simplest structures of this type are double QWs (DQW) and step QWs. The DQW structure with equally deep wells was chosen, because it can be more easily fabricated with good accuracy. Even for the technologically well developed AlGaAs system, the variable-width rectangular profiled structures (with just two different material compositions) can presently be grown with better accuracy than the variable-composition structures (even the simplest among them, the stepped QWs). They are the only type of heterostructures practically used nowdays for intersubband devices, e.g. in complex devices like quantum cascade lasers, despite the fact that an even better performance could sometimes idealistically be expected from carefully tailored variable-composition structures. The parameters to be varied are the widths of the two wells and the barrier, and the well depth is taken constant, determined by the material composition. The holes density is kept low (3.2×10^6 cm^{-2}) so that space charge potential could be neglected. The method of optimization is similar to that described in Section 5.3 and Appendix E, the only difference being that we have chosen here the SPDC efficiency, rather than the value of $\chi^{(2)}$, as the target, so the effects of pump and signal/idler absorption are included.

The material system considered in this work is the technologically most developed AlGaAs alloy, with GaAs taken as the well and AlGaAs as the barrier material, with the Al content in the alloy equal to 48%. In Table 6.1, the structural unit is AlGaAs/GaAs/AlGaAs/GaAs/AlGaAs DQW, with the first and last layers being thick AlGaAs barriers, their thickness being somewhat arbitrarily set to 100 Angstrom ($\mathring{A}$) to make neighbouring DQWs independent, i.e. well isolated from each other. The widths of the three inner layers, coming from the optimisation procedure, are also given in Table 6.1 in $\mathring{A}$ units.

Table 7.1 shows a number of best daughter structures, coming from different parents, retained before selecting the best one at the end of the optimisation procedure. This illustrates a limited correlation between nonlinear susceptibility and conversion efficiency, and in particular the fact that the highest value of $\chi^{(2)}$ does not imply that this structure will deliver the highest efficiency. The reason behind this is the absorption, as will be discussed in more detail in Sec. 6.6.

Table 6.1: The partially or fully optimized DQW structures, their SPDC efficiency, and the value of $\chi^{(2)}$, respectively.

structure	**SPDC efficiency**	$\chi^{(2)}$ **(m/V)**
100/34/5/76/100	2.11×10^{-21}	1.09×10^{-13}
100/36/12/62/100	1.31×10^{-21}	1.22×10^{-12}
100/82/5/24/100	3.88×10^{-22}	9.87×10^{-14}
100/13/18/54/100	3.18×10^{-22}	5.46×10^{-14}
100/40/9/68/100	3.03×10^{-22}	1.81×10^{-13}
100/68/9/40/100	2.64×10^{-22}	1.67×10^{-13}
100/11/58/49/100	1.11×10^{-22}	2.72×10^{-14}
100/55/29/81/100	2.77×10^{-22}	5.24×10^{-14}

6.6 Effect of Holes Density on the SPDC Efficiency

In this section we consider the effect of the hole density, while keeping the interaction length limited to 100μm, on the SPDC efficiency. The holes density was varied from 5×10^{6} to 2×10^{12} cm^{-2}, and the best (fully optimised) structure from Table 7.1 was used. As shown in Fig. 6.3(a), there exists an optimum density, for which the SPDC efficiency is largest. The reason behind this is that, as shown in Fig. 6.2, there are areas in the (k_x, k_y) plane where the relevant combination of dipole matrix elements has very high values. At low temperatures (T=77K) holes populate almost fully all the (k_x, k_y) states below the Fermi level, and states above it are almost empty. Increasing the hole density increases the Fermi level, and expands the range of (k_x, k_y) states which are populated. The value of $\chi^{(2)}$ then increases, because all the small (k_x, k_y) states have significant (and same sign) contributions to $\chi^{(2)}$, as shown in Fig. 6.2. However, adding even more holes does not necessarily mean that $\chi^{(2)}$ will steadily increase. There is an area in the (k_x, k_y) plane where the $\{\ldots\}$ term in Eq.(6.2) changes sign, (Figs. 6.2(a),(b) and (c)) , and if this becomes populated with holes, the value of $\chi^{(2)}$ will actually decrease, as displayed in Fig. 6.3(b) (point after the optimum holes density). In addition, more holes will also increase the absorption (which only gets positive contributions from any (k_x, k_y)), as can be seen from Figs. 6.3(c)-(e), hence decreasing the SPDC efficiency. Therefore, choosing the correct value of holes

density is important for achieving the highest SPDC efficiency, Fig. 6.3(a).

As shown in Fig. 6.3(c), the optimum interaction length L is always small for reasonably large values of hole density, across the temperature range of practical interest. Noteworthy, the coherence length l_c for this degenerate SPDC case is 1500 μm, as calculated from Sellmeyer's equation [70], and this value is applicable to large cross-section ('bulk-like') MQW structures. For L comparable to l_c the effective $\chi^{(2)}$ would decrease, and would even become very small if $L >> l_c$. However, employing quasi-phase-matching schemes would enable just a moderate reduction of l_c (by a factor of $2/\pi$) [86]. Alternatively, dispersion engineering (e.g. by dispersion engineering of the waveguide structure, to give the same velocity of pump and signal waves) would increase l_c itself. To avoid going into details on this side, we have used Eq.(6.4) in calculations, having in mind that some further reduction of efficiency might take place in real structures if the interaction length is large.

6.7 Effect of Pump Frequency Variation on the SPDC Efficiency

It is interesting to explore how 'broadband' a particular structure can be considered to be, so we next consider the effects of variation of the pump frequency around the value a particular structure is designed / optimised for (200 meV), on the SPDC efficiency. We take the optimum structure (100/34/5/76/100), at 77K and 300K, and choose the optimal values of hole densities and interaction lengths (extracted from Fig. 6.3(c), and given in Table 6.2), which deliver the peak efficiency at the design pump frequency, Fig. 6.3(a). The SPDC efficiency is then calculated for a range of pump photon energies, from 160 to 240 meV (while the signal and idler photon energies are always kept to a half of that value). The results are shown in Fig. 6.4.

As shown in Figs. 6.4(a), the structure optimised for 200 meV pump, with a low value of hole density, gives at 77K the highest efficiency for the pump energy at 205 meV (with the signal/idler at 102.5 meV), while at 300K its efficiency is highest for 210 meV pump (with signal/idler at 110 meV). However, these peak ef-

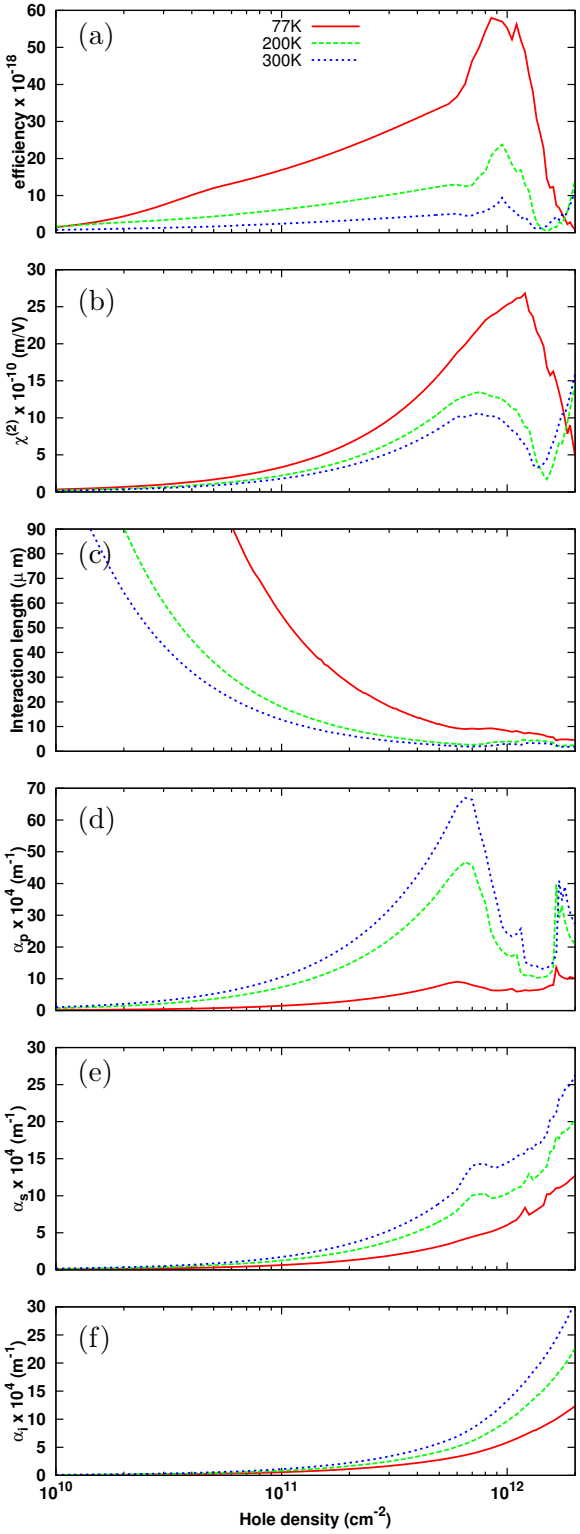

Figure 6.3: The hole density dependence of relevant parameters in the fully optimised structure at different temperatures: (a) twin photon generation efficiency, (b) $\chi^{(2)}$, (c) optimal interaction length, (d)-(e) the absorption coefficient for the pump, signal and idler wave (note that the signal and idler have the same frequency but different polarization). The solid red line in Fig. 6.3(a) is scaled down by 0.2, so that all lines are clearly visible

.

Table 6.2: The optimal values of hole density and interaction length for the structure (100/34/5/76/100), at different temperatures.

T (K)	**Optim. hole density (cm^{-2})**	**L (μm)**
77	8.5×10^{11}	9.3
200	9.5×10^{11}	3.8
300	1.0×10^{12}	2.9

ficiencies are only slightly higher than for 200 meV pump. In fact, in this optimal structure neither the nonlinear susceptibility nor the absorption have any prominent resonant features, Figs. 6.4(b)-(e). Although $\chi^{(2)}$ decreases with increasing pump energy, the efficiency is still somewhat better in the higher energy range (200-240 meV) than in the lower energy range (160-200 meV), Fig. 6.4(a), because the absorption behaves in the opposite manner, and the resulting efficiency comes from the interplay of the two. Generally, the structure has a rather large useful bandwidth for SPDC, of ~ 40 meV, before its efficiency drops to a half of its peak value. This feature makes these devices perspective for communication systems.

It is interesting to note that the values of the conversion efficiency, Fig. 6.3, depend quite strongly on temperature, but the position of the peak (and also its width) depend rather weakly on temperature. This comes from the fact that the general shape (frequency dependence) of nonlinear susceptibility and absorption coefficients of the three waves, Figs. 6.3(b-e), does not change much with temperature, and the conversion efficiency, which depends on all these effects, inherits the temperature insensitivity of its frequency dependence (however the actual values of efficiency, on or off peak, are affected).

6.8 Conclusion

Optimization of p-doped QW structures to deliver efficient polarization-entangled twin-photon generation by SPDC in the mid-infrared spectral range was performed using a genetic algorithm. Calculations show that the optimal structure lengths are rather small, with practically accessible levels of hole densities, and have a reasonably large bandwidth, which makes them practically interesting.

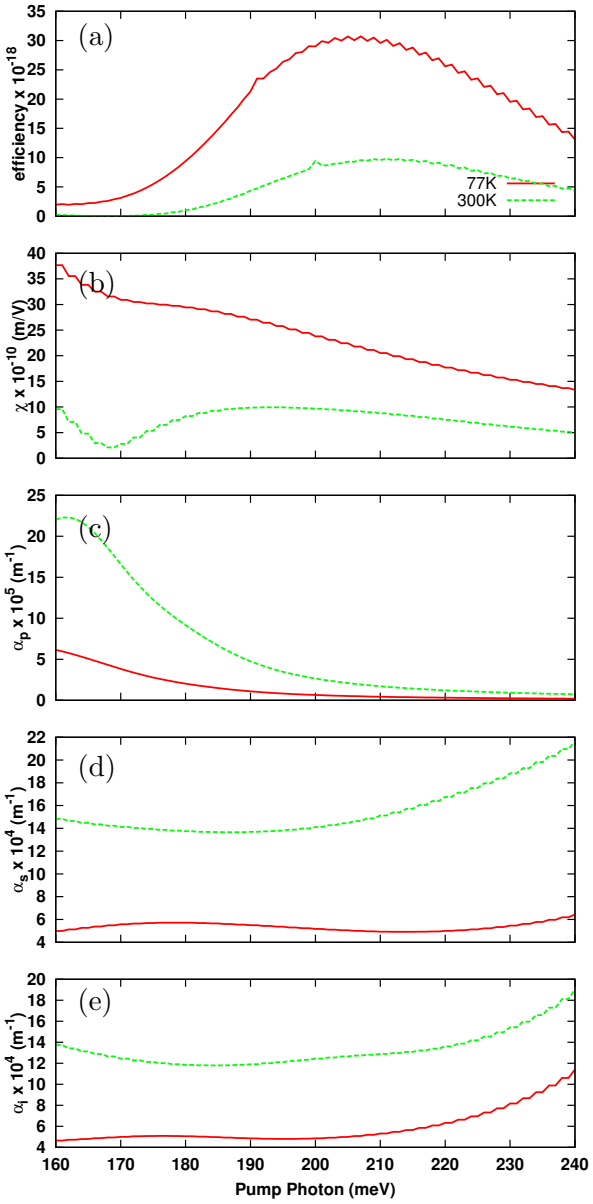

Figure 6.4: Twin-photon generation efficiency (a), as well as $\chi^{(2)}$ and absorption α (b)-(e), dependence on the pump photon energy, for the interaction length L and hole density fixed to values optimal for the 200 meV pump. The red line in Fig. 6.4(a) is scaled down by 0.1, so that the green line is also visible in the plot.

Chapter 7

Direct Three Photon Entanglement from TOSPDC process

7.1 Introduction

Usually, $\chi^{(3)}$ value is always much smaller compare to $\chi^{(2)}$,meaning that the second order contributes more in the nonlinear process. But by designing the QW to be symmetric, we can suppress $\chi^{(2)}$ contribution and make third order process as the dominant process. In this chapter, to generate direct three photon entanglement, the nonlinear process that we consider is TOSPDC.

7.2 Third Order SPDC based on valence inter-subband transitions

TOSPDC process is illustrated in Fig. 3.3(b). From Fig. 3.3(b) we can see that this TOSPDC is 4 energy level interaction that requires one pump photon to be converted into 3 photons as the output. These 3 photons are said to be entangled to each other when they are generated in this third order nonlinear process with

maximally entangled GHZ state take form as,

$$|\text{GHZ}\rangle = \frac{|000\rangle + |111\rangle}{\sqrt{2}} \tag{7.1}$$

and $|0\rangle = |\omega_p, X\rangle\,,\ |1\rangle = |\omega_q, X\rangle\,,\ |2\rangle = |\omega_r, Z\rangle$ with $\omega_p + \omega_q + \omega_r = \omega_{pump}$

The multi-qubit state for n qubits can be express in terms of state vectors,

$$|\psi\rangle = \sum_{i=1}^{2^n} \alpha_i \, |x_1 x_2 ... x_n\rangle \,, \tag{7.2}$$

with 2^n different probability amplitudes α_i with $\sum_i |\alpha_i|^2 = 1$ and $x_i \in 0, 1$

The polarisation of TOSPDC is given by Eq. (7.3),

$$\mathbf{P} = \varepsilon_0 \chi^{(3)} \mathbf{E}^3 \tag{7.3}$$

and determined by the third-order nonlinear susceptibility ($\chi^{(3)}$).

Since we focus on intersubband transition involving hole states in QWs, the state energies $E_l(k_x, k_y)$ depend on their quantum index l and the in-plane wave vector (k_x, k_y), and the transition matrix elements also depend on (k_x, k_y), so the summation over all states, discretized in the (k_x, k_y) plane, is written as

$$\begin{aligned}
&\chi^{(3)}_{kijh}(\omega_p + \omega_q + \omega_r; \omega_p, \omega_q, \omega_r) = \frac{N}{\varepsilon_0 \hbar^3} \mathcal{P}_I \sum_{k_x, k_y} \sum_{nvml} \\
&\left\{ \frac{(\rho^{(0)}_{mm} - \rho^{(0)}_{ll}) \mu^k_{mn} \mu^j_{nv} \mu^i_{vl} \mu^h_{lm}}{[\omega_{nm} - \omega_p - \omega_q - \omega_r - i\Gamma_{nm}]\,[\omega_{vm} - \omega_p - \omega_q - i\Gamma_{vm}]\,[\omega_{lm} - \omega_p - i\Gamma_{lm}]} \right. \\
&- \frac{(\rho^{(0)}_{ll} - \rho^{(0)}_{vv}) \mu^k_{mn} \mu^j_{nv} \mu^i_{lm} \mu^h_{vl}}{[\omega_{nm} - \omega_p - \omega_q - \omega_r - i\Gamma_{nm}]\,[\omega_{vm} - \omega_p - \omega_q - i\Gamma_{vm}]\,[\omega_{vl} - \omega_p - i\Gamma_{vl}]} \\
&- \frac{(\rho^{(0)}_{vv} - \rho^{(0)}_{ll}) \mu^k_{mn} \mu^j_{vm} \mu^i_{nl} \mu^h_{lv}}{[\omega_{nm} - \omega_p - \omega_q - \omega_r - i\Gamma_{nm}]\,[\omega_{nv} - \omega_p - \omega_q - i\Gamma_{nv}]\,[\omega_{lv} - \omega_p - i\Gamma_{lv}]} \\
&\left. + \frac{(\rho^{(0)}_{ll} - \rho^{(0)}_{nn}) \mu^k_{mn} \mu^j_{vm} \mu^i_{lv} \mu^h_{nl}}{[\omega_{nm} - \omega_p - \omega_q - \omega_r - i\Gamma_{nm}]\,[\omega_{nv} - \omega_p - \omega_q - i\Gamma_{nv}]\,[\omega_{nl} - \omega_p - i\Gamma_{nl}]} \right\}
\end{aligned} \tag{7.4}$$

with,

$$\rho_{ii}^{(0)} = f_{FD}(E_i(k_x, k_y), E_F) \text{ , for } ii = nn, vv, mm, ll \tag{7.5}$$

7.3 Absorption of the whole nonlinear process

The efficiency of any optical process does not only depend on polarisation, but also on the absorption effect, that will reduce the number of photons generated. This depends on the absorption coefficient for all photons that are correlated in the whole optical process. The absorption coefficient α is calculated from the imaginary part of linear susceptibility ($\chi^{(1)}$), as [64, p. 167]

$$\alpha = \chi^{(1)"}\omega/c \ , \tag{7.6}$$

where $\chi^{(1)"}$ is calculated as

$$\begin{aligned}\chi^{(1)"} =& \frac{\Delta k_x \Delta k_y}{(2\pi)^2 L_z} \frac{e^2}{3\hbar\varepsilon_0} \sum_{k_x,k_y} \sum_{n} \{f_{FD}(E_l(k_x, k_y), E_F) - \\ & f_{FD}(E_m(k_x, k_y), E_F)\} \left|d_{lm}^i\right|^2 \times \\ & \left[\frac{\Gamma_{lm}}{\Gamma_{lm}^2 + (\omega_{lm} - \omega)^2} - \frac{\Gamma_{lm}}{\Gamma_{lm}^2 + (\omega + \omega_{lm})^2}\right].\end{aligned}$$

For resonant structures the absorption peaks at pump and signal / idler photon energies, just as the nonlinear susceptibility does, and must be accounted for.

7.4 Efficiency of TOSPDC process

Number of photon triplets emitted per pump pulse can be approximated by [87],

$$N = \frac{6^2\hbar c^3 k_r' k_s' k_i'}{\sqrt{\pi}\sqrt{k_r'^2 + k_s'^2 + k_i'^2 - k_r' k_s' - k_r' k_i' - k_s' k_i'}} \times \frac{\omega_r \omega_s \omega_i}{\omega_p^2} \frac{n_p^2}{n_r^2 n_s^2 n_i^2} \gamma^2 L p \sigma_f \tag{7.7}$$

with k'_μ is the first derivative $(dk/d\omega)$ of k_μ for $\mu = r, s, i$ and p ,$k = n\omega/c$ and γ as below

$$\gamma = \frac{3\chi^{(3)}\omega_p}{4\varepsilon_0 c^2 n_p^2 A_{eff}} \tag{7.8}$$

where A_{eff} is the pump interaction area which we take as $1mm^2$.

For pump pulse, the number of pump photons N_p is given by,

$$N_p = \frac{p}{\hbar\omega_{p0}} \tag{7.9}$$

So the efficiency of TOSPDC process would become N/N_p, by taking the filter bandwidth $\sigma_f = 1$.

In bulk material, refractive index can be calculated using Sellmayer's equation and the relation between refractive index and the permittivity of one material is defined by $n = \varepsilon^{1/2}$.

In QW layers, for polarization where the electric field of light is parallel to the layers, the average permittivity (ε) is,

$$\varepsilon = \sum_i \varepsilon_i \frac{d_i}{d} \ , \tag{7.10}$$

while for polarization that is normal to the QW layers, the average permittivity is,

$$\frac{1}{\varepsilon} = \sum_i \frac{1}{\varepsilon_i}\frac{d_i}{d} \ . \tag{7.11}$$

where d_i is the thickness of material i and $d = d_1 + d_2 + ... + d_n$, the total thickness of all n layers which make one period of the MQW structure. For simplicity, only phase refractive index is calculated with the help of Sellmayer's equation.

So for electric field of light parallel to QW layers,

$$\varepsilon_{||} = \sum_i \varepsilon_i \frac{d_i}{d_{total}} \ , \tag{7.12}$$

The average permittivity for this polarization is,

$$\varepsilon_{||} = \varepsilon_{\mathrm{GaAs}} \frac{d_{\mathrm{GaAs}}}{d_{total}} + \varepsilon_{\mathrm{AlGaAs}} \frac{d_{\mathrm{AlGaAs}}}{d_{total}} \tag{7.13}$$

and the refractive index for this case is $n_{||}(100\text{meV}) = \varepsilon_{||}^{1/2}$, while for case where electric field of light is normal ($\perp$) to the QW layer, the average permittivity is

$$\frac{1}{\varepsilon_\perp} = \sum_i \frac{1}{\varepsilon_i}\frac{d_i}{d} \tag{7.14}$$

so to calculate average permittivity for this case, Eq (7.14) can be written as,

$$\frac{1}{\varepsilon_\perp} = \frac{1}{\varepsilon_{\text{GaAs}}}\frac{d_{\text{GaAs}}}{d} + \frac{1}{\varepsilon_{\text{AlGaAs}}}\frac{d_{\text{AlGaAs}}}{d} \tag{7.15}$$

and $\varepsilon_\perp$ is just,

$$\left[\frac{1}{\varepsilon_\perp}\right]^{-1} = \left[\frac{1}{\varepsilon_{\text{GaAs}}}\frac{d_{\text{GaAs}}}{d} + \frac{1}{\varepsilon_{\text{AlGaAs}}}\frac{d_{\text{AlGaAs}}}{d}\right]^{-1} \tag{7.16}$$

and the average refractive index for this case, $n_\perp(\omega) = \varepsilon_\perp^{1/2}$ and $k' = n/c$

Since the number of generated photon triplets in Equation (7.7) neglects the absorption, and linearly depends on $\chi^{(3)}$, the $\chi^{(3)}$ value can be set as the target of the optimization process.

7.5 Optimization of $\chi^{(3)}$

In introduction section, we already mentioned that, we need to suppress the second order nonlinear contribution so that third order nonlinearity becomes dominant. So in optimization process, we only consider symmetric structures, by making sure that the well/barrier structures and holes distribution is symmetric during whole optimization process. Three QWs (TQW) symmetric structure with equally deep wells is chosen because, this kind of structure is much easier to fabricate, and the number of parameters that need to be varied is small, which is similar to asymmetric DQW.

During optimization, some parameters are kept equal so that the structure is always symmetric. As in Figure 7.1 QW's width for QW1 is always equal to QW3 and both barrier's widths (B1 and B2) are kept the same. The position of dopants (D1 and D2) in QW1, QW3 respectively also being kept symmetric. By

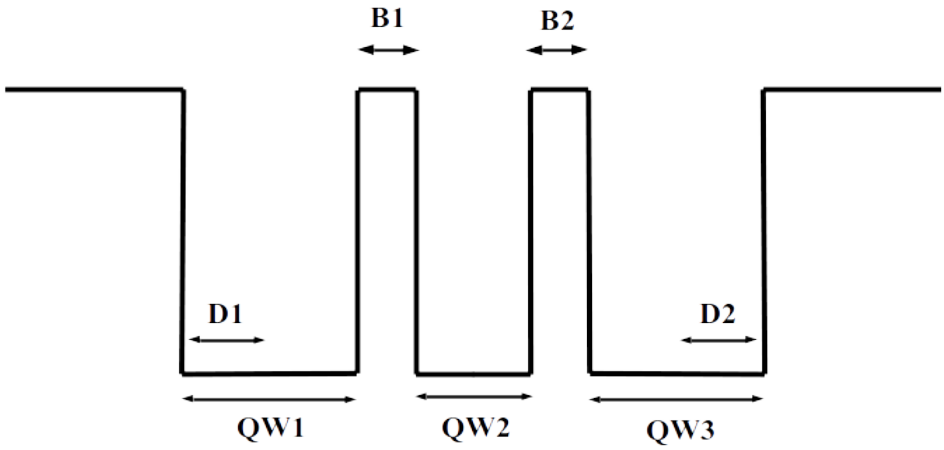

Figure 7.1: Symmetric TQW that used during optimization process

doing this, we can reduce the number of parameters from five to only three.

The optimization process is based on genetic optimization which was already discussed in Section 5.3 and Appendix E. As mentioned in Chapter 6, the product of dipole matrix elements depends on (k_x, k_y) and the value for each k-point is replicated for each quarter plane. So, we can only consider a quarter of the (k_x, k_y) plane during the whole optimization process.

For simplicity, degenerate TOSPDC is chosen by setting the pump photon to be 80meV and the three output photon energies fixed at pump energy divided by three. The holes density is kept low so that the space charge does not perturbed the whole system during the optimization process, and the temperature is set to 77K.

Figure 7.2 shows the optimization process for 8 different parents that is genetically modified for 7 cycles. The parents were distributed equally in the parameters space used, with step width equal to $50\mathring{A}$ and genetically modified by halving the step width in each cycle. By doing this, we could say that we cover every possible well/barrier width during the optimization process. Each cycle will have 27 (3 different parameters $\times$ 3 different widths) different daughters and the daughters with highest $\chi^{(3)}$ will become the next parents in the next optimization cycle until the step width is equal to $1\mathring{A}$. At the end of optimization, the best daughter out of different parents is our optimised heterostructure.

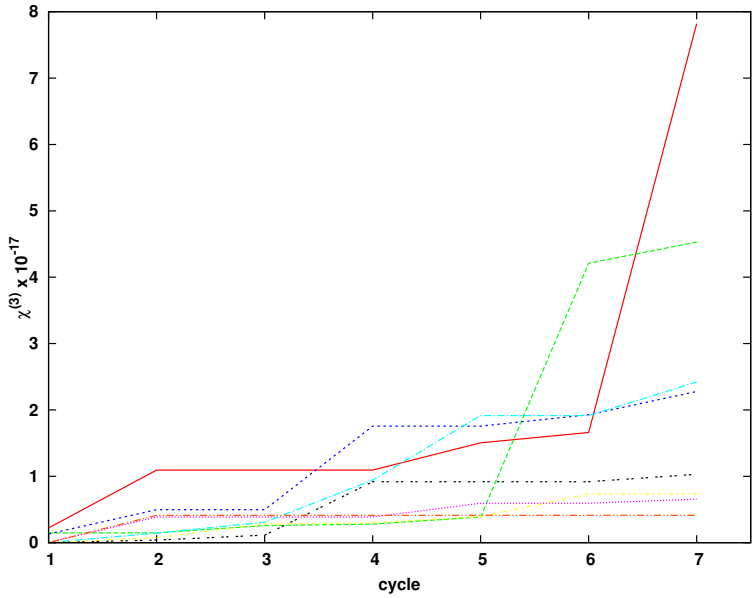

Figure 7.2: The optimization process

.

Table 7.1 shows several best daugther structures coming from different parents. From here, the best daugther out of all parents will be used in the further analysis.

7.6 Effects of holes density and temperature on the $\chi^{(3)}$ value

In this section we consider the effect of the hole density, while keeping the interaction length fixed to 100μm, on the TOSPDC efficiency. The holes density was varied from 5×10^{6} to 5×10^{12} cm^{-2}, and the best (fully optimised) structure from Table 7.1 was used. Since the TOSPDC efficiency linearly depends on $\chi^{(3)}$ (Eq.(7.4 - 7.9) the plots in Fig. 7.3 (a) and (b) look similarly except that (a) is the efficiency of TOSPDC process and (b) is the $\chi^{(3)}$ value for different holes density values.

As shown in Fig. 7.3(a), there exists an optimum density, for which the SPDC efficiency is largest. The reason behind this is that, there are areas in the (k_x, k_y)

Table 7.1: The partially or fully optimized DQW structures and the value of $\chi^{(3)}$, respectively.

structure	$\chi^{(3)}$ **(m^2/V^2)**
100/54/4/80/4/541/100	7.82×10^{-17}
100/2/28/4/28/2/100	4.53×10^{-17}
100/35/11/21/11/35/100	2.28×10^{-17}
100/51/6/58/6/51/100	2.42×10^{-17}
100/42/49/66/49/42/100	7.35×10^{-18}
100/8/27/8/27/8/100	6.57×10^{-18}

plane where the relevant combination of dipole matrix elements has very high values. At low temperatures (T=77K) holes populate almost fully all the (k_x, k_y) states below the Fermi level, and states above it are almost empty. Increasing the hole density increases the Fermi level, and expands the range of (k_x, k_y) states which are populated. The fact that $\chi^{(3)}$ increases slowly for small hole densities, and then much faster for large hole densities (0.1 to 5 $\times10^{12}$ cm^{-2}) , means that the largest contribution to $\chi^{(3)}$ comes from (k_x, k_y) which are not so small. Therefore, a sufficiently large hole density must be provided in order to populate all states with lower energies first, and only then will these most active (k_x, k_y) states become populated, so $\chi^{(3)}$ will then strongly increase.

However, further increase of holes density populates states with even larger (k_x, k_y), where the $\{\ldots\}$ term in Eq.(7.4) changes sign, and the value of $\chi^{(3)}$ will then actually decrease, as displayed in Fig. 7.3(b).

To this extent, the physical explanation of the behaviour of $\chi^{(3)}$ with holes density is similar to that of $\chi^{(2)}$, discussed in Chapter 6. However, the variation of $\chi^{(3)}$ with temperature (which also causes holes redistribution over the states in (k_x, k_y) plane) is different, with $\chi^{(3)}$ increasing with increasing temperature. This comes from different expressions for $\chi^{(2)}$ and $\chi^{(3)}$. In any case, the proper choice of holes density at the device operating temperature is important in providing the maximum TOSPDC efficiency.

Table 7.2: The optimal values of hole density and interaction length for the structure (100/54/4/80/4/54/100), at different temperatures.

T (K)	**Optim. hole density (cm^{-2})**
77	4.8×10^{12}
200	4.2×10^{12}
300	3.9×10^{12}

7.7 Variation of pump photon energy

For this purpose we have chosen the optimal structure with (temperature-dependent) optimal values of holes density, given in Table 7.2, and varied the pump photon energy from 50 to 100 meV (and the output photons energy is always a third of that value). The results are shown in Fig.7.4, and show that TOSPDC based on valence intersubband transitions is more narrow-band ($\sim$10 meV) than was the case for second-order nonlinearity based SPDC.

7.8 Conclusion

In this Chapter the optimal design of p-doped MQW structure was performed, using the genetic algorithm, to deliver the best structures for $\chi^{(3)}$-based TOSPDC process. The constraint that the structure must be symmetric was imposed in this optimisation, in order to disable any second-order nonlinearity. The results show that the correct choice of holes density is important in these structures, and also that $\chi^{(3)}$ improves with the operating temperature, in contrast to structures designed for the $\chi^{(2)}$-based SPDC process.

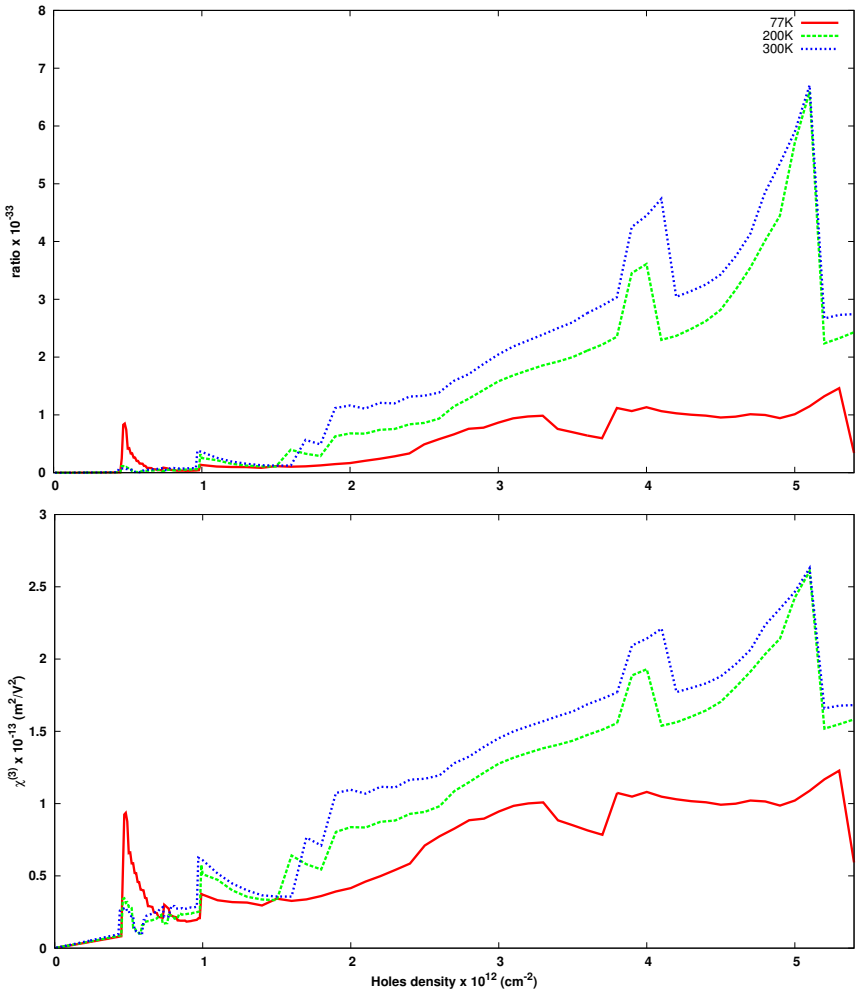

Figure 7.3: The hole density dependence of relevant parameters in the fully optimised structure at different temperatures: (a) conversion ratio, (b) $\chi^{(3)}$
.

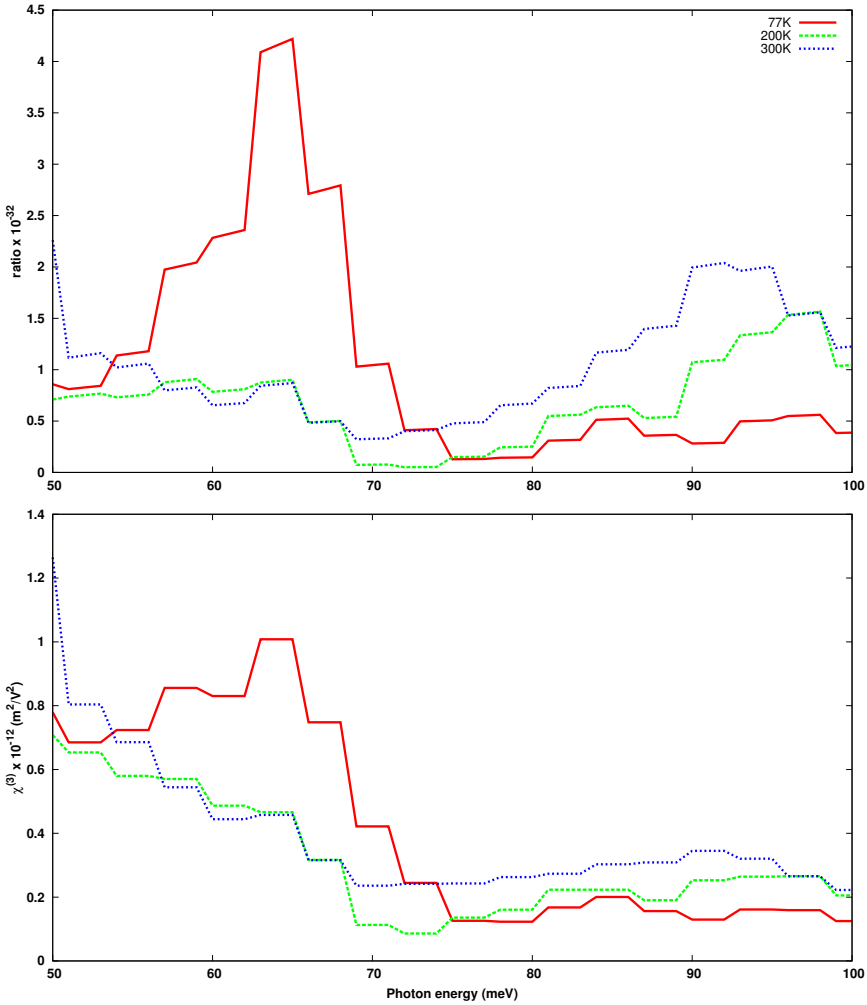

Figure 7.4: (a)Three photon generation efficiency and (b) $\chi^{(3)}$ dependence on the pump photon energy

.

Chapter 8

Concluding Remarks

A range of $Al_xGa_{1-x}As$/GaAs semiconductor heterostructures have been investigated to select the best designs for non-linear optical processes for quantum information technologies. This chapter summarises the findings in the relevant chapters and presents several possibilities for future work.

Quantum information technologies require reliable sources of correlated/entangled photons. PDC is believed to be a highly prospective entangled photon source. By manipulating the well and barrier widths, we could design optimal heterostructures for generating twin and triple entangled photons. As discussed in Chapter 5, non-parabolic effective mass approximation is used to calculate the subband energies and the wave functions in the CB. The details of the method are discussed in Section 3.1. The 6-band K·p method, described in Section 3.2, is used in calculating the subband energies and the wave functions in the VB, for Chapters 6 and 7.

The good agreement of results in Chapter 4 with the results of the semi-analytical method from [59], although not directly describing the entangled photon generation, support the validity and accuracy of the methodology used for the nonlinear susceptibility calculation in Chapters 5 - 7, and the design of optimal semiconductor heterostructures for entangled photon sources.

The design of spectrally entangled photon sources is presented in Chapter 5. In the present work we show that, in calculating the dipole matrix elements, the nonparabolicity effects must be included in such a way that the dipole matrix elements values are independent on the choice of the coordinate origin. The genetic

optimization performed in Chapter 5 enables finding optimal heterostructures for this purpose. This was used for designing optimal structures for both almost-degenerate and for non-degenerate cases. Both cases result in good values of Schimdt's number, meaning that these optimal structure can be used as sources of entangled photons.

In Chapter 5, since the transitions occur in the CB it is not possible to produce entangled photons with different polarizations, because the involved states microscopically have s-like character. To overcome this, transitions between states which have p-like character, that can produce photons with different polarizations, were studied in Chapter 6. The 6-band k·p method is used to calculate the subband energies, wave functions and dipole matrix elements for transitions in the VB. Only the case of degenerate entangled photons was considered, since these photons can have different polarizations. In optimizing the QW structure, we considered asymmetric structures only, because only these enable non-zero $\chi^{(2)}$ values. We also find that there are areas in the (k_x, k_y) plane which have opposite signs of their contributions to the total $\chi^{(2)}$ value. This will affect the total efficiency of the SPDC process. Therefore, increasing the holes density to enhance the conversion rate does not necessarily mean that $\chi^{(2)}$ and the SPDC process will be high. Choosing the correct value of holes density is therefore necessary. The optimal structure is also found to be useful for a range of pump photon energies.

Both of optimised QW structures, in Chapters 5 and 6, produce Bell state entangled photons. GHZ states are multiparticle entangled states. Their generation is considered in Chapter 7, by designing the optimal structure for direct TOSPDC, by making use of the third order nonlinearity. To achieve this, the second order nonlinearity is suppressed by using symmetric structures only, so that the third order nonlinear processes become dominant. The optimal structure designed in Chapter 7 also has hugely varying contributions to the total $\chi^{(3)}$ across the (k_x, k_y) plane.

8.1 Further work

In the present work we have designed optimal structures in Chapters 5 - 7 for specific applications. These can be starting points for further work on optimization, to fine tune the structures for different applications. This will decrease the required optimization time.

Increasing the number of QWs is the best way for further tuning of the energy states and wave functions, to possibly increase the nonlinear susceptibility and efficiency of the PDC process. This would be suitable for future work, with larger computational resources.

In Chapters 5 - 7, general equations for $\chi^{(2)}$ and $\chi^{(3)}$ were used in the optimization. The same optimization method can be applied to different nonlinear processes, for example second/third harmonic generation, sum or difference frequency mixing, or others, as discussed in Section 3.3.2. But of course these would need different target functions for efficiency.

In Chapters 6 and 7, the maximum energy spacing between states is kept below 200meV, in order to limit the number of energy states calculated, but this also limits the range of photon energies for which the structure is optimised. Increasing it would require a much larger number of states to be included, and therefore would require a much larger computational time and resources, but this would be necessary if we want to expand the range of photon energies towards the near-infrared.

The $\chi^{(3)}$ calculation in Chapter 7 can be improved by using the accurately calculated group refractive index, although we believe that the difference will be small compared to the present calculation using the phase refractive index.

Appendix A : Derivation for SHG Nonlinear Susceptibility

Referring to Figure 3.2, Equation (6.2) can be reduced to Equation (3.62) by following derivation;

$$
\begin{aligned}
\chi^{(2)}\left(\omega_2,\omega_1,\omega_0\right) =& \frac{e^3 N}{2\epsilon_0\hbar^2}\left[\left(\rho_{11}^{(0)}-\rho_{22}^{(0)}\right) d_{13}d_{32}d_{21}\right. \\
&\times\left\{\left([(\omega_{31}-\omega_0-\omega_1)-i\Gamma_{31}]\left[(\omega_{21}-\omega_0)-i\Gamma_{21}\right]\right)^{-1}\right. && \text{(1a)}\\
&+\left([(\omega_{31}-\omega_0-\omega_1)-i\Gamma_{31}]\left[(\omega_{21}-\omega_1)-i\Gamma_{21}\right]\right)^{-1} && \text{(1b)}\\
&+\left([(\omega_{32}+\omega_0+\omega_1)+i\Gamma_{32}]\left[(\omega_{21}-\omega_0)-i\Gamma_{21}\right]\right)^{-1} && \text{(1c)}\\
&\left.+\left([(\omega_{32}+\omega_0+\omega_1)+i\Gamma_{32}]\left[(\omega_{21}-\omega_1)-i\Gamma_{21}\right]\right)^{-1}\right\} && \text{(1d)}\\
&+\left(\rho_{11}^{(0)}-\rho_{33}^{(0)}\right) d_{12}d_{23}d_{31} \\
&\times\left\{\left([(\omega_{21}-\omega_0-\omega_1)-i\Gamma_{21}]\left[(\omega_{31}-\omega_0)-i\Gamma_{31}\right]\right)^{-1}\right. && \text{(1e)}\\
&+\left([(\omega_{21}-\omega_0-\omega_1)-i\Gamma_{21}]\left[(\omega_{31}-\omega_1)-i\Gamma_{31}\right]\right)^{-1} && \text{(1f)}\\
&+\left([(\omega_{23}+\omega_0+\omega_1)+i\Gamma_{23}]\left[(\omega_{31}-\omega_0)-i\Gamma_{31}\right]\right)^{-1} && \text{(1g)}\\
&\left.+\left([(\omega_{23}+\omega_0+\omega_1)+i\Gamma_{23}]\left[(\omega_{31}-\omega_1)-i\Gamma_{31}\right]\right)^{-1}\right\} && \text{(1h)}\\
&+\left(\rho_{22}^{(0)}-\rho_{11}^{(0)}\right) d_{23}d_{31}d_{12} \\
&\times\left\{\left([(\omega_{32}-\omega_0-\omega_1)-i\Gamma_{32}]\left[(\omega_{12}-\omega_0)-i\Gamma_{12}\right]\right)^{-1}\right. && \text{(1i)}\\
&+\left([(\omega_{32}-\omega_0-\omega_1)-i\Gamma_{32}]\left[(\omega_{12}-\omega_1)-i\Gamma_{12}\right]\right)^{-1} && \text{(1j)}\\
&+\left([(\omega_{31}+\omega_0+\omega_1)+i\Gamma_{31}]\left[(\omega_{12}-\omega_0)-i\Gamma_{12}\right]\right)^{-1} && \text{(1k)}\\
&\left.+\left([(\omega_{31}+\omega_0+\omega_1)+i\Gamma_{31}]\left[(\omega_{12}-\omega_1)-i\Gamma_{12}\right]\right)^{-1}\right\} && \text{(1l)}
\end{aligned}
$$

$$
\begin{aligned}
&+\left(\rho_{22}^{(0)}-\rho_{33}^{(0)}\right) d_{21}d_{13}d_{32} \\
&\times\left\{\left([(\omega_{12}-\omega_0-\omega_1)-i\Gamma_{12}]\,[(\omega_{32}-\omega_0)-i\Gamma_{32}]\right)^{-1}\right. && \text{(1m)}\\
&+\left([(\omega_{12}-\omega_0-\omega_1)-i\Gamma_{12}]\,[(\omega_{32}-\omega_1)-i\Gamma_{32}]\right)^{-1} && \text{(1n)}\\
&+\left([(\omega_{13}+\omega_0+\omega_1)+i\Gamma_{13}]\,[(\omega_{32}-\omega_0)-i\Gamma_{32}]\right)^{-1} && \text{(1o)}\\
&\left.+\left([(\omega_{13}+\omega_0+\omega_1)+i\Gamma_{13}]\,[(\omega_{32}-\omega_1)-i\Gamma_{32}]\right)^{-1}\right\} && \text{(1p)}\\
&+\left(\rho_{33}^{(0)}-\rho_{11}^{(0)}\right) d_{32}d_{21}d_{13} \\
&\times\left\{\left([(\omega_{23}-\omega_0-\omega_1)-i\Gamma_{23}]\,[(\omega_{13}-\omega_0)-i\Gamma_{13}]\right)^{-1}\right. && \text{(1q)}\\
&+\left([(\omega_{23}-\omega_0-\omega_1)-i\Gamma_{23}]\,[(\omega_{13}-\omega_1)-i\Gamma_{13}]\right)^{-1} && \text{(1r)}\\
&+\left([(\omega_{21}+\omega_0+\omega_1)+i\Gamma_{21}]\,[(\omega_{13}-\omega_0)-i\Gamma_{13}]\right)^{-1} && \text{(1s)}\\
&\left.+\left([(\omega_{21}+\omega_0+\omega_1)+i\Gamma_{21}]\,[(\omega_{13}-\omega_1)-i\Gamma_{13}]\right)^{-1}\right\} && \text{(1t)}\\
&+\left(\rho_{33}^{(0)}-\rho_{22}^{(0)}\right) d_{31}d_{12}d_{23} \\
&\times\left\{\left([(\omega_{13}-\omega_0-\omega_1)-i\Gamma_{13}]\,[(\omega_{23}-\omega_0)-i\Gamma_{23}]\right)^{-1}\right. && \text{(1u)}\\
&+\left([(\omega_{13}-\omega_0-\omega_1)-i\Gamma_{13}]\,[(\omega_{23}-\omega_1)-i\Gamma_{23}]\right)^{-1} && \text{(1v)}\\
&+\left([(\omega_{12}+\omega_0+\omega_1)+i\Gamma_{12}]\,[(\omega_{23}-\omega_0)-i\Gamma_{23}]\right)^{-1} && \text{(1w)}\\
&\left.+\left([(\omega_{12}+\omega_0+\omega_1)+i\Gamma_{12}]\,[(\omega_{23}-\omega_1)-i\Gamma_{23}]\right)^{-1}\right\]. && \text{(1x)}
\end{aligned}
$$

In this case (SHG), $\omega_0=\omega_1=\omega$ and $\omega_2=2\omega$. Referring to Figure 3.2 and considering the nearly double resonant condition, only four terms in Equation (1) will be taken into account which are (1a), (1b), (1o) and (1p) terms. The others will be neglected because only those four terms will give high matrix elements' value. Equation (1) then reduces to;

$$
\begin{aligned}
\chi^{(2)}(2\omega,\omega,\omega) =& \frac{e^3N}{2\epsilon_0\hbar^2}\left[\left(\rho_{11}^{(0)}-\rho_{22}^{(0)}\right) d_{13}d_{32}d_{21}\right. \\
&\times\left\{\left([(\omega_{31}-2\omega)-i\Gamma_{31}]\,[(\omega_{21}-\omega)-i\Gamma_{21}]\right)^{-1}\right. \\
&\left.+\left([(\omega_{31}-2\omega)-i\Gamma_{31}]\,[(\omega_{21}-\omega)-i\Gamma_{21}]\right)^{-1}\right\} \\
&+\left(\rho_{22}^{(0)}-\rho_{33}^{(0)}\right) d_{21}d_{13}d_{32} \\
&\times\left\{\left([(\omega_{13}+2\omega)+i\Gamma_{13}]\,[(\omega_{32}-\omega)-i\Gamma_{32}]\right)^{-1}\right.
\end{aligned}
$$

$$
\begin{aligned}
&+\left(\left[\left(\omega_{13}+2\omega\right)+i\Gamma_{13}\right]\left[\left(\omega_{32}-\omega\right)-i\Gamma_{32}\right]\right)^{-1}\Big\}\Big] \\
=&\frac{e^3N}{2\epsilon_0\hbar^2}\left[2\left(\rho_{11}^{(0)}-\rho_{22}^{(0)}\right)d_{13}d_{32}d_{21}\right. \\
&\times\left(\left[\omega_{31}-2\omega-i\Gamma_{31}\right]\left[\omega_{21}-\omega-i\Gamma_{21}\right]\right)^{-1} \\
&+2\left(\rho_{22}^{(0)}-\rho_{33}^{(0)}\right)d_{21}d_{13}d_{32} \\
&\left.\times\left(\left[\omega_{13}+2\omega+i\Gamma_{13}\right]\left[\omega_{32}-\omega-i\Gamma_{32}\right]\right)^{-1}\right] \\
=&\frac{e^3d_{13}d_{32}d_{21}N}{\epsilon_0\hbar^2}\left[\frac{\rho_{11}^{(0)}-\rho_{22}^{(0)}}{\left[\omega_{31}-2\omega-i\Gamma_{31}\right]\left[\omega_{21}-\omega-i\Gamma_{21}\right]}\right. \\
&\left.+\frac{\rho_{22}^{(0)}-\rho_{33}^{(0)}}{\left[\omega_{13}+2\omega+i\Gamma_{13}\right]\left[\omega_{32}-\omega-i\Gamma_{32}\right]}\right]. \qquad (2a)
\end{aligned}
$$

Using $\omega_{ij}=-\omega_{ji}$, and volume density $N\rho_{ii}^{(0)}=n_i/L_z$, Equation (2a) can be simplified to:

$$
\begin{aligned}
\chi^{(2)}\left(2\omega,\omega,\omega\right)=&\frac{e^3}{L_z\epsilon_0\hbar^2}d_{13}d_{32}d_{21}\left[\frac{n_1-n_2}{\left[\omega_{31}-2\omega-i\Gamma_{31}\right]\left[\omega_{21}-\omega-i\Gamma_{21}\right]}\right. \\
&\left.+\frac{n_2-n_3}{\left[\omega_{13}+2\omega+i\Gamma_{13}\right]\left[\omega_{32}-\omega-i\Gamma_{32}\right]}\right] \\
=&\frac{e^3}{L_z\epsilon_0\hbar^2}d_{13}d_{32}d_{21}\left[\frac{n_1-n_2}{\left[\omega_{31}-2\omega-i\Gamma_{31}\right]\left[\omega_{21}-\omega-i\Gamma_{21}\right]}\right. \\
&\left.+\frac{(-1)(n_3-n_2)}{(-1)\left[\omega_{31}-2\omega-i\Gamma_{31}\right]\left[\omega_{32}-\omega-i\Gamma_{32}\right]}\right] \\
=&\frac{e^3}{L_z\epsilon_0\hbar^2}\frac{d_{13}d_{32}d_{21}}{\left[\omega_{31}-2\omega-i\Gamma_{31}\right]} \\
&\times\left[\frac{n_1-n_2}{\left[\omega_{21}-\omega-i\Gamma_{21}\right]}+\frac{n_3-n_2}{\left[\omega_{32}-\omega-i\Gamma_{32}\right]}\right], \qquad (3a)
\end{aligned}
$$

which is similar to Equation (3.6.17) in [64] Page 175.

Appendix B : Dipole Matrix Derivation from Momentum

Sirtori *et. al* defines his Equation 8 as follows [88],

$$\langle\psi_0|\,\widehat{P}\,|\psi_i\rangle = \frac{1}{2}\langle\psi_0|\,P_z\frac{m_0}{m(E_0,z)} + \frac{m_0}{m(E_i,z)}P_z\,|\psi_i\rangle \tag{4}$$

with $P_z = i\hbar\dfrac{d}{dz}$,Equation (4) can be expanded as,

$$\langle\psi_0|\,\widehat{P}\,|\psi_i\rangle = \frac{m_0}{2}\langle\psi_0|\,P_z\frac{m_0}{m(E_0,z)} + \frac{m_0}{m(E_i,z)}P_z\,|\psi_i\rangle \tag{5a}$$

$$= \frac{m_0}{2}\langle\psi_0|\,i\hbar\frac{d}{dz}\frac{1}{m(E_0,z)} + \frac{1}{m(E_i,z)}i\hbar\frac{d}{dz}\,|\psi_i\rangle \tag{5b}$$

$$= \frac{i\hbar m_0}{2}\left[\int_0^z \psi_0\frac{d}{dz}\left(\frac{\psi_i}{m(E_0,z)}\right)dz + \int_0^z \psi_0\frac{1}{m(E_i,z)}\frac{d\psi_i}{dz}dz\right]. \tag{5c}$$

In numerical approach, differential terms in Equation (5c) can be defined as,

$$\psi_i^{`} = \frac{\psi_{i+1} - \psi_{i-1}}{z_{i+1} - z_{i-1}}. \tag{6}$$

Commutation relation of operator z and H defines the momentum operator,

$$\widehat{P} = \frac{im_0}{\hbar}\left[\widehat{H},\widehat{z}\right]. \tag{7}$$

Using Equation(7), one can define $\langle\psi_0|\,\widehat{P}\,|\psi_i\rangle$ in Equation (4) as,

$$\langle\psi_0|\,\widehat{P}\,|\psi_i\rangle = \frac{im_0}{\hbar}\left[\langle\psi_0|\,\widehat{H}\widehat{z}\,|\psi - i\rangle - \langle\psi_0|\,\widehat{z}\widehat{H}\,|\psi - i\rangle\right] \tag{8a}$$

$$= \frac{im_0}{\hbar}\left[\langle\widehat{H}\psi_0|\,\widehat{z}\,|\psi - i\rangle - \langle\psi_0|\,\widehat{z}\,|\widehat{H}\psi - i\rangle\right] \tag{8b}$$

$$= \frac{im_0}{\hbar}\left[E_0\,\langle\psi_0|\,\widehat{z}\,|\psi - i\rangle - E_i\,\langle\psi_0|\,\widehat{z}\,|\psi - i\rangle\right] \tag{8c}$$

$$= \frac{im_0}{\hbar}(E_0 - E_i)\,\langle\psi_0|\,\widehat{z}\,|\psi_i\rangle \tag{8d}$$

By rearranging Equation (8d), the dipole matrix can be written as,

$$\langle\psi_0|\,\widehat{z}\,|\psi_i\rangle = \frac{\hbar}{im_0}\frac{\langle\psi_0|\,\widehat{P}\,|\psi_i\rangle}{E_0 - E_i}. \tag{9}$$

Using Equation (5c), Equation (9) can be written as,

$$\langle\psi_0|\,\widehat{z}\,|\psi_i\rangle = -\frac{\hbar^2/2}{E_o - E_i}\left[\int_0^z \psi_0 \frac{d}{dz}\left(\frac{\psi_i}{m(E_0, z)}\right)dz + \int_0^z \psi_0 \frac{1}{m(E_i, z)}\frac{d\psi_i}{dz}dz\right] \tag{10a}$$

Appendix C : Perturbation Solution of the Time Evolution Density Matrix / Density Matrix Equation of Motion

Boyd in his book [64] page 158 (chapter 3) derives the perturbation solution for Equation (3.54). Equation (3.54) is the time evolution equation of density matrix, also known as density matrix equation of motion. Perturbation term, $\widehat{V}(t)$ in Equation (3.52) is assumed to be weak in the sense that expectation of $\widehat{V}$ is much smaller than expectation value of $\widehat{H_0}$. The interaction energy is assumed adequately given by the electric dipole approximation as,

$$\widehat{V} = -\widehat{\mu} \cdot \mathbf{E}(t) \tag{11}$$

where $\widehat{\mu} = -e\widehat{r}$ which denotes the electric dipole moment operator of the atom. Equation (3.52) will split the commutator $\left[\widehat{H}, \widehat{\rho}\right]$ in Equation (3.54) into two terms. The first terms which is $\left[\widehat{H}_0, \widehat{\rho}\right]$, the unperturbed Hamiltonian $\widehat{H}_0$ satisfies the equation $\widehat{H}_0 u_n = E_n u_n$, where the states n represent the energy eigenfunctions u_n. So the matrix representation of $\widehat{H}_0$ is diagonal,

$$H_{0,nm} = E_n \delta_{nm} \tag{12}$$

The commutator can be expanded as,

$$\left[\widehat{H}_0, \widehat{\rho}\right]_{nm} = \left(\widehat{H}_0\widehat{\rho} - \widehat{\rho}\widehat{H}_0\right)_{nm} \tag{13a}$$

$$= \sum_v \left(\widehat{H}_{0,nv}\rho_{vm} - \rho_{nv}H_{0,vm}\right) \tag{13b}$$

$$= \sum_v \left(E_n\delta_{nv}\rho_{vm} - \rho_{nv}\delta_{vm}E_m\right) \tag{13c}$$

$$= E_n\rho_{nm} - E_m\rho_{nm} = (E_n - E_m)\rho_{nm}. \tag{13d}$$

With angular frequency,

$$\omega_{nm} = \frac{E_n - E_m}{\hbar}, \tag{14}$$

the time evolution equation of density matrix, Equation (3.54), can be written as,

$$\dot{\rho}_{nm} = -i\omega_{nm}\rho_{nm} - \frac{i}{\hbar}\left[\widehat{V}, \widehat{\rho}\right]_{nm} - \Gamma_{nm}\left(\rho_{nm} - \rho_{nm}^{eq}\right) \tag{15}$$

The full derivation on how to get perturbation solution of time evolution equation for the density matrix can referred to [64] in Chapter 3 under Section 3.4 pages 158-161.

Appendix D : Derivation of Optical Transition Matrix Elements at Valence Band

From Section 3.2.2, we start the derivation with 6×6 Hamiltonian and use the commutator properties of the coordinates and derivatives, e.g.

$$\left[\frac{d}{dz}, z\right] = 1, \quad \left[\frac{d^2}{dz^2}, z\right] = 2\frac{d}{dz}, \tag{16a}$$

$$\left[g(z)\frac{d}{dz}, z\right] = g(z), \quad \left[\frac{d}{dz}g(z), z\right] = g(z), \tag{16b}$$

$$\left[\frac{d}{dz}g(z)\frac{d}{dz}, z\right] = \frac{dg(z)}{dz} + 2g(z)\frac{d}{dz} \tag{16c}$$

In the derivation of $\overrightarrow{v}$ operator, we also set $k_x \to -i\partial/\partial_x$ and $k_y \to -i\partial/\partial y$, as well, so e.g. $[k_-, x] = -i$, $[k_-, y] = -1$, $[k_+, x] = -i$, and $[k_+, y] = 1$. Thus, we find the x, y, and z components of the velocity matrix (the factor of $1/\hbar$ in front of the commutator in Equation (3.47 is implicitly assumed in these expressions, along with $\hbar^2/2m_0$, which is absorbed in γ parameters as before):

$$v^z_{1,1} = [P + Q, z] = -\left[\left(\frac{d(\gamma_1 - 2\gamma_2)}{dz}\right) + 2(\gamma_1 - 2\gamma_2)\frac{d}{dz}\right] \tag{17a}$$

$$v^x_{1,1} = [P + Q, x] = -(\gamma_1 + \gamma_2) \cdot 2\frac{d}{dx} \to -2ik_x(\gamma_1 + \gamma_2) \tag{17b}$$

$$v^y_{1,1} = [P + Q, y] = -2ik_y(\gamma_1 + \gamma_2) \tag{17c}$$

$$v^z_{1,2} = v^x_{1,2} = v^y_{1,2} = 0 \tag{18}$$

$$v^z_{1,3} = [-S_-, z] = i2\sqrt{3}k_-(\sigma - \delta + \pi) \tag{19a}$$
$$v^x_{1,3} = [-S_-, x] = 2\sqrt{3}\left[(\sigma - \delta + \pi)\frac{d}{dz} + \left(\frac{d\pi}{dz}\right)\right] \tag{19b}$$
$$v^y_{1,3} = [-S_-, y] = -i2\sqrt{3}\left[(\sigma - \delta + \pi)\frac{d}{dz} + \left(\frac{d\pi}{dz}\right)\right] \tag{19c}$$

$$v^z_{1,4} = [R, z] = 0 \tag{20a}$$
$$v^x_{1,4} = [R, x] = i2\sqrt{3}\overline{\gamma} \cdot k_- - i2\sqrt{3}\mu \cdot k_+ \tag{20b}$$
$$v^y_{1,4} = [R, y] = 2\sqrt{3}\mu \cdot k_+ + 2\sqrt{3}\overline{\gamma} \cdot k_- \tag{20c}$$

$$v^z_{1,5} = [\frac{1}{\sqrt{2}}S_-, z] = -\frac{1}{\sqrt{2}}v^z_{1,3} \tag{21a}$$
$$v^x_{1,5} = [\frac{1}{\sqrt{2}}S_-, x] = -\frac{1}{\sqrt{2}}v^x_{1,3} \tag{21b}$$
$$v^y_{1,5} = [\frac{1}{\sqrt{2}}S_-, y] = -\frac{1}{\sqrt{2}}v^y_{1,3} \tag{21c}$$
$$\tag{21d}$$

$$v^z_{1,6} = [\sqrt{2}R, z] = \sqrt{2}v^z_{1,4} \tag{22a}$$
$$v^x_{1,6} = [\sqrt{2}R, x] = \sqrt{2}v^x_{1,4} \tag{22b}$$
$$v^y_{1,6} = [\sqrt{2}R, y] = \sqrt{2}v^y_{1,4} \tag{22c}$$

$$v^z_{2,1} = v^x 2, 1 = v^y 2, 1 = 0 \tag{23}$$

$$v^z_{2,2} = v^z_{1,1} \tag{24a}$$
$$v^x_{2,2} = v^x_{1,1} \tag{24b}$$
$$v^y_{2,2} = v^y_{1,1} \tag{24c}$$

$$v^z_{2,3} = [-R^\dagger, z] = 0 \tag{25a}$$
$$v^x_{2,3} = [-R^\dagger, x] = -i2\sqrt{3}\overline{\gamma} \cdot k_+ + i2\sqrt{3}\mu \cdot k_- \tag{25b}$$
$$v^y_{2,3} = [-R^\dagger, y] = \sqrt{3}\overline{\gamma} \cdot k_- + i2\sqrt{3}\mu \cdot k_+ \tag{25c}$$

$$v^z_{2,4} = [-S_+, z] = i2\sqrt{3}k_+(\sigma - \delta + \pi) \tag{26a}$$
$$v^x_{2,4} = [-S_+, x] = 2\sqrt{3}\left[(\sigma - \delta + \pi)\frac{d}{dz} + \left(\frac{d\pi}{dz}\right)\right] \tag{26b}$$
$$v^y_{2,4} = [-S_+, y] = i2\sqrt{3}\left[(\sigma - \delta + \pi)\frac{d}{dz} + \left(\frac{d\pi}{dz}\right)\right] \tag{26c}$$

$$v^z_{2,5} = [-\sqrt{2}R^\dagger, z] = \sqrt{2}v^z_{2,3} = 0 \tag{27a}$$
$$v^x_{2,5} = [-\sqrt{2}R^\dagger, x] = \sqrt{2}v^x_{2,3} \tag{27b}$$
$$v^y_{2,5} = [-\sqrt{2}R^\dagger, y] = \sqrt{2}v^y_{2,3} \tag{27c}$$

$$v^z_{2,6} = [\frac{1}{\sqrt{2}}S_+, z] = -\frac{1}{\sqrt{2}}v^z_{2,4} \tag{28a}$$
$$v^x_{2,6} = [\frac{1}{\sqrt{2}}S_+, x] = -\frac{1}{\sqrt{2}}v^x_{2,4} \tag{28b}$$
$$v^y_{2,6} = [\frac{1}{\sqrt{2}}S_+, y] = -\frac{1}{\sqrt{2}}v^y_{2,4} \tag{28c}$$

$$v^z_{3,1} = [-S^\dagger_-, z] = i2\sqrt{3}k_+(\sigma - \delta + \pi) \tag{29a}$$

$$v^x_{3,1} = [-S^\dagger_-, x] = 2\sqrt{3} \cdot \left[(\sigma - \delta + \pi)\frac{d}{dz} + \left(\frac{d(\sigma - \delta)}{dz}\right)\right] \tag{29b}$$

$$v^y_{3,1} = [-S^\dagger_-, y] = i2\sqrt{3} \cdot \left[(\sigma - \delta + \pi)\frac{d}{dz} + \left(\frac{d(\sigma - \delta)}{dz}\right)\right] \tag{29c}$$

$$v^z_{3,2} = [-R, z] = -v^z_{1,4} = 0 \tag{30a}$$

$$v^x_{3,2} = [-R, x] = -v^x_{1,4} \tag{30b}$$

$$v^y_{3,2} = [-R, y] = -v^y_{1,4} \tag{30c}$$

$$v^z_{3,3} = [P - Q, z] = -\left[\left(\frac{d(\gamma_1 + 2\gamma_2)}{dz}\right) + 2(\gamma_1 + 2\gamma_2)\frac{d}{dz}\right] \tag{31a}$$

$$v^x_{3,3} = [P - Q, x] = -(\gamma_1 - \gamma_2) \cdot 2\frac{d}{dx} \to -2ik_x(\gamma_1 - \gamma_2) \tag{31b}$$

$$v^y_{3,3} = [P - Q, y] = -2ik_y(\gamma_1 - \gamma_2) \tag{31c}$$

$$v^z_{3,4} = [C, z] = 0 \tag{32a}$$

$$v^x_{3,4} = [C, x] = -2\left(\frac{d(\sigma - \delta + \pi)}{dz}\right) \tag{32b}$$

$$v^y_{3,4} = [C, y] = i2\left(\frac{d(\sigma - \delta + \pi)}{dz}\right) \tag{32c}$$

$$v^z_{3,5} = [\sqrt{2}Q, z] = 2\sqrt{2}\left[\left(\frac{d\gamma_2}{dz}\right) + 2\gamma_2\frac{d}{dz}\right] \tag{33a}$$

$$v^x_{3,5} = [\sqrt{2}Q, x] = -i2\sqrt{2}k_x\gamma_2 \tag{33b}$$

$$v^y_{3,5} = [\sqrt{2}Q, y] = -i2\sqrt{2}k_y\gamma_2 \tag{33c}$$

$$v^z_{3,6} = \left[\sqrt{3/2}\Sigma_-, z\right] = -i3\sqrt{2}k_-(\sigma - \delta + \pi) \tag{34a}$$

$$v^x_{3,6} = \left[\sqrt{3/2}\Sigma_-, x\right] = -3\sqrt{2}\cdot\left[(\sigma - \delta + \pi)\frac{d}{dz} + \left(\frac{d(2\sigma - 2\delta + \pi)/3}{dz}\right)\right] \tag{34b}$$

$$v^y_{3,6} = \left[\sqrt{3/2}\Sigma_-, y\right] = i3\sqrt{2}\cdot\left[(\sigma - \delta + \pi)\frac{d}{dz} + \left(\frac{d(2\sigma - 2\delta + \pi)/3}{dz}\right)\right] \tag{34c}$$

$$v^z_{4,1} = [R^\dagger, z] = -v^z_{2,3} = 0 \tag{35a}$$

$$v^x_{4,1} = [R^\dagger, x] = -v^x_{2,3} \tag{35b}$$

$$v^y_{4,1} = [R^\dagger, y] = -v^y_{2,3} \tag{35c}$$

$$v^z_{4,2} = [-S^\dagger_+, z] = i2\sqrt{3}k_-(\sigma - \delta + \pi) \tag{36a}$$

$$v^x_{4,2} = [-S^\dagger_+, x] = 2\sqrt{3}\cdot\left[(\sigma - \delta + \pi)\frac{d}{dz} + \left(\frac{d(\sigma - \delta)}{dz}\right)\right] \tag{36b}$$

$$v^y_{4,2} = [-S^\dagger_+, y] = -i2\sqrt{3}\cdot\left[(\sigma - \delta + \pi)\frac{d}{dz} + \left(\frac{d(\sigma - \delta)}{dz}\right)\right] \tag{36c}$$

$$\tag{36d}$$

$$v^z_{4,3} = [C^\dagger, z] = 0 \tag{37a}$$

$$v^x_{4,3} = [C^\dagger, x] = 2\left(\frac{d(\sigma - \delta - \pi)}{dz}\right) \tag{37b}$$

$$v^y_{4,3} = [C^\dagger, y] = i2\left(\frac{d(\sigma - \delta - \pi)}{dz}\right) \tag{37c}$$

$$v^z_{4,4} = v^z_{3,3} \tag{38a}$$

$$v^x_{4,4} = v^x_{3,3} \tag{38b}$$

$$v^y_{4,4} = v^y_{3,3} \tag{38c}$$

$$v^z_{4,5} = \left[-\sqrt{3/2}\Sigma_+, z\right] = i3\sqrt{2}k_+(\sigma - \delta + \pi) \tag{39a}$$

$$v^x_{4,5} = \left[-\sqrt{3/2}\Sigma_+, x\right] = -3\sqrt{2}\cdot\left[(\sigma - \delta + \pi)\frac{d}{dz} + \left(\frac{d(2\sigma - 2\delta + \pi)/3}{dz}\right)\right] \tag{39b}$$

$$v^y_{4,5} = \left[-\sqrt{3/2}\Sigma_+, y\right] = i3\sqrt{2}\cdot\left[(\sigma - \delta + \pi)\frac{d}{dz} + \left(\frac{d(2\sigma - 2\delta + \pi)/3}{dz}\right)\right] \tag{39c}$$

$$v^z_{4,6} = [\sqrt{2}Q, z] = v^z_{3,5} \tag{40a}$$
$$v^x_{4,6} = [\sqrt{2}Q, x] = v^x_{3,5} \tag{40b}$$
$$v^y_{4,6} = [\sqrt{2}Q, y] = v^y_{3,5} \tag{40c}$$

$$v^z_{5,1} = [\frac{1}{\sqrt{2}}S^\dagger_-, z] = -\frac{1}{\sqrt{2}}v^z_{3,1} \tag{41a}$$
$$v^x_{5,1} = [\frac{1}{\sqrt{2}}S^\dagger_-, x] = -\frac{1}{\sqrt{2}}v^x_{3,1} \tag{41b}$$
$$v^y_{5,1} = [\frac{1}{\sqrt{2}}S^\dagger_-, y] = -\frac{1}{\sqrt{2}}v^y_{3,1} \tag{41c}$$

$$v^z_{5,2} = [-\sqrt{2}R, z] = \sqrt{2}v^z_{1,6} \tag{42a}$$
$$v^x_{5,2} = [-\sqrt{2}R, x] = \sqrt{2}v^x_{1,6} \tag{42b}$$
$$v^y_{5,2} = [-\sqrt{2}R, y] = \sqrt{2}v^y_{1,6} \tag{42c}$$

$$v^z_{5,3} = [\sqrt{2}Q, z] = \sqrt{2}v^z_{3,5} \tag{43a}$$

$$v_{5,3}^{x} = [\sqrt{2}Q, x] = \sqrt{2}v_{3,5}^{x} \tag{43b}$$
$$v_{5,3}^{y} = [\sqrt{2}Q, y] = \sqrt{2}v_{3,5}^{y} \tag{43c}$$

$$v_{5,4}^{z} = \left[-\sqrt{3/2}\Sigma_{+}^{\dagger}, z\right] = i3\sqrt{2}k_{-}(\sigma - \delta + \pi) \tag{44a}$$
$$v_{5,4}^{x} = \left[-\sqrt{3/2}\Sigma_{+}^{\dagger}, x\right] = 3\sqrt{2} \cdot \left[(\sigma - \delta + \pi)\frac{d}{dz} + \left(\frac{d(\sigma - \delta + 2\pi)/3}{dz}\right)\right] \tag{44b}$$
$$v_{5,4}^{y} = \left[-\sqrt{3/2}\Sigma_{+}^{\dagger}, y\right] = -i3\sqrt{2} \cdot \left[(\sigma - \delta + \pi)\frac{d}{dz} + \left(\frac{d(\sigma - \delta + 2\pi)/3}{dz}\right)\right] \tag{44c}$$

$$v_{5,5}^{z} = [P, z] = -\left(\frac{d\gamma_1}{dz}\right) - 2\gamma_1\frac{d}{dz} \tag{45a}$$
$$v_{5,5}^{x} = [P, x] = -i2\sqrt{2}k_x\gamma_1 \tag{45b}$$
$$v_{5,5}^{y} = [P, y] = -i2\sqrt{2}k_y\gamma_1 \tag{45c}$$

$$v_{5,6}^{z} = [-C, z] = -v_{3,4}^{z} = 0 \tag{46a}$$
$$v_{5,6}^{x} = [-C, x] = -v_{3,4}^{x} \tag{46b}$$
$$v_{5,6}^{y} = [-C, y] = -v_{3,4}^{y} \tag{46c}$$

$$v_{6,1}^{z} = [\sqrt{2}R^{\dagger}, z] = -v_{2,5}^{z} = 0 \tag{47a}$$
$$v_{6,1}^{x} = [\sqrt{2}R^{\dagger}, x] = -v_{2,5}^{x} \tag{47b}$$
$$v_{6,1}^{y} = [\sqrt{2}R^{\dagger}, y] = -v_{2,5}^{y} \tag{47c}$$

$$v_{6,2}^{z} = [\frac{1}{\sqrt{2}}S_{+}^{\dagger}, z] = -i\sqrt{3}\sqrt{2}k_{-}(\sigma - \delta + \pi) \tag{48a}$$

$$v^x_{6,2} = [\frac{1}{\sqrt{2}} S^\dagger_+, x] = -\sqrt{3}\sqrt{2} \cdot \left[(\sigma - \delta + \pi) \frac{d}{dz} + \left(\frac{d(\sigma - \delta)}{dz} \right) \right] \tag{48b}$$

$$v^y_{6,2} = [\frac{1}{\sqrt{2}} S^\dagger_+, y] = i\sqrt{3}\sqrt{2} \cdot \left[(\sigma - \delta + \pi) \frac{d}{dz} + \left(\frac{d(\sigma - \delta)}{dz} \right) \right] \tag{48c}$$

$$v^z_{6,3} = \left[-\sqrt{3/2}\Sigma^\dagger_-, z \right] = -i3\sqrt{2}k_+(\sigma - \delta + \pi) \tag{49a}$$

$$v^x_{6,3} = \left[-\sqrt{3/2}\Sigma^\dagger_-, x \right] = -3\sqrt{2} \cdot \left[(\sigma - \delta + \pi) \frac{d}{dz} + \left(\frac{d(2\sigma - 2\delta + \pi)/3}{dz} \right) \right] \tag{49b}$$

$$v^y_{6,3} = \left[-\sqrt{3/2}\Sigma^\dagger_-, y \right] = i3\sqrt{2} \cdot \left[(\sigma - \delta + \pi) \frac{d}{dz} + \left(\frac{d(2\sigma - 2\delta + \pi)/3}{dz} \right) \right] \tag{49c}$$

$$v^z_{6,4} = [\sqrt{2}Q, z] = \sqrt{2} v^z_{3,5} \tag{50a}$$

$$v^x_{6,4} = [\sqrt{2}Q, x] = \sqrt{2} v^x_{3,5} \tag{50b}$$

$$v^y_{6,4} = [\sqrt{2}Q, y] = \sqrt{2} v^y_{3,5} \tag{50c}$$

$$v^z_{6,5} = [-C^\dagger, z] = -v^z_{4,3} = 0 \tag{51a}$$

$$v^x_{6,5} = [-C^\dagger, x] = -v^x_{4,3} \tag{51b}$$

$$v^y_{6,5} = [-C^\dagger, y] = -v^y_{4,3} \tag{51c}$$

$$v^z_{6,6} = [P, z] = v^z_{5,5} \tag{52a}$$

$$v^x_{6,6} = [P, x] = v^x_{5,5} \tag{52b}$$

$$v^y_{6,6} = [P, y] = v^z_{5,5} \tag{52c}$$

Bibliography

[1] G. Gurzadëiìan, V. Dmitriev, and D. Nikogosëiìan, "Handbook of nonlinear optical crystals," *3rd, rev. edition (Springer, Berlin*, 1999. xii, 30

[2] A. Einstein, B. Podolsky, and N. Rosen, "Can quantum-mechanical description of physical reality be considered complete?," *Phys. Rev.*, vol. 47, pp. 777–780, May 1935. 1

[3] J. S. Bell *et al.*, "On the einstein-podolsky-rosen paradox," *Physics*, vol. 1, no. 3, pp. 195–200, 1964. 1

[4] A. K. Ekert, "Quantum cryptography based on bell's theorem," *Phys. Rev. Lett.*, vol. 67, pp. 661–663, Aug 1991. 2

[5] P. P. Rohde, "Optical quantum computing with photons of arbitrarily low fidelity and purity," *PHYSICAL REVIEW A*, vol. 86, NOV 19 2012. 2

[6] C. H. Bennett, G. Brassard, C. Crépeau, R. Jozsa, A. Peres, and W. K. Wootters, "Teleporting an unknown quantum state via dual classical and einstein-podolsky-rosen channels," *Phys. Rev. Lett.*, vol. 70, pp. 1895–1899, Mar 1993. 2

[7] N. Gisin, G. Ribordy, W. Tittel, and H. Zbinden, "Quantum cryptography," *Reviews of modern physics*, vol. 74, no. 1, pp. 145–195, 2002. 2

[8] C. H. Bennett, G. Brassard, C. Crépeau, R. Jozsa, A. Peres, and W. K. Wootters, "Teleporting an unknown quantum state via dual classical and einstein-podolsky-rosen channels," *Physical Review Letters*, vol. 70, no. 13, p. 1895, 1993. 2

[9] M. A. Nielsen and I. L. Chuang, *Quantum computation and quantum information*. Cambridge university press, 2010. 2

[10] L. Esaki and R. Tsu, "Superlattice and negative differential conductivity in semiconductors," *I B M J RES DEVELOP*, vol. 14, no. 1, pp. 61–65, 1970. 6

[11] L. Chang, L. Esaki, W. Howard, and R. Ludeke, "The growth of a gaas–gaalas superlattice," *Journal of Vacuum Science & Technology*, vol. 10, no. 1, pp. 11–16, 1973. 6

[12] P. Franken, A. Hill, C. e. Peters, and G. Weinreich, "Generation of optical harmonics," *Physical Review Letters*, vol. 7, no. 4, p. 118, 1961. 8

[13] R. Dingle, W. Wiegmann, and C. H. Henry, "Quantum states of confined carriers in very thin al x ga 1- x as-gaas-al x ga 1- x as heterostructures," *Physical Review Letters*, vol. 33, no. 14, p. 827, 1974. 8

[14] M. O. Scully and M. S. Zubairy, *Quantum optics*. Cambridge university press, 1997. 9

[15] M. Planck, "On the law of distribution of energy in the normal spectrum," *Annalen der Physik*, vol. 4, no. 553, p. 1, 1901. 9

[16] A. Einstein, "Concerning an heuristic point of view toward the emission and transformation of light," *American Journal of Physics*, vol. 33, no. 5, p. 367, 1965. 9

[17] G. N. Lewis, "The conservation of photons," *Nature*, vol. 118, pp. 874–875, 1926. 9

[18] P. Grangier, B. Sanders, and J. Vuckovic, "Focus on single photons on demand," *New Journal of Physics*, vol. 6, no. 1, 2004. 9

[19] D. Klyshko, "Photons and nonlinear optics," 1988. 9, 61

[20] F. De Martini and F. Sciarrino, "Non-linear parametric processes in quantum information," *Progress in quantum electronics*, vol. 29, no. 3, pp. 165–256, 2005. 10

[21] D. C. Burnham and D. L. Weinberg, "Observation of simultaneity in parametric production of optical photon pairs," *Physical Review Letters*, vol. 25, no. 2, p. 84, 1970. 10

[22] C. Hong and L. Mandel, "Experimental realization of a localized one-photon state," *Physical Review Letters*, vol. 56, pp. 58–60, 1986. 10

[23] C. Hong, Z. Ou, and L. Mandel, "Measurement of subpicosecond time intervals between two photons by interference," *Physical Review Letters*, vol. 59, no. 18, pp. 2044–2046, 1987. 10

[24] R. Ghosh and L. Mandel, "Observation of nonclassical effects in the interference of two photons," *Physical review letters*, vol. 59, pp. 1903–1905, 1987. 10

[25] L. Mandel, "Quantum effects in one-photon and two-photon interference," in *More Things in Heaven and Earth*, pp. 460–473, Springer, 1999. 10

[26] L. Mandel and E. Wolf, *Optical coherence and quantum optics*. Cambridge university press, 1995. 11

[27] S. Friberg, C. Hong, and L. Mandel, "Measurement of time delays in the parametric production of photon pairs," *Physical review letters*, vol. 54, pp. 2011–2013, 1985. 11

[28] S. Takeuchi, R. Okamoto, and K. Sasaki, "High-yield single-photon source using gated spontaneous parametric downconversion," *Applied optics*, vol. 43, no. 30, pp. 5708–5711, 2004. 11

[29] J. E. Schaar, K. L. Vodopyanov, P. S. Kuo, M. M. Fejer, X. Yu, A. Lin, J. S. Harris, D. Bliss, C. Lynch, V. G. Kozlov, *et al.*, "Terahertz sources based on intracavity parametric down-conversion in quasi-phase-matched gallium arsenide," *Selected Topics in Quantum Electronics, IEEE Journal of*, vol. 14, no. 2, pp. 354–362, 2008. 11

[30] A. B. U'Ren, K. Banaszek, and I. A. Walmsley, "Photon engineering for quantum information processing," *arXiv preprint quant-ph/0305192*, 2003. 11

[31] G. Di Giuseppe, M. Atatüre, M. D. Shaw, A. V. Sergienko, B. E. Saleh, and M. C. Teich, "Entangled-photon generation from parametric down-conversion in media with inhomogeneous nonlinearity," *Physical Review A*, vol. 66, no. 1, p. 013801, 2002. 11, 61

[32] D. Fattal, K. Inoue, J. Vučković, C. Santori, G. S. Solomon, and Y. Yamamoto, "Entanglement formation and violation of bell's inequality with a semiconductor single photon source," *Phys. Rev. Lett.*, vol. 92, p. 037903, Jan 2004. 11

[33] O. Gywat, G. Burkard, and D. Loss, "Biexcitons in coupled quantum dots as a source of entangled photons," *Phys. Rev. B*, vol. 65, p. 205329, May 2002. 11

[34] M. Scheibner, S. E. Economou, A. S. Bracker, D. Gammon, and I. V. Ponomarev, "Entangled photon pair generation with quantum dot molecules," *JOURNAL OF THE OPTICAL SOCIETY OF AMERICA B-OPTICAL PHYSICS*, vol. 29, pp. A82–A85, FEB 2012. 11

[35] R. Young, R. Stevenson, P. Atkinson, K. Cooper, D. Ritchie, and A. Shields, "Entangled photons on-demand from a single quantum dot," in *Lasers and Electro-Optics, 2006 and 2006 Quantum Electronics and Laser Science Conference. CLEO/QELS 2006. Conference on*, pp. 1 –2, may 2006. 11, 61

[36] G. Oohata, R. Shimizu, and K. Edamatsu, "Photon polarization entanglement induced by biexciton: Experimental evidence for violation of bell's inequality," *Phys. Rev. Lett.*, vol. 98, p. 140503, Apr 2007. 11

[37] A. Hayat, P. Ginzburg, and M. Orenstein, "Observation of two-photon emission from semiconductors," *Nature Photonics*, vol. 2, no. 4, pp. 238–241, 2008. Cited By (since 1996): 37. 11

[38] O. Gywat, G. Burkard, and D. Loss, "Quantum computation and the production of entangled photons using coupled quantum dots," *Superlattices and Microstructures*, vol. 31, no. 24, pp. 127 – 140, 2002. 11

[39] D. M. Greenberger, M. A. Horne, and A. Zeilinger, "Going beyond bell's theorem," in *Bell's theorem, quantum theory and conceptions of the universe*, pp. 69–72, Springer, 1989. 12

[40] H.-J. Briegel, W. Dür, J. I. Cirac, and P. Zoller, "Quantum repeaters: The role of imperfect local operations in quantum communication," *Physical Review Letters*, vol. 81, no. 26, p. 5932, 1998. 12

[41] A. Cabello and F. Sciarrino, "Loophole-free bell test based on local precertification of photon's presence," *Physical Review X*, vol. 2, no. 2, p. 021010, 2012. 12

[42] T. Pittman, B. Jacobs, and J. Franson, "Probabilistic quantum logic operations using polarizing beam splitters," *Physical Review A*, vol. 64, no. 6, p. 062311, 2001. 12

[43] D. E. Browne and T. Rudolph, "Resource-efficient linear optical quantum computation," *Physical Review Letters*, vol. 95, no. 1, p. 010501, 2005. 12

[44] D. Bouwmeester, J.-W. Pan, M. Daniell, H. Weinfurter, and A. Zeilinger, "Observation of three-photon greenberger-horne-zeilinger entanglement," *Physical Review Letters*, vol. 82, no. 7, p. 1345, 1999. 12

[45] J. Persson, T. Aichele, V. Zwiller, L. Samuelson, and O. Benson, "Three-photon cascade from single self-assembled inp quantum dots," *Physical Review B*, vol. 69, no. 23, p. 233314, 2004. 12

[46] T. E. Keller, M. H. Rubin, Y. Shih, and L.-A. Wu, "Theory of the three-photon entangled state," *Physical Review A*, vol. 57, no. 3, p. 2076, 1998. 12

[47] H. Hübel, D. R. Hamel, A. Fedrizzi, S. Ramelow, K. J. Resch, and T. Jennewein, "Direct generation of photon triplets using cascaded photon-pair sources," *Nature*, vol. 466, no. 7306, pp. 601–603, 2010. 12

[48] T. Guerreiro, A. Martin, B. Sanguinetti, J. Pelc, C. Langrock, M. Fejer, N. Gisin, H. Zbinden, N. Sangouard, and R. Thew, "Nonlinear interaction

between single photons," *Physical review letters*, vol. 113, no. 17, p. 173601, 2014. 12

[49] D. R. Hamel, L. K. Shalm, H. Hübel, A. J. Miller, F. Marsili, V. B. Verma, R. P. Mirin, S. W. Nam, K. J. Resch, and T. Jennewein, "Direct generation of three-photon polarization entanglement," *Nature Photonics*, vol. 8, no. 10, pp. 801–807, 2014. 12

[50] L. K. Shalm, D. R. Hamel, Z. Yan, C. Simon, K. J. Resch, and T. Jennewein, "Three-photon energy-time entanglement," *Nature Physics*, vol. 9, no. 1, pp. 19–22, 2013. 12

[51] S. Krapick, B. Brecht, V. Quiring, R. Ricken, H. Herrmann, and C. Silberhorn, "On-chip generation of photon-triplet states in integrated waveguide structures," in *CLEO: QELS_Fundamental Science*, pp. FM2E–3, Optical Society of America, 2015. 12

[52] M. Yukawa, K. Miyata, T. Mizuta, H. Yonezawa, P. Marek, R. Filip, and A. Furusawa, "Generating superposition of up-to three photons for continuous variable quantum information processing," *Optics express*, vol. 21, no. 5, pp. 5529–5535, 2013. 12

[53] J. Rarity and P. Tapster, "Three-particle entanglement from entangled photon pairs and a weak coherent state," *Physical Review A*, vol. 59, no. 1, p. R35, 1999. 12

[54] M. Corona, K. Garay-Palmett, and A. B. URen, "Experimental proposal for the generation of entangled photon triplets by third-order spontaneous parametric downconversion in optical fibers," *Optics letters*, vol. 36, no. 2, pp. 190–192, 2011. 12

[55] C. Schüller, *Inelastic light scattering of semiconductor nanostructures: fundamentals and recent advances*. No. 219, Springer, 2006. 14

[56] P. Harrison, *Computational Methods in Physics, Chemistry and Biology: An Introduction*. Wiley, 2001. 15, 17

[57] V. Jovanovic, Z. Ikonic, D. Indjin, P. Harrison, V. Milanovic, and R. Soref, "Designing strain-balanced gan/algan quantum well structures: Application to intersubband devices at 1.3 and 1.55 μm wavelengths," *Journal of applied physics*, vol. 93, no. 6, pp. 3194–3197, 2003. 17

[58] E. Anderson, *LAPACK Users' guide*, vol. 9. Siam, 1999. 17

[59] P. Harrison, *Quantum wells, wires and dots: theoretical and computational physics of semiconductor nanostructures*. John Wiley & Sons, 2009. 18, 40, 43, 64

[60] J. Cooper, A. Valavanis, Z. Ikonic, P. Harrison, and J. Cunningham, "Finite difference method for solving the schrödinger equation with band nonparabolicity in mid-infrared quantum cascade lasers," *Journal of Applied Physics*, vol. 108, no. 11, pp. 113109–113109, 2010. 19

[61] X. Ma, K. Li, Z. Zhang, H. Hu, Q. Wang, X. Wei, and G. Song, "Two-band finite difference method for the bandstructure calculation with nonparabolicity effects in quantum cascade lasers," *Journal of Applied Physics*, vol. 114, no. 6, pp. 063101–063101, 2013. 19

[62] Z. Ikonić, "Program fhqw3a - theory, organisation of the program, and instruction for use," *University of Leeds, (Internal Report)*, 2004. 19

[63] Z. Ikonić, P. Harrison, and R. Kelsall, "Intersubband hole-phonon and alloy disorder scattering in sige quantum wells," *Physical Review B*, vol. 64, no. 24, p. 245311, 2001. 19

[64] R. W. Boyd, *Nonlinear optics*. Academic press, 2008. 29, 52, 63, 66, 76, 90, 93, 94

[65] M. Bedoya and A. Camacho, "Nonlinear intersubband terahertz absorption in asymmetric quantum well structures," *Physical Review B*, vol. 72, no. 15, p. 155318, 2005. 29

[66] J. Heinrich, R. Langhans, M. Vitiello, G. Scamarcio, D. Indjin, C. Evans, Z. Ikonić, P. Harrison, S. Höfling, and A. Forchel, "Wide wavelength tuning

of gaas/ algaas bound-to-continuum quantum cascade lasers by aluminum content control," *Applied Physics Letters*, vol. 92, p. 141111, 2008. 40

[67] R. Razali, A. Valavanis, J. Cooper, Z. Ikonić, D. Indjin, and P. Harrison, "Mid-infrared entangled photon generation in optimised asymmetric semiconductor quantum wells," *Superlattices. Microstruct.*, vol. 90, pp. 107–116, 2016. 44, 62

[68] C. Sirtori, F. Capasso, J. Faist, and S. Scandolo, "Nonparabolicity and a sum rule associated with bound-to-bound and bound-to-continuum intersubband transitions in quantum wells," *Phys. Rev. B*, vol. 50, no. 12, p. 8663, 1994. 47

[69] T. Suhara and T. Nosaka, "Quantum theory analysis of loss effects in guided nonlinear-optic twin-photon generation," *IEEE J. Quant. Electron.*, vol. 42, no. 8, pp. 777–784, 2006. 53, 65

[70] S. Adachi, "GaAs, AlAs, AlxGa1-xAs and : Material parameters for use in research and device applications," *J. Appl. Phys.*, vol. 58, no. 3, pp. R1–R29, 1985. 54, 65, 70

[71] T. Skauli, P. Kuo, K. Vodopyanov, T. Pinguet, O. Levi, L. Eyres, J. Harris, M. Fejer, B. Gerard, L. Becouarn, *et al.*, "Improved dispersion relations for GaAs and applications to nonlinear optics," *J. Appl. Phys.*, vol. 94, no. 10, pp. 6447–6455, 2003. 54, 65

[72] L. Zhang, A. B. U'ren, R. Erdmann, K. A. O'Donnell, C. Silberhorn, K. Banaszek, and I. A. Walmsley, "Generation of highly entangled photon pairs for continuous variable bell inequality violation," *J. Mod. Opt.*, vol. 54, no. 5, pp. 707–719, 2007. 59

[73] L. Tombez, S. Schilt, J. Di Francesco, T. Führer, B. Rein, T. Walther, G. Di Domenico, D. Hofstetter, and P. Thomann, "Linewidth of a quantum-cascade laser assessed from its frequency noise spectrum and impact of the current driver," *App. Phys. B*, vol. 109, no. 3, pp. 407–414, 2012. 59

[74] R. Razali, Z. Ikonić, D. Indjin, and P. Harrison, "Polarization-entangled mid-infrared photon generation in p-doped semiconductor quantum wells," *Semiconductor Science and Technology*, vol. 31, no. 11, p. 115011, 2016. 61

[75] N. Gisin and R. Thew, "Quantum communication," *Nature Photonics*, vol. 1, no. 3, pp. 165–171, 2007. 61

[76] J. Volz, M. Scheucher, C. Junge, and A. Rauschenbeutel, "Nonlinear [pi] phase shift for single fibre-guided photons interacting with a single resonator-enhanced atom," *Nature Photonics*, vol. 8, no. 12, pp. 965–970, 2014. 61

[77] S. Barz, "Quantum computing with photons: introduction to the circuit model, the one-way quantum computer, and the fundamental principles of photonic experiments," *Journal of Physics B: Atomic, Molecular and Optical Physics*, vol. 48, no. 8, p. 083001, 2015. 61

[78] A. K. Ekert, "Quantum cryptography based on bells theorem," *Physical review letters*, vol. 67, no. 6, p. 661, 1991. 61

[79] F. Bussières, C. Clausen, A. Tiranov, B. Korzh, V. B. Verma, S. W. Nam, F. Marsili, A. Ferrier, P. Goldner, H. Herrmann, *et al.*, "Quantum teleportation from a telecom-wavelength photon to a solid-state quantum memory," *Nature Photonics*, vol. 8, no. 10, pp. 775–778, 2014. 61

[80] M. Pavičić, "Entanglement and superdense coding with linear optics," *International journal of quantum information*, vol. 9, no. 07n08, pp. 1737–1744, 2011. 61

[81] P. Sarrafi, E. Y. Zhu, K. Dolgaleva, B. M. Holmes, D. C. Hutchings, J. S. Aitchison, and L. Qian, "Continuous-wave quasi-phase-matched waveguide correlated photon pair source on a iii–v chip," *Applied Physics Letters*, vol. 103, no. 25, p. 251115, 2013. 61

[82] C. Xiong, G. D. Marshall, A. Peruzzo, M. Lobino, A. S. Clark, D.-Y. Choi, S. J. Madden, C. M. Natarajan, M. G. Tanner, R. H. Hadfield, *et al.*, "Generation of correlated photon pairs in a chalcogenide as2s3 waveguide," *Applied Physics Letters*, vol. 98, no. 5, p. 051101, 2011. 61

[83] Y. Chen, J. Zhang, M. Zopf, K. Jung, Y. Zhang, R. Keil, F. Ding, and O. G. Schmidt, "Wavelength-tunable entangled photons from silicon-integrated iii-v quantum dots," *Nat. Commun.*, vol. 7, 2016. 61

[84] D. B. Rao, S. Yang, and J. Wrachtrup, "Generation of entangled photon strings using nv centers in diamond," *Phys. Rev. B*, vol. 92, no. 8, p. 081301, 2015. 61

[85] M. Cusack, M. Shaw, and M. Jaros, "Role of localization in determining second-order optical nonlinearities in p-type gaas-alas asymmetric quantum wells," *Physical Review B*, vol. 49, no. 23, p. 16575, 1994. 62

[86] T. Suhara and H. Kintaka, "Quantum theory analysis of twin-photon beams generated by parametric fluorescence," *IEEE J. Quant. Electron.*, vol. 41, no. 9, pp. 1203–1212, 2005. 70

[87] M. Corona, K. Garay-Palmett, and A. B. URen, "Third-order spontaneous parametric down-conversion in thin optical fibers as a photon-triplet source," *Physical Review A*, vol. 84, no. 3, p. 033823, 2011. 76

[88] C. Sirtori, F. Capasso, J. Faist, and S. Scandolo, "Nonparabolicity and a sum rule associated with bound-to-bound and bound-to-continuum intersubband transitions in quantum wells," *Phys. Rev. B*, vol. 50, pp. 8663–8674, Sep 1994. 91